Empirical Modeling and System Optimization for a Precooled Joule-Thomson Cycle for Cryosurgery

By

Kyle C. Rule

A thesis submitted in partial fulfillment of

the requirements for the degree of:

Master of Science

(Mechanical Engineering)

at the

UNIVERSITY OF WISCONSIN – MADISON

2014

This thesis has been approved by

Professor Gregory F. Nellis	**Date**
Professor Sanford A. Klein	**Date**

Abstract

Cryosurgery is a viable treatment option for patients suffering from various internal or dermatological diseases/disorders. The technique utilizes the application of a very low temperature instrument or fluid to ablate undesirable tissue. Although minimally invasive in comparison to many alternative treatments, the current state-of-the-art must often employ more than one cryoprobe depending on the size of the affected region. Precooled Mixed Gas Joule-Thomson cycles offer a potential increase in cooling capacity, but also in design problem complexity as the appropriate selection of mixtures and operating conditions is not intuitive. Previous work has focused on cycle improvement via *a priori* mixture optimization. The focus of this research is, in part, to advance the design approach capability of the model via incorporation of a compressor map and orifice sizing tool. These provisions allow for system optimization for a given compressor size and heat exchanger geometry.

In order to evaluate the predictive capabilities of the model, its use was verified experimentally. A fully instrumented cryosurgical probe test facility constructed as part of previous research was improved for this purpose. A carefully selected binary mixture was utilized in the experimental system and compared to modeled system response as a function of cooling load and 2^{nd} stage static charge pressure. The predictive model was found to over-predict the cooling load by approximately 20%, largely resulting from the under-approximation of the recuperator hot side inlet refrigerant temperature. A correction method for this temperature is presented and found to vary linearly with cooling load. Finally, component level modeling errors are quantified, showing agreement between 5 and 20% with the measured data.

Acknowledgements

This research would not have been possible without the many contributions from my advisors, family, and friends/colleagues in the Solar Energy Lab.

First, I want to extend a special thank you to Professor's Greg Nellis and Sandy Klein. The opportunity to work in the SEL and learn from you both during the last year and a half has been a privilege and one of the most rewarding experiences in my life. Your classes have been by far the most interesting and influential of any other I have taken, no doubt as a result of your passion for teaching and intelligence. There is not enough I can say to express my gratitude regarding the knowledge, research ideas, and encouragement you have shared with me. I would also like to thank Professor Franklin Miller for the project advice and excellent conversation. I am grateful for your willingness to provide valuable insight and experience in cryogenics.

I want to thank my dad, Charles, mom, Charlotte, and sister, Samantha for providing the support and motivation to pursue a higher level degree. Dad, your work ethic and moral compass are second to none and I'm lucky to have had as good a role model. The sacrifices you and mom have made for me throughout my life are truly appreciated. I would also like to thank Robert Christiaansen, a family friend (more like family) who has always been there to provide sage advice and guidance. I would be in a very different position now if not for your support.

I want to thank my lovely fiancée Ashley for sharing in this journey with me. Your patience and encouragement brought out the best in me. I recognize the priority you placed on my education as you progressed through your own degree and work.

Finally, I want to thank the many members of the SEL who have participated in one way or another in this research. My former undergraduate assistants, Dan Uhler and Erin Connors, for the time spent working with me through issues with the experimental test facility as well as collecting data. Harrison Skye, who has been so gracious to provide his support and advice long after completion of his research work in the SEL. My office mates, Amir Jahromi, Rodrigo Barraza, Fritz Schwartz, Renzhuo Wang, and Dongsheng Zhang, for their friendship, moral support, and advice throughout the project. In addition I want to thank all of the SEL students for making my time here so enjoyable including John, Nathan, Diego, Wenjie, Mohamed, and many others.

Table of Contents

List of Figures

List of Tables

List of Variables

Nomenclature

A_0	Cross-sectional jewel orifice area (m^2)
$A_{i,uc}$	Uncorrected area output for the *i*th mixture constituent (m^2)
a_0	Recuperator pressure drop coefficient (kPa)
a_1	Recuperator pressure drop coefficient (-)
C	Compressor clearance volume ratio (-)
c	Specific heat (J/kg-K)
$C_{iterations}$	Number of model iterations (-)
$c_{rec,c}$	Recuperator cold side sectional specific heat capacity (J/kg-K)
$\dot{C}_{rec,c}$	Recuperator cold side sectional capacitance rate (W/K)
$\dot{C}_{rec,h}$	Recuperator hot side sectional capacitance rate (W/K)
$c_{rec,h}$	Recuperator hot side sectional specific heat capacity (J/kg-K)
c_p	Constant pressure specific heat (J/kg-K)
c_v	Constant volume specific heat (J/kg-K)
$d_{orifice}$	Jewel orifice diameter (m)
E_{RMS}	RMS error (units depend on metric analyzed)
h	Enthalpy (J/kg)
h_{min}	Lower bound on 2^{nd} stage cycle enthalpy (J/kg)
$h_{rec,c}$	Recuperator cold side nodal enthalpy (J/kg)
$h_{rec,h}$	Recuperator hot side nodal enthalpy (J/kg)
k	Isentropic exponent (-)
$L_{tube,f,rec}$ *or* $L_{rec,f}$	Total length of finned recuperator tubing (m)
L_{rec}	Sectional length of finned recuperator tubing (m)
$L_{f,actual}$	Actual recuperator finned tube length (m)
$limit_{lower}$	Lower limit on the cold end recuperator temperature difference (K)
$limit_{upper}$	Upper limit on the cold end recuperator temperature difference (K)
m	Mass of refrigerant contained within the 2^{nd} stage cycle (kg)
$\dot{m}$	Mass flow rate (kg/s)
$\dot{m}_{2nd}$	2^{nd} stage mass flow rate (kg/s)

$\dot{m}_{2nd,actual}$	Actual 2nd stage cycle mass flow rate (kg/s)
$\dot{m}_{2nd,predicted}$	Predicted mass flow rate for 2nd stage cycle (kg/s)
Max_{meas}	Measurement range (units depend on instrument analyzed)
$N \text{ or } N\#$	Number of heat exchanger sections (-)
N_{bits}	Number of bits of data acquisition system (-)
N_{calls}	Number of mixture property database calls (-)
N_{points}	Number of points used to develop correlation (-)
N_{rec}	Number of recuperator sub-sections (-)
NTU_{rec}	Recuperator number of heat transfer units (-)
P	Pressure (Pa)
P_A	Partial pressure of mixture constituent A (Pa)
P_{amb}	Ambient pressure (Pa)
P_B	Partial pressure of mixture constituent B (Pa)
P_C	2nd stage cycle charge pressure (Pa)
$P_{discharge}$	Compressor discharge pressure (Pa)
$P_{downstream} \text{ or } P_0$	Pressure downstream of jewel orifice (Pa)
P_H	2nd stage cycle high side pressure (Pa)
$P_{high,2nd}$	2nd stage cycle compressor discharge pressure (Pa)
P_L	2nd stage cycle low side pressure (Pa)
$P_{low,1st}$	1st stage compressor suction pressure (Pa)
$P_{low,2nd}$	2nd stage compressor suction pressure (Pa)
$P_{rec,c}$	Recuperator cold side nodal pressure (Pa)
$P_{rec,h}$	Recuperator hot side nodal pressure (Pa)
$P_{suction}$	Compressor suction pressure (Pa)
$P_{upstream} \text{ or } P_1$	Pressure immediately upstream of jewel orifice (Pa)
P_X	Partial pressure of constituent X (Pa)
$\dot{Q}_{load}$	Cryoprobe cooling capacity (W)
$\dot{Q}_{rec}$	Heat transfer rate (W)
q_{rec}	Energy per unit mass (J/kg)
$\dot{Q}_{load,\max}$	Maximum cryoprobe cooling capacity (W)

$R_{specific}$	Gas constant (J/kg-K)
$Range_o$	Instrument output voltage range (V)
Re	Reynold's number (-)
RF_i	Response factor for the *i*th constituent (-)
s	Entropy (J/kg-K)
T	Temperature (K)
T_{amb}	Ambient temperature (K)
$T_{downstream}$	Temperature immediately downstream of orifice (K)
$T_{rec,c}$	Recuperator cold side nodal temperature (K)
$T_{rec,c,diff}$	Recuperator cold end temperature difference (K)
$T_{rec,h}$	Recuperator hot side nodal temperature (K)
$T_{rec,h,diff}$	Recuperator hot end temperature difference (K)
T_{sat}	Saturation temperature (K)
$T_{suction}$	Compressor suction side fluid temperature (K)
t	Time (s)
U	Internal energy (J)
U_{acc}	Instrument accuracy (units depend on instrument analyzed)
U_{cal}	Total instrument uncertainty (units depend on instrument analyzed)
U_{ins}	Instrument uncertainty (units depend on instrument analyzed)
U_{prec}	Repeatability error (units depend on instrument analyzed)
U_{res}	Data acquisition system resolution (units depend on instrument)
UA_{rec}	Recuperative heat exchanger conductance (W/K)
UA_{total}	Combined/total heat exchanger conductance (W/K)
V	2nd stage cycle volume (m^3)
v	Velocity (m/s)
v_0	Velocity downstream of jewel orifice (m/s)
v_1	Velocity upstream of jewel orifice (m/s)
$\dot{V}_{disp}$	Compressor displacement rate (m^3/s)
V_H	2nd stage cycle high side volume (m^3)
V_L	2nd stage cycle low side volume (m^3)
$v_{rec,c,out}$	Recuperator cold stream outlet fluid velocity (m/s)

$v_{rec,h,in}$	Recuperator hot stream inlet fluid velocity (m/s)
$\dot{V}_{suction}$	Compressor suction side volumetric flow rate (m^3/s)
x	Thermodynamic mass quality (-)
x_c	Recuperator cold stream thermodynamic mass quality (-)
y_i	Mole fraction of the *i*th mixture constituent (-)
$\bar{y}_{2nd}$	Mole fraction vector of 2nd stage refrigerant (-)

Greek Symbols

ΔP	Pressure difference (Pa)
$\Delta P_{rec,c}$	Recuperator cold stream pressure drop (Pa)
$\Delta P_{rec,h}$	Recuperator hot stream pressure drop (Pa)
ΔT	Temperature difference (K)
$\Delta T_{pp,rec}$	Recuperator pinch point temperature difference (K)
ε_{rec} *or* ε	Recuperator section effectiveness (-)
η_{vol}	Compressor volumetric efficiency (-)
ρ	Fluid density (kg/m^3)
$\rho_{rec,c,out}$	Recuperator cold stream outlet fluid density (kg/m^3)
$\rho_{rec,h,in}$	Recuperator hot stream inlet fluid density (kg/m^3)

Subscripts

#	Cryoprobe state number (-)

1 Introduction and Literature Review

1.1 Cryosurgery Review

Cryosurgery is a medicinal technique used to destroy or ablate diseased tissue by the application of a very low temperature fluid or object. It is a treatment method utilized for a wide variety of internal and dermatological diseases, with the former often relying on the use of a cryosurgical probe to impart cooling to the undesirable tissue. The temperatures required to induce cell death are reported to be between -20 °C and -50 °C (Rubinsky, 2000). Thus, in controlled internal procedures, a monitoring technique must be utilized to ensure adequate temperatures are achieved beyond the margin of the affected region. There are many body imaging techniques that accomplish this task utilizing the difference between frozen and unfrozen tissue properties. Figure 1-1 details images taken using an ultrasound during a cryosurgical procedure on a liver.

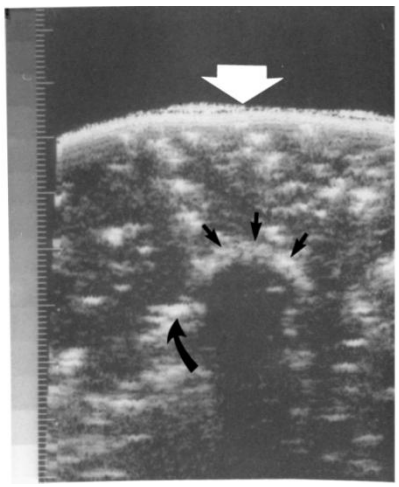

Figure 1-1: Ultrasound images of a frozen lesion beneath liver tissue. The white arrow indicates the outer surface of the liver where the ultrasound transducer was placed. The black arrows identify the perimeter of the frozen tissue (Rubinsky, 2000).

Although the ultimate freezing temperature is the predominant factor in treatment effectiveness, Gage and Baust (2009) detail additional factors, specifically for tissue nearest the edges of the application zone (in the -20 [C] to -30 [C] range). These include tissue freezing duration, thawing rate, and freeze-thaw cycle repetition. Consideration has also been given to the cooling rate, which primarily influences the size of the cryolesion as well as treatment duration.

1.1.1 Medical Objectives

The primary goal of any cryosurgical procedure is to induce the destruction of cancerous or undesirable tissue. The physical mechanisms attributing to cell necrosis are 1) direct cryoinjury of the cellular membrane and enzymatic machinery of the cell as well as 2) vascular injury resulting from tissue ischemia (which may occur at higher subzero temperatures then the former) (Hoffmann & Bischof, 2002). As tissue temperature plays the greatest role in assuring cell death, an optimal probe must be capable of reducing the

temperature to the lowest extreme possible (less than -50 °C). Thus, in general (and as will be shown in section 1.3.1), lower cryosurgical probe application temperatures are desired.

Ensuring that all of the diseased tissue reaches the lowest possible temperatures can be difficult as the volume and shape of the zone to be ablated varies greatly. For cancerous tumors larger than 4 cm or of irregular proportion, multiple probes are often used to ensure complete exposure of the tumor to the temperature range required for cell destruction (Gage & Baust, 1998). The use of multiple probes adds additional complexity to the medical procedure and increases risk to the patient due to the need for multiple insertion sites; effectively reducing a primary benefit of cryosurgery over traditional, excisional techniques. As a result, a single probe of greater cooling capacity for the same package size is advantageous, specifically for large tumors or diseased tissue volumes.

A secondary effect of large cooling power is reduced treatment duration. Fredrickson et al. (2006) showed that for a fixed cryoprobe tip geometry, a high temperature refrigeration advantage translates into a 16% reduction in the time required for steady state cryolesion size (for a nominal test case). However, compared to the average treatment duration (~10 min for a dual freeze-thaw application), this does not represent a significant decrease. Nonetheless, a reduction in operating time is beneficial for both the patient and the surgical team.

A surgical tool, specifically for use in treating internal conditions, should allow for 1) precise placement and manipulation by its user as well as 2) unconstrained application time (treatment availability). The first point may be accomplished by reduction of connective tubing and bulky storage devices, with an emphasis on ergonomic instrument design. In cryosurgery, the latter can be ensured by avoiding high pressure and liquefied gas refrigerant

systems as both are most often employed in open cycle designs and thus may be depleted during the surgical procedure.

In addition to these objectives, as with any treatment technique, the medical utility provided by a cryosurgical system must be weighed against other tools/methods in terms of its overall size and cost.

1.1.2 Advantages and Disadvantages

Although a range of treatment options exist for the removal of undesirable tissue, in this section, the benefits of cryosurgery are weighed primarily against those of traditional excisional techniques. Based on the medical objectives detailed in section 1.1.1, the treatment should be accomplished with minimal impact on surrounding healthy tissue (yet ideally in a single application), quickly, and with minimal effort by the surgical team. In addition, it should not negatively impact long term patient health.

Korpan (2007) states several advantages of cryosurgery over classical surgeries including that it spares more healthy tissue in comparison to resection, that it provides an alternative for patients who have unresectable tumors, it allows for retreatment, and that it elicits an immunologic response to antigens in the frozen tissue. There has been much debate over whether a freezing-related immunologic injury is a valid hypothesis. Hoffmann et al. (2002) cite in house laboratory work and numerous other studies in emphasizing the inconsistency of its observance. It is clear that additional work needs to be performed in this area. An additional advantage of cryosurgery is that it may be combined with other treatment methods, such as resection, in order to increase procedure efficacy.

The disadvantages of cryosurgery are largely related to ensuring the tumor or affected region is fully and properly treated. In order to reduce this problem, surgeons often rely on ultrasound or other body imaging techniques which add cost and complexity in addition to that associated with the purchase and use of the cryosurgical system itself. As internal application of cryosurgery is not commonplace, the operating procedures used in clinical practice vary. Due to the temperatures and time scales associated with the technique, overexposure can lead to the damage of healthy tissue. Conversely, misuse of an underpowered probe may leave the patient at risk of disease recurrence. For example, data shows that a significant increase in cell necrosis in the -20 °C range can be achieved through repetitive freezing (Gill, Fraser, & Carter, 1968). However, as outlined by Gage & Baust (1998), single freeze-thaw cycle procedures are widely used by physicians, impacting the patients chances at being cured. Clearly, additional work is needed to establish a more widely accepted treatment methodology (perhaps based specifically on the type of disease and/or treatment location). This will greatly aid in making the use of cryosurgery for internal diseased tissue resection more commonplace.

1.1.3 Past Implementation

The many benefits of cryotherapy have been recognized since long before the medical advances of the present era. Around 1845, James Arnott, who is recognized as the first physician to utilize the freezing of tissue for the treatment of cancer, focused on using the application of cold in localized anesthesia (Rubinsky, 2000). He accomplished this using a combination of crushed ice and sodium chloride. Technological advances in cryogenics during the early part of the 20^{th} century led to the widespread use of solid CO_2 as an

inexpensive means of treating dermatological conditions. However, these treatments were only able to penetrate to a depth of around 7 mm. It wasn't until the development of a liquid nitrogen cryosurgical apparatus in the early 1960s that cryosurgical techniques were reviewed for the internal treatment of diseases (Baust, Gage, Ma, & Zhang, 1997). An example of one such design is detailed in Figure 1-2. Liquid nitrogen is fed through the inner cannula to the load location where it vaporizes, thereby providing latent cooling to the active portion of the tip. The nitrogen vapor is then exhausted through the outer tube. The cryosurgical system described allows for some recapture of the vaporized nitrogen but vacuum storage of the refrigerant is required and application time is limited. Additionally, the flow of exhausted nitrogen must be controlled and ultimately represents an asphyxiation hazard for the patient and surgical team.

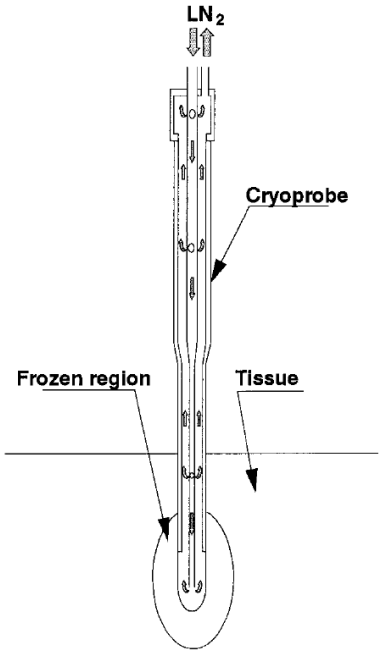

Figure 1-2: A cross sectional view of a liquid N_2 cryosurgical probe design (Baust et al., 1997).

Through the 1970's, cryosurgical treatment methods were primarily used in treating external conditions as a result of the inability to adequately monitor the extent of tissue exposure during internal procedures. With the widespread use of ultrasound in the 1980's, cryotherapy experienced resurgence. Through the 1990's, these cycles relied largely on the use of liquid nitrogen or argon gas-based Joule-Thomson (JT) systems. Argon gas-based systems were an improvement over liquid nitrogen in that they allowed for real-time control of ice ball formation and the cryoprobe size could be reduced (due to the use of a warm gas at the inlet, eliminating large insulated tubes) (Babaian et al., 2008). An example of such a system is shown in Figure 1-3. Argon is released from a high pressure storage cylinder through a recuperative heat exchanger where it receives precooling from the gas which has already expanded over the orifice. In order to achieve the cooling capacity required via Joule-Thomson expansion, a high pressure drop and mass flow rate are required. The major disadvantages to this cycle are argon storage and exhaust gas control.

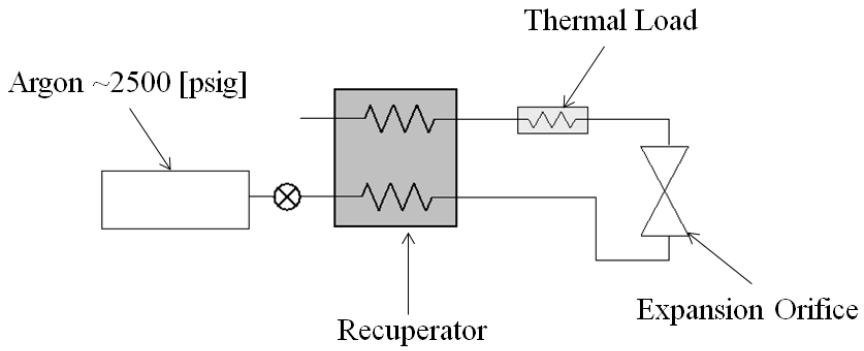

Figure 1-3: Argon gas-based Joule-Thomson cycle.

Further improvements to Joule-Thomson cycle technology, specifically the implementation of closed, mixed gas systems, have further improved the state of art in recent years.

1.2 Current Implementation – Precooled Mixed Gas Joule-Thomson Cycle

The cycle under investigation by this research builds upon the basic, single stage Joule-Thomson systems described briefly in section 1.1.3. It is a two-stage cycle that utilizes a mixed gas refrigerant in order to maximize potential cooling performance over a large temperature range while minimizing the pressure rise required by the compressor. Figure 1-4 below shows the first and second stage fluid flow paths through a cross section of the two stage cryosurgical probe analyzed by this research. As a result of high thermal losses in the connective tubing, all heat exchange occurs within a double walled evacuated stainless steel cryoprobe sheath.

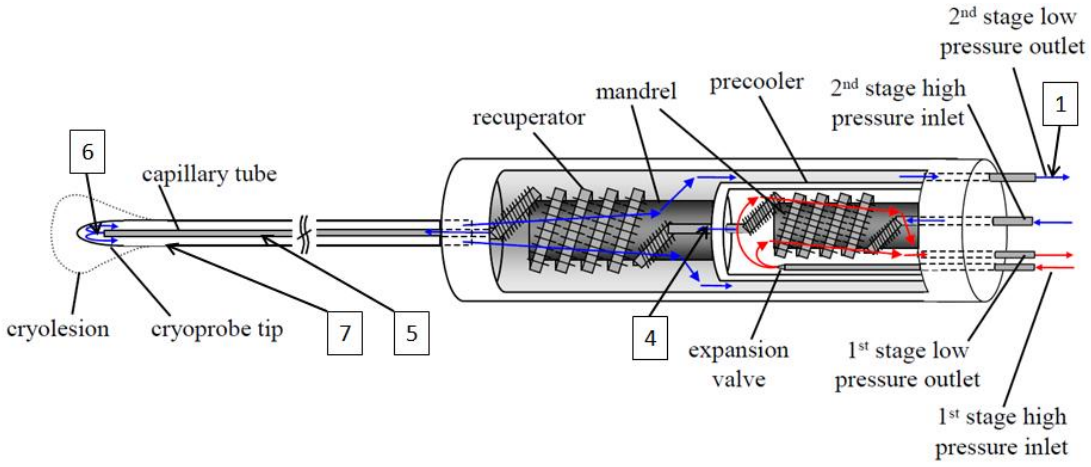

Figure 1-4: Cross sectional fluid flow schematic for the 2 stage cryosurgical probe analyzed by this research (H. M. Skye, 2011)

The first stage, denoted by the red arrows in Figure 1-4, utilizes a synthetic pure fluid refrigerant, R410a, to pre-cool the incoming refrigerant mixture from the 2nd stage. The mixed gas, which can consist of any synthetic or natural gas refrigerant blend, enters the cryoprobe from flexible fluid lines that lead to a compressor cabinet. The mixed gas first passes through the precooler before entering the recuperator (denoted by state 4), where it

receives additional precooling from the fluid returning from the active portion of the cryoprobe tip. States 5 and 6 are just before and after the expansion orifice, respectively. After passing through the active portion of the tip (represented by state 7), the fluid returns to the compressor (state 1).

1.2.1 Cycle Analysis/Performance Metrics

A cryoprobe system schematic, with states corresponding to those in Figure 1-4 is shown below (Figure 1-5). In order to evaluate the cooling power of this staged refrigeration system, an energy balance may be taken over the active portion of the cycle (i.e. the portion in contact with the biological thermal load).

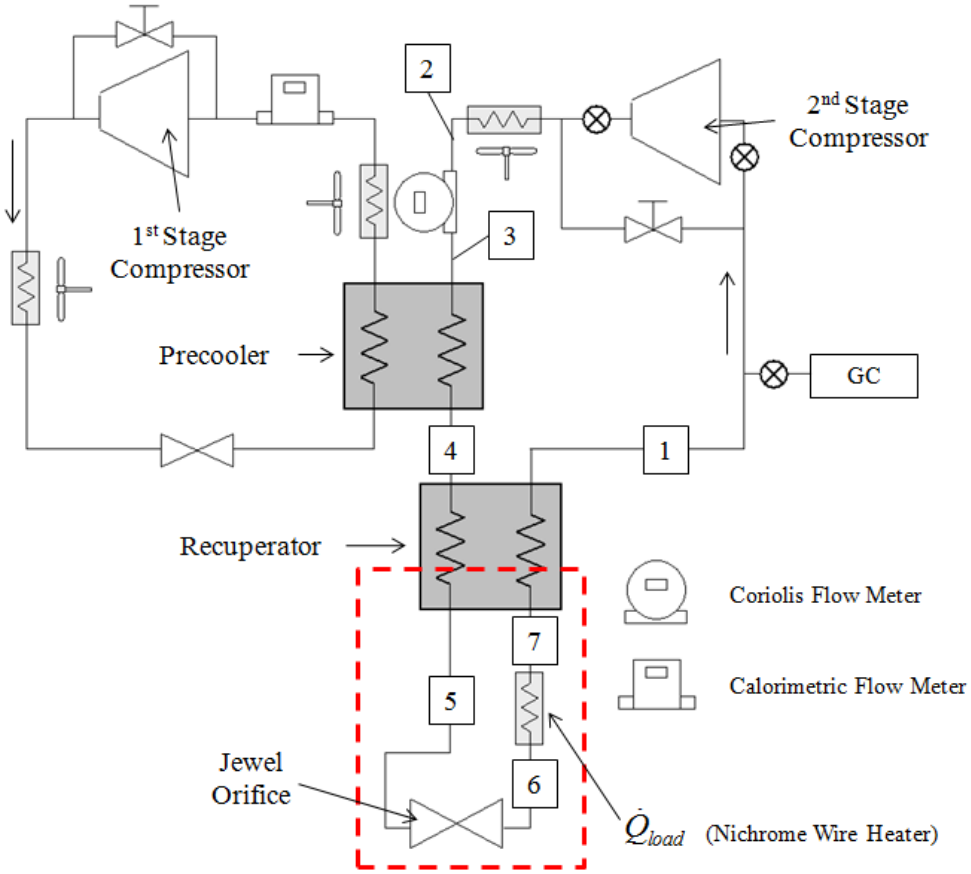

Figure 1-5: Cryoprobe system schematic. In order to evaluate system cooling potential, a control volume is taken over the coldest portions of the system (shown by the dashed line - from the biological thermal load through an arbitrary cross section of the recuperator).

The control volume utilized for this analysis is highlighted by the dashed line in Figure 1-5 and cuts through an arbitrary cross section of the recuperator. Assuming steady state operating conditions and representing the temperature difference between the two fluid streams by ΔT, the energy balance simplifies to the following:

$$\frac{\dot{Q}_{load}}{\dot{m}_{2nd}} = [h(P_{low,2nd}, T, \bar{y}_{2nd}) - h(P_{low,2nd}, T + \Delta T, \bar{y}_{2nd})] \tag{1.1}$$

where $\bar{y}_{2nd}$ represents the molar composition of the 2nd stage (mixed gas) cycle refrigerant

Stated formally, the cooling capacity of the precooled mixed gas cryosurgical probe is a function of the enthalpy difference between the two fluid streams at any arbitrary cross section of the recuperator. In order to simplify this relationship and establish an upper bound on system performance, an ideal cycle is considered (i.e., one where the heat exchanger length or conductance is infinitely large). In such a case, the temperature difference between the two fluid streams will equal zero at some pinch point location within the heat exchanger. The resulting simplified energy balance provides a relation for the maximum potential cooling load that can be provided by the mixed gas cycle.

$$\frac{\dot{Q}_{load,\max}}{\dot{m}_{2nd}} \le \min[h(P_{low,2nd}, T, \bar{y}_{2nd}) - h(P_{low,2nd}, T, \bar{y}_{2nd})] \quad for\ T_7 \le T \le T_4 \tag{1.2}$$

Equation (1.2) is evaluated over the entire range of temperatures spanned by the recuperative heat exchanger in order to determine the minimum isothermal enthalpy difference between the two fluid streams.

Consider an ideal JT cycle utilizing a pure fluid refrigerant (e.g., argon). In the ideal case, there is no pressure drop through the heat exchanger and the effectiveness is equal to unity. In order to fully destroy any tissue that comes into contact with the probe, the temperature of the fluid returning from the active portion of the tip (state 7) is set at 115 K. A nominal test condition is then selected based on experience with the experimental test facility (reviewed in detail in chapter 2). Specifically, the temperature of the incoming refrigerant (state 4) is assumed to be precooled to 240 K and the pressure drop over the expansion orifice is taken to be approximately 260 psi. The minimum isothermal enthalpy difference for this particular operating condition can be determined using equation (1.2). For the purposes

of this example, a quadratic approximations optimization algorithm is used within Engineering Equation Solver (Klein, 2013a) in order to iteratively determine the pinch point temperature between states 4 and 7. The corresponding value of $\frac{\dot{Q}_{load,\max}}{\dot{m}_{2nd}}$ is calculated to be 5.146 kJ/kg.

Based on this information, the recuperator temperature profile for both the cold and warm fluid streams can be obtained. Again, equation (1.2) is utilized, but this time over a cross section passing through states 5 and 7. This energy balance may be solved for T_5 using the value of $\frac{\dot{Q}_{load,\max}}{\dot{m}_{2nd}}$ calculated above. Knowing the temperature at state 4, an energy balance on the warm side of the recuperator is used to determine the rate of heat transfer between the two fluid streams:

$$\frac{\dot{Q}_{rec}}{\dot{m}_{2nd}} = h_4 - h_5 \tag{1.3}$$

Finally, the enthalpy profile for both the warm and cold fluid streams through the recuperator may be calculated in a manner that is similar to the methods presented in section 8.4.2 of Nellis and Klein (2009). The corresponding temperature profile for the warm and cold streams is shown in Figure 1-6(a). As shown, the pinch point is located at the warm end of the heat exchanger.

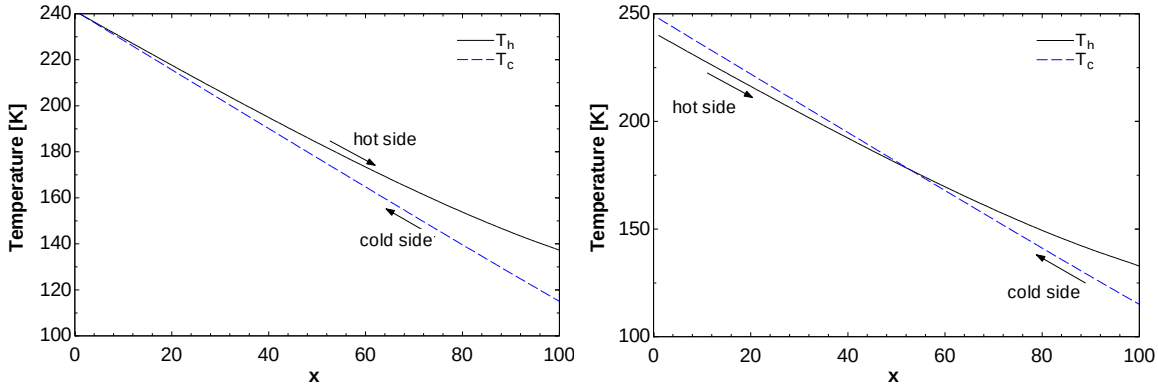

Figure 1-6: Temperature vs. axial position in an idealized recuperator for a nominal test condition. Equation (1.2) evaluated using (a) the temperature resulting in the minimum isothermal enthalpy difference between streams, and (b) using an arbitrary temperature between T_4 and T_7.

If the analysis is repeated using an average temperature between states 4 and 7, a 2nd law violation is observed (See Figure 1-6(b)). An exhaustive study would reveal that equating the maximum cooling potential to any other isothermal enthalpy difference, corresponding to a different temperature within the recuperator (in this case, other than T_4), would represent a violation of the second law.

As the maximum possible cooling potential of the cryosurgical probe has been evaluated, it would seem reasonable to use this as a primary figure of merit in comparing the potential benefits of different mixture blends and system operating conditions. However, this relation only considers an idealized cycle. A more appropriate comparison includes the operating bounds of an actual cryosurgical system and their effects on refrigeration performance. Other objective functions have been suggested for mixed gas JT cycles. Alexeev et al. (1997) utilize a fractional Carnot efficiency in optimizing various hydrocarbon mixture compositions. Maytal et al. (2005), who performed mixture optimization on a single stage JT cycle, used three different target functions to direct his analysis including: cooling capacity, the coefficient of performance, and the compactness of the recuperator ($\frac{\dot{Q}}{UA}$). His

model constrained the recuperator pinch point temperature difference in order to simulate the limitations resulting from fixed heat exchanger size, similar to the method described in section 2.2.3. As the primary objective of this research is to maximize cooling capacity for a given cryosurgical probe design (i.e., we are not able to alter the heat exchanger length or geometry), different operating conditions and mixtures are compared on the basis of cooling load for a fixed tip temperature.

1.2.2 Benefits of a Mixed Gas Cycle

The maximum possible refrigeration power for a mixed gas JT cryosurgical probe is limited by the minimum isothermal enthalpy difference between the high and low pressure fluid streams within the recuperator. Figure 1-7 details the difference in the isothermal enthalpy difference for (a) a binary mixture of R14+R23 and (b) argon. As can be seen from the plots, the binary mixture has a higher isothermal enthalpy difference for the same pressure drop and spans a much larger range of temperatures as compared to the argon case. This improvement is a result of the differing boiling points of the mixture constituents, effectively expanding the saturated regime over a larger range of intensive properties. In order to obtain the same isothermal enthalpy difference, the pure fluid refrigerant would need to be expanded over a much greater pressure drop. This explains the high pressure storage requirement for open JT systems using argon. Mixed gas refrigerants have the potential to provide the same level of cooling but at much lower pressure drops (suitable for a small compressor) and thus are ideal for a closed JT system.

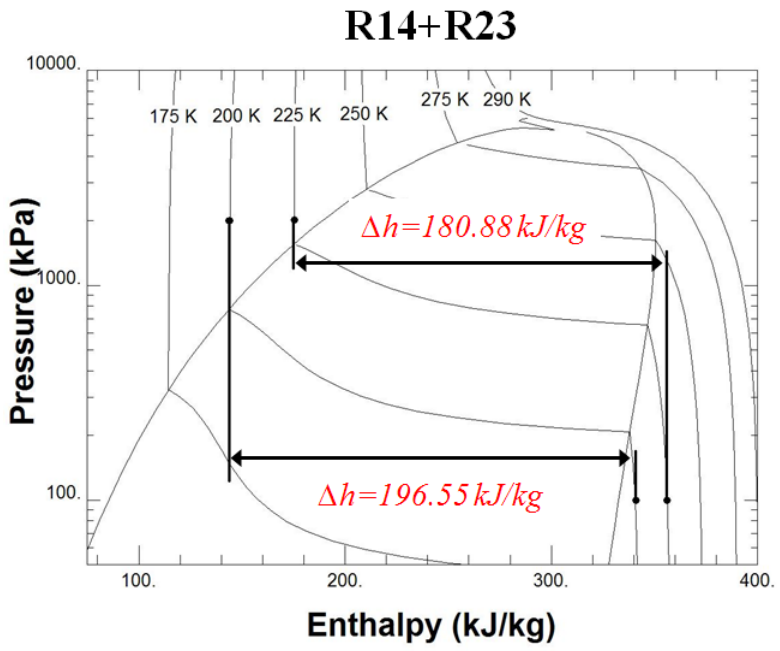

(a)

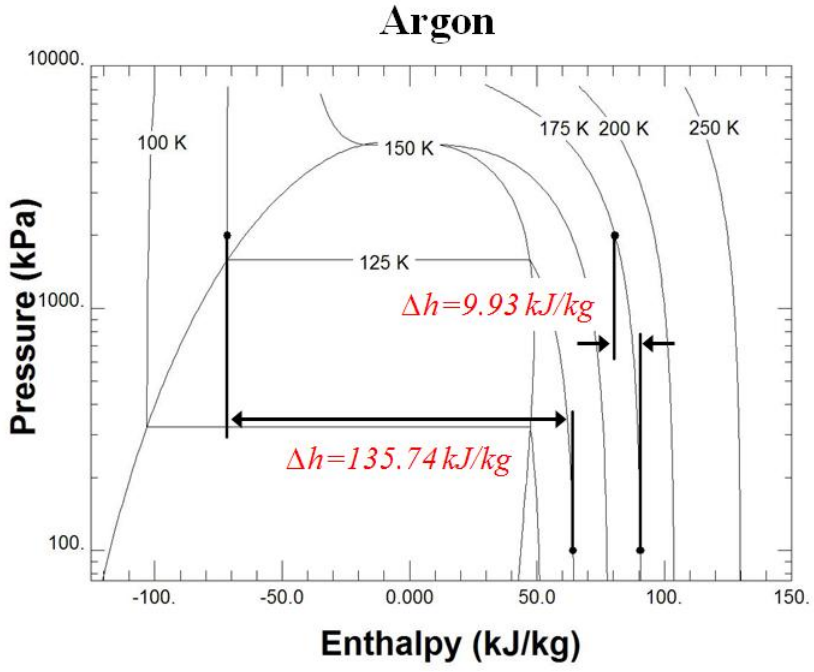

(b)

Figure 1-7: Pressure vs. enthalpy property plots comparing the isothermal enthalpy difference a pressure drop of 1900 [kPa] for (a) a binary mixture of R14 and R23 (0.2 mole fraction R14) and (b) a pure fluid refrigerant (argon).

In any real system, there will be difference in temperature between the high and low pressure fluid streams at any location within the recuperator. A comparison of a non-isothermal case is presented in Figure 1-8. As shown, for a 25 K temperature drop, the operating range resulting in high refrigeration performance for the pure fluid refrigerant system is severely limited. This is not the case for the mixed gas cycle, where a higher value of the enthalpy difference between the high and low pressure streams is observed, as well as a larger viable system operating range.

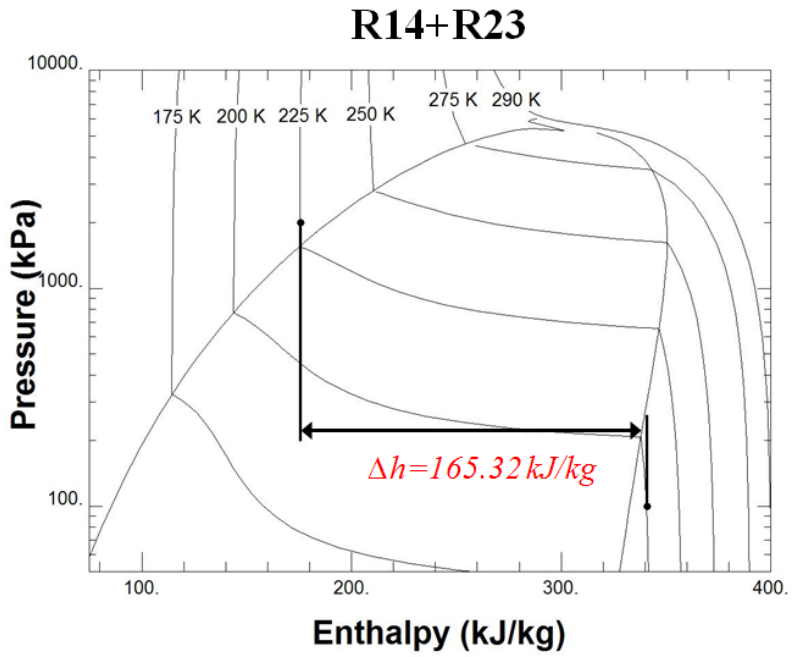

(a)

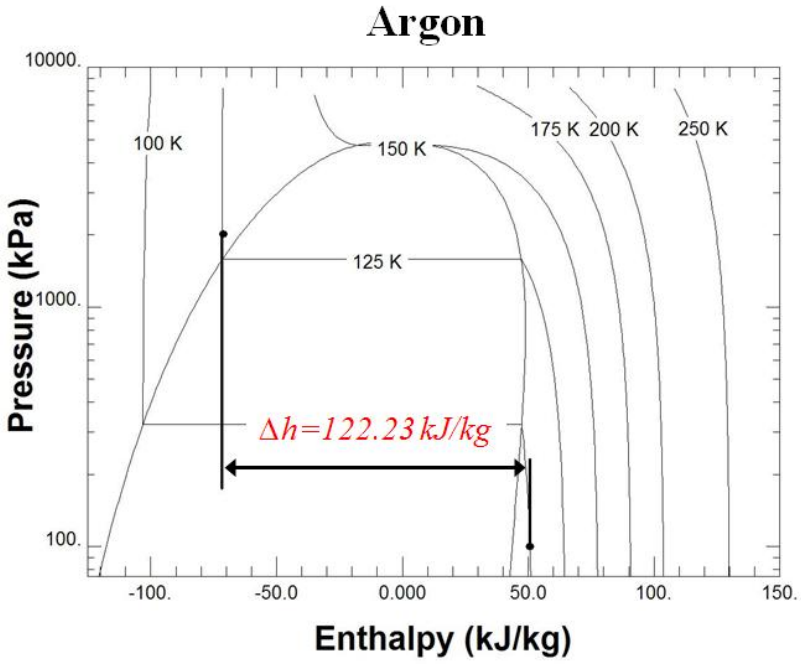

(b)

Figure 1-8: Pressure vs. enthalpy property plots comparing the non-isothermal enthalpy difference with a pressure drop of 1900 [kPa] for (a) a binary mixture of R14+R23 and (b) a pure fluid refrigerant (argon).

1.2.3 Advantages of Precooling

Following the discussion in section 1.2.1, it can be observed that the isothermal enthalpy difference drops off substantially with higher temperatures. Specifically for the argon case, Figure 1-6(a) showed that the actual location of the pinch point will be on the warm side of the heat exchanger. The same will often be true with mixed gas refrigerants, although due to the temperature glide within the vapor dome, the pinch can occur within the heat exchanger as well. Specifically, as shown in Figure 1-8(a), for a nominal mixture of R14 and R23, the enthalpy difference trails off greatly for temperatures above about 250 K. As the maximum possible cooling load is limited by the minimum isothermal enthalpy difference (as detailed by Equation(1.2)), the temperature difference at the warm end of the recuperator represents a barrier to cryoprobe performance. In order to combat this, a cascaded refrigeration system can be utilized, with one cycle precooling the mixed gas refrigerant. By depressing the highest temperature spanned by the recuperator, an increase in cooling load potential is observed.

Skye et al. (2009) verified this effect for a 7 component refrigerant mix by optimizing the composition at two different recuperator operating temperature spans, 1) between 285 K and 140 K and 2) between 238 K and 140 K. The corresponding enthalpy difference for a 900 kPa pressure drop was plotted as a function of temperature. As can be seen from Figure 1-9, the minimum enthalpy difference and thus the maximum potential cooling load for case 2 is substantially greater than that of case 1.

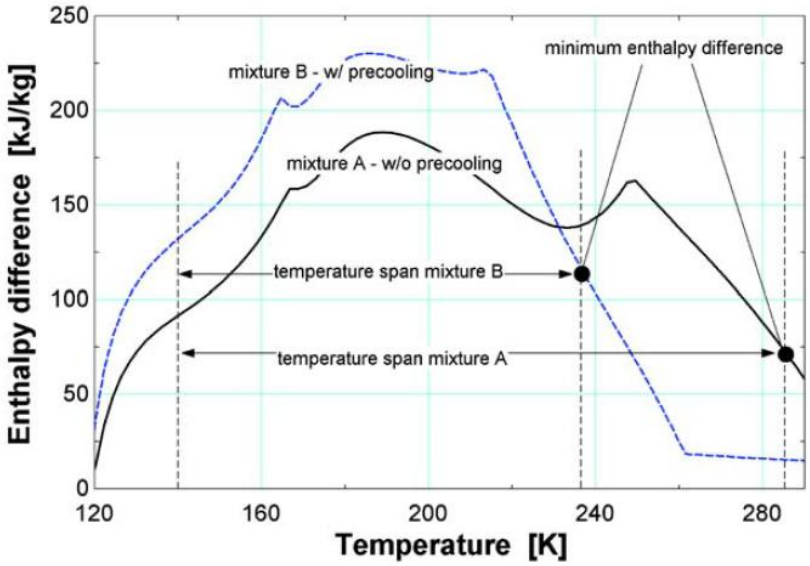

Figure 1-9: Enthalpy difference between the high and low pressure streams as a function of temperature with mixture A optimized for a temperature span of 285 [K] to 140 [K] and mixture B optimized between a temperature span of 238 [K] and 140 [K] (H. Skye et al., 2009).

1.3 Previous Work

A significant amount of past research has been conducted on mixed gas JT cryosurgical systems. The primary focus of previous investigations has been directed towards the identification of optimal mixture compositions for use in both single stage open and precooled mixed gas cycles. Research conducted by Skye (2011) is of particular importance as the same experimental test facility is utilized for the work in this study.

1.3.1 Single Stage Cryosurgical Cycles

Some of the first work directed towards cryosurgical probe system modeling was conducted by Keppler et al (2004). This effort was primarily focused on maximizing refrigeration performance by varying the composition of the mixed gas for a particular operating condition. A thermodynamic pinch point model was utilized to characterize the system and evaluate model convergence. This formulation is described by Maytal et al (2005). The cycle model was interfaced with a genetic optimization algorithm using the

cryoprobe recuperator compactness target, $\frac{\dot{Q}_{load}}{UA_{total}}$, as the objective function guiding optimization. Analysis was performed on both hydrocarbon and synthetic mixture blends (with the synthetic mixture representing a non-flammable refrigerant alternative). The reported data highlights trends of optimal mixture composition with operating temperature. In both cases, it was observed that increasing the number of constituents theoretically yielded far greater cooling capacity than could be achieved with smaller 2 and 3 component mixtures. In addition, the ideal blend utilized constituents which covered a large range of boiling point temperatures.

Although an optimum mixture composition could be identified for a given system operating point, the recuperator compactness target provides no information with regard to the size of the cryolesion that will be produced. In order to quantify this, as well as establish a more surgically relevant performance target (i.e., cryolesion size) for cycle mixture optimization, Fredrickson (2004) formulated a numerical model of a cryolesion development in human tissue. Using this model, she was able to relate the cryoprobe load curve for an optimized mixture at a given tip temperature with cryolesion development time and size. These findings can be summarized as follows:

1) For a mixed gas JT cryosurgical probe, there is a trade-off between the ultimate cooling power that can be achieved and load temperature. As load temperature decreases, the available cooling power decreases as well.
2) The primary factor influencing cryolesion development is the steady state operating temperature and refrigeration power provided by the cryoprobe (i.e. the point at

which heat transfer due to metabolic heat generation and blood perfusion from the surface of the cryolesion balances that provided by the cryosurgical system).

These findings are summarized in Figure 1-10. Using the thermodynamic pinch point model for the cryosurgical probe, one may identify the optimal mixture composition for a given operating point/tip temperature (state 7 from Figure 1-5). For the same mixture, at higher values of steady-state tip temperature, the refrigeration power may only slightly increase. The magnitude of this increase was found to only minimally effect treatment time (to steady-state iceball growth). This point is reflected by item (2) above. If the mixture optimization is repeated over a large range of cryoprobe tip temperatures, a line representing the 'best mixture locus' can be formed. The cryolesion model may then be used to determine the different steady state cryolesion sizes and tip temperatures resulting from changes in refrigeration power. The intersection of these two curves, the 'best mixture locus' and 'steady state refrigeration power', yields the largest possible cryolesion. Fredrickson (2006) went on to verify this work experimentally using a single stage, argon gas based cryosurgical system.

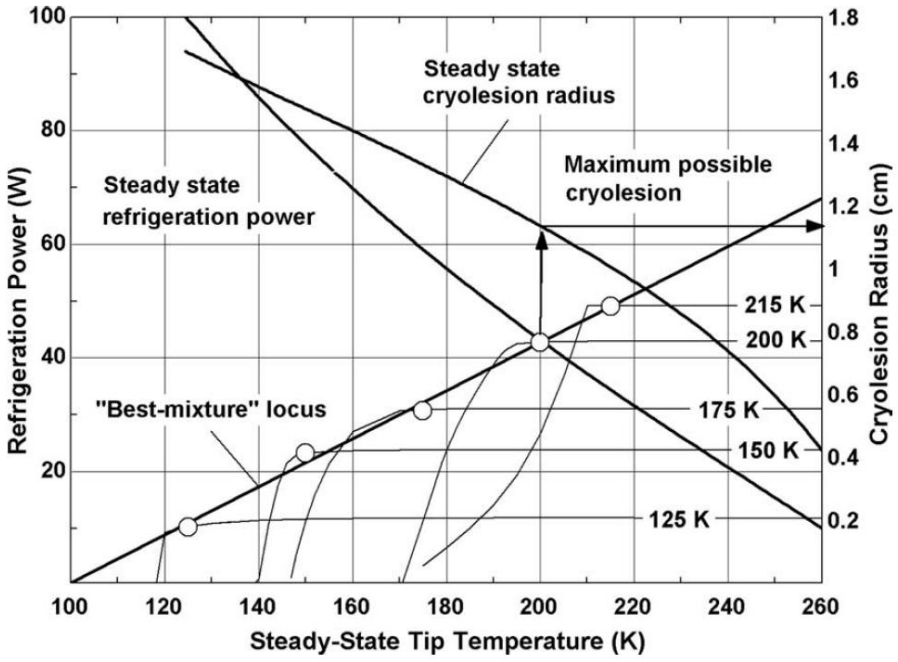

Figure 1-10: Refrigeration power and cryolesion radius as a function of steady-state tip temperature. The intersection between the 'best-mixture locus' and steady state refrigeration power curves represent the largest possible cryolesion that can be produced (Fredrickson, 2004).

1.3.2 Precooled Mixed Gas Cycles

Skye (2011) constructed an experimental test facility using a commercial two stage mixed gas cryosurgical probe. Additional details on the construction and capability of the experimental test setup will be presented in chapter 2. Using experimental data, an empirical correlation was developed relating the heat exchanger conductance for a synthetic refrigerant blend to the physical length of the finned heat exchanger tubing. Detailed information on the development and use of this correlation for the purposes of this research will be presented in section 3.3.1.

The original model revision, and subsequent iteration by Passow (2012), allowed six inputs, including the 2nd stage mass flow rate and the 2nd stage compressor suction and

discharge pressures. The model could be used to provide independent optimization of the mixture composition for a given operating point. As shown in Figure 1-11, the model did a good job of predicting system response, specifically for values of input load less than 15 [W] (errors for greater values of input load were largely attributed to an overly conservative estimate of the precooler effectiveness).

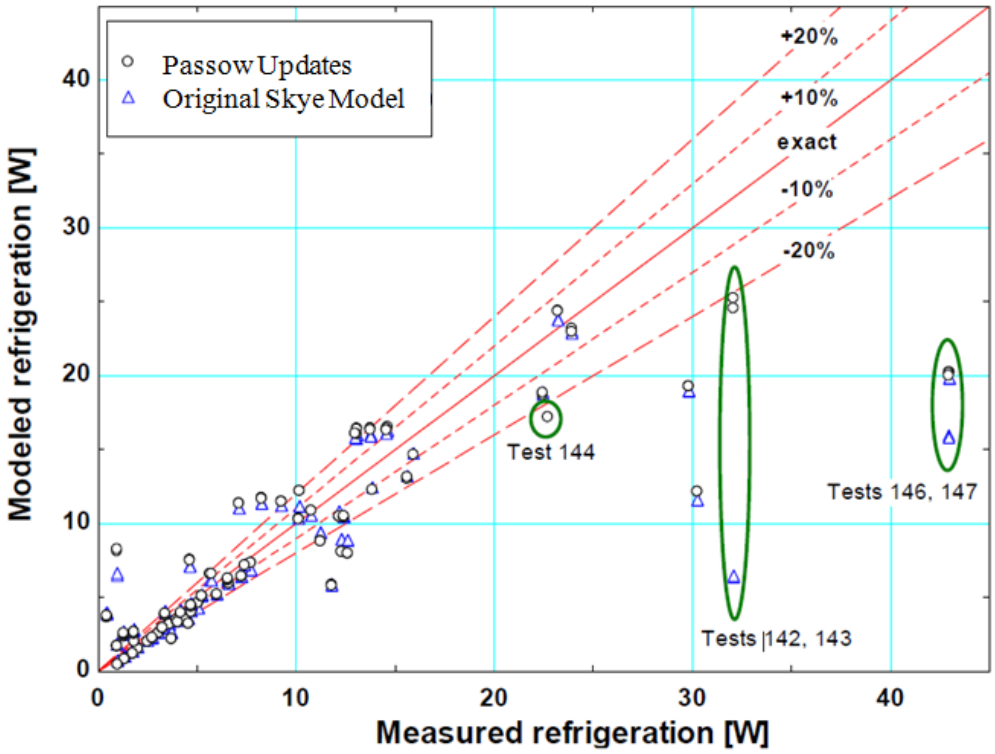

Figure 1-11: Modeled refrigeration power compared to measured refrigeration power. Results from two different model revisions are presented (adapted from (Passow, 2012)).

1.4 Research Objectives

This work seeks to build upon previous research of a precooled mixed gas Joule-Thomson cryosurgical probe. The main objectives of this research can be summarized as follows:

1) Formulate a predictive model for the two stage cryoprobe including correlations obtained from previous work. This model should allow for system optimization from the standpoint of a designer (based upon the operating boundaries of the system only).
2) Verify and improve the predictive capability of the model through experimentation with a precooled mixed gas cryosurgical probe.
3) Experimentally demonstrate the use of the model to select the best operating point for the JT cycle (2^{nd} stage) given compressor and heat exchanger specifications.

The primary focus of previous research was cycle optimization via modification of the charged mixture composition. As detailed in section 1.3.2, work conducted by Skye (2011) included a characterization of an actual precooled mixed gas JT cycle, providing for a more physics based prediction of experimental system outputs. However, the model was never verified outside of the range of experimental data used to develop the empirical correlations and was again based on optimization of the working mixture blend. From a design perspective, mixture composition is only one of many independent cycle parameters that need to be considered. For example, system charge pressure and orifice diameter also have a significant impact on cryoprobe performance and their optimum value likely varies with the concentration of different constituents. Furthermore, as very few inputs (cycle state points) are known prior to system operation, the model should allow for use based only on the operating boundaries for a given design. The primary goal of this research is to formulate a model which takes into consideration all of the relevant parameters (for a given compressor

and recuperator size), in order to enable a design based approach to obtaining the most effective cryosurgical probe.

In addition to the above, the majority of experimental data collected from the two stage cryosurgical probe in past research required the use of either the 2nd stage bypass valve or high pressure isolation valve (to modify the pressure drop over the compressor and system mass flow rate, respectively). This was done in an effort to provide accurate system characterization over a large range of operating conditions, as the jewel orifice is difficult to interchange. Thus, few data points are representative of the "as-built" cryoprobe application in a surgical environment. As the purpose this research is to determine the optimum operating condition for experimental cycle analyzed, additional data must be collected in order to accurately map the response of the cryoprobe to changes in various inputs.

2 Experimental Test Facility

2.1 Test Facility Overview

In order to evaluate the predictive capabilities of the model, outputs are compared directly to experimental data from a fully instrumented precooled mixed gas cryosurgical probe (donated for the purposes of this research by American Medical Systems). As described in section 1.2, the precooling and recuperative heat exchangers for the commercial unit are enclosed within an evacuated stainless steel housing. Figure 2-1 below shows the disassembled probe, revealing the coiled fin recuperator tubing and the 1/8 in. diameter stainless connections normally enclosed within the plastic handle at the base.

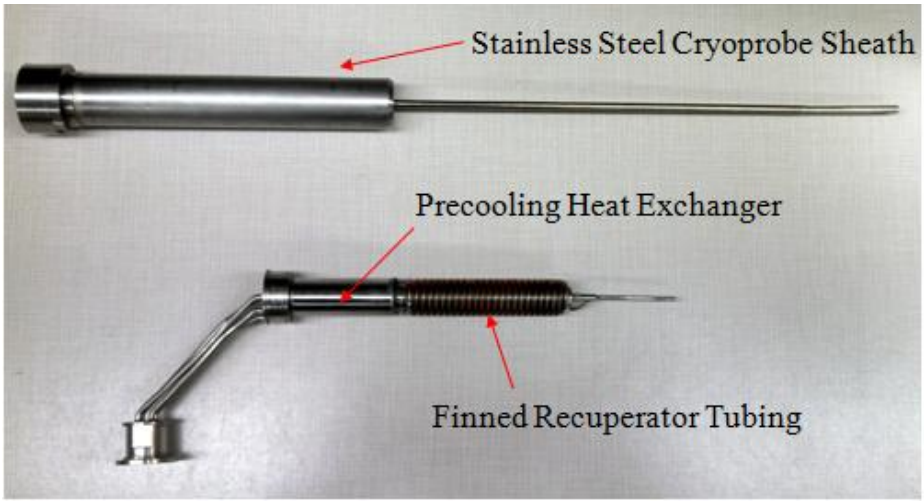

Figure 2-1: Two stage cryosurgical probe.

In order to fully resolve the fluid condition at different cycle operating points during operation, the cryoprobe needed to be modified. A detailed review of these modifications (and overview of the fabrication of the test facility including heater wiring diagrams and in-stream PRT construction) may be found in Chapter 4 of Skye (2011). In order to ensure the accurate calculation of relevant system performance metrics from the experimental data, an uncertainty analysis was conducted. This analysis guided the selection of measurement instrumentation by quantifying the relative sensitivity of these calculated metrics, including the cryoprobe compactness target, $\frac{\dot{Q}_{load}}{UA_{total}}$ and the heat exchanger conductance, to sensor accuracy. An updated system schematic, including modifications made since the original construction of the test facility, is shown in Figure 2-2.

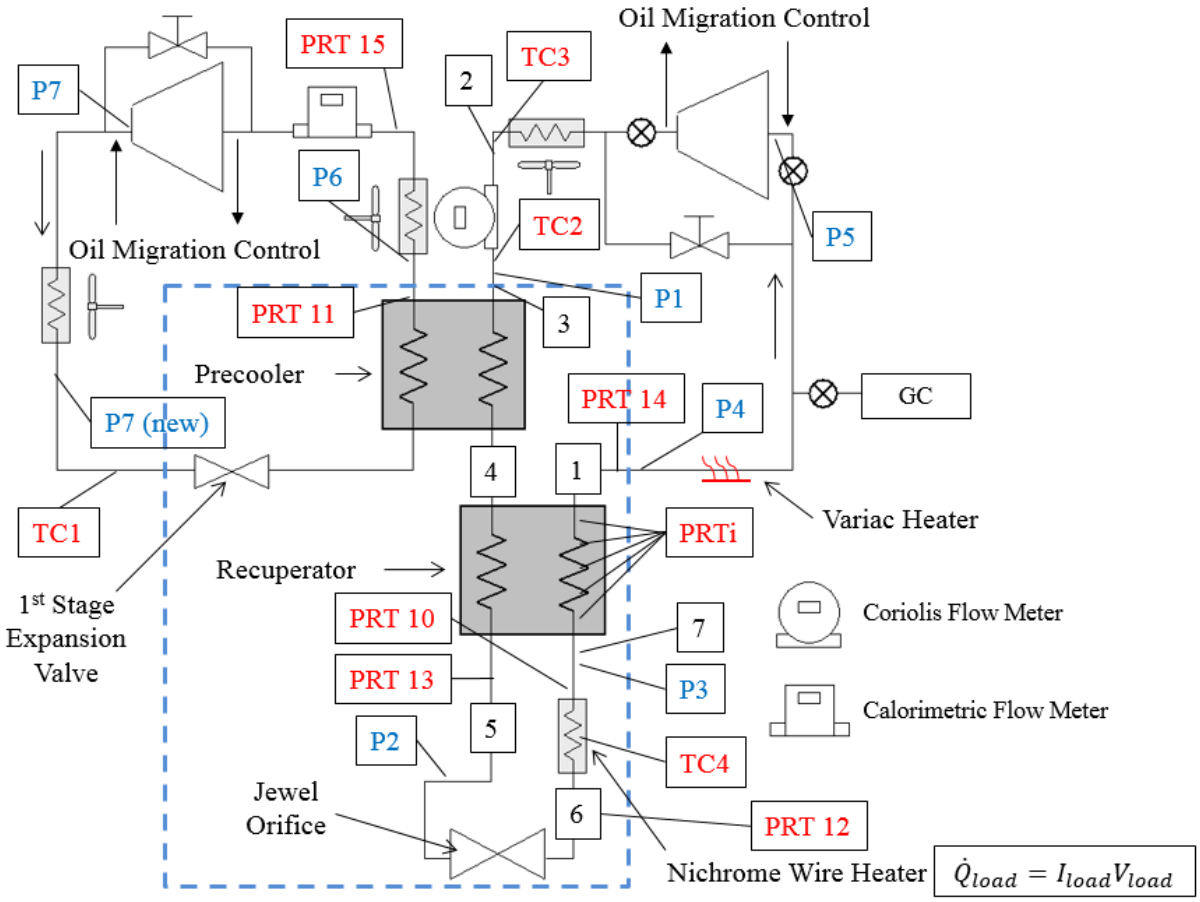

Figure 2-2: Detailed schematic of experimental test facility. Items outlined by the dashed line are contained within a vacuum insulated enclosure.

Cycle components contained within the dashed line are enclosed in a vacuum insulated Dewar to minimize parasitic heat leak due to conduction. Additionally, these components are wrapped in seven layers of multi-layer insulation (MLI) to reduce the effects of radiation from the surroundings. A detailed analysis quantifying the parasitic heat leak due to these effects as well as ohmic dissipation in the load heater current wires is summarized in Table 2-1 below (H. M. Skye, 2011).

Table 2-1: Test facility parasitic heat leak (H. M. Skye, 2011).

Heat source	Magnitude
radiation	0.5 W
conduction	0.26 W
ohmic dissipation	0.014 W
Total	**0.78 W**

Following the discussion presented in section 1.2, the mixed gas refrigerant leaves the compressor at high pressure and enters the Coriolis flow meter. The meter is placed on the high pressure side of the cycle, before the precooler, to ensure single phase flow operation. The flow then enters the precooling heat exchanger at near ambient temperature (a condition facilitated by the use of the air aftercooler near the compressor). After passing through the tube side of the recuperator, the flow is expanded through an interchangeable jewel orifice. For all tests conducted in this research a 0.175 in. diameter orifice is utilized. A nichrome wire heater wrapped around a section of ¼ in. stainless steel tubing simulates the biological thermal load before the refrigerant mix passes through the shell side of the recuperator (energized using a Lakeshore 332 temperature controller which interfaces with the data acquisition system). The temperature profile throughout the recuperator is resolved using platinum resistance thermometers, diametrically opposed and evenly spaced along the length of heat exchanger as detailed in Figure 2-3 below.

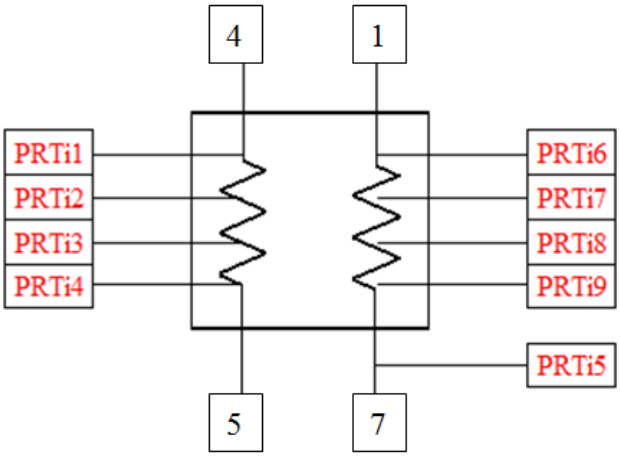

Figure 2-3: Schematic detailing the location of platinum resistance thermometers along the shell side of the recuperator

In order to verify the mixture composition at steady state operating conditions, a gas chromatograph (GC) is utilized on the low pressure side of the 2nd stage cycle just before the flexible compressor return line. A heater, external to the Dewar, ensures that the mixture is fully vaporized before sampling. Without this heater, liquid phase constituents could remain in the low pressure tubing before the sample line resulting in inaccurate composition measurements. A mV/V style pressure transducer is included as part of the commercial cryoprobe unit to measure the compressor suction pressure for the 2nd stage. This style of sensor has an output that is proportional to the excitation/supply voltage provided to the unit. A similar style sensor is utilized on the high pressure side of the 1st stage compressor.

The first stage cycle utilizes a pure synthetic refrigerant, R410a, and remains at a constant value of charge pressure for the experiments conducted in this research (the experimental operating range is specified in section 5.2.1). A condenser cools the superheated refrigerant to approximately room temperature before it enters the Dewar. After

the refrigerant passes through the precooling heat exchanger, it passes through a secondary evaporator, external to the Dewar, to prevent any liquid from entering the compressor.

Past issues with oil migration to the coldest portions of the system resulted in several design iterations. The current adaptation is not pictured for either the 1st or 2nd stage cycles in Figure 2-2. Instead the reader is directed to section 2.2.1 of Passow (2012). Similar consideration has been given to moisture management, resulting in a detailed operating procedure for modifying system charge pressure or 2nd stage refrigerant composition.

2.2 Test Facility Modifications/Improvements

Several modifications have been made to the experimental system since its original construction by Skye (2011). These include replacement of the 1st and 2nd stage calorimetric flow meters with Coriolis flow meters for improved measurement accuracy as well as modifications to the original oil management system (Passow, 2012). Test facility improvements made as a part of this research are broken down for each cycle in sections 2.2.1 and 2.2.2.

2.2.1 1st Stage (PCC) Cycle

Prior to the use of the experimental test facility, the Coriolis flow meter that had been installed on the precooling stage was removed due to high accuracy sensor requirements for a related research project. The mass flow rate through the 1st stage cycle is required for the calculation of the precooler heat exchanger conductance and subsequent characterization of its physical size by the predictive model. However, the model formulation described in Chapter 3 assumes that the temperature at state 4 (see Figure 2-2) may be fully defined by the saturation temperature of the 1st stage refrigerant only (reference section 3.3.3).

$$T_4 = T_{sat}(R410A, P = P_{low,1st}) \quad (2.1)$$

This assumption eliminates the need for a measured flow rate in the 1st stage. Nonetheless, in consideration of possible future model improvements, a calorimetric flow meter (Omega model#FMA1741ST-EPDM) was installed in place of the Coriolis unit. Since the calorimetric flow meter is calibrated by the manufacturer for pure nitrogen at standard conditions, it must be corrected for the specific heat of the working fluid. Please refer to Skye (2011) for additional details on this correction.

The calorimetric and Coriolis flow meters were compared using nitrogen over a range of flow rates prior to installation. The results are shown in Figure 2-4. The blue lines highlight the 1st stage flow rate bounds for the tests conducted in this research. Uncertainty bands for the Coriolis meter are indicated by the red dashed lines. The instrument uncertainty for the Coriolis flow meter, an Endress+Hauser ProMass 83A, is provided by the manufacturer as ±0.50 % relative to the reading (o.r.) for flow rates above 0.278 g/s. The lowest flow rate used in the test detailed by Figure 2-4 is 0.3602 g/s, but as a result of errors introduced via the use of a shunt resistor to measure output voltage as well as that due to the resolution of the data acquisition system (DAQ), a conservative uncertainty of 1% o.r. is assumed. The measurement uncertainty (rms error) of the calorimetric flow meter is due to the combined effects of instrument uncertainty and the resolution of the data acquisition system, U_{ins} and U_{res}, respectively. The instrument uncertainty can be determined by combining the ±1.5% full scale accuracy and ±0.5% full scale repeatability errors reported by the manufacturer.

$$U_{ins} = \sqrt{U_{acc}{}^2 + U_{prec}{}^2} \tag{2.2}$$

The uncertainty due to the resolution of the 16-bit NI6036E data acquisition system is equal to the minimum change in the measured quantity, in this case the flow rate that can be captured by the 6036E:

$$U_{res} = \frac{Input\ Voltage\ Range}{2^{N_{bits}}}\left(\frac{Max_{meas}}{Range_o}\right) \tag{2.3}$$

where the input voltage range is equal to 20 V (the input range is ±10 V), Max_{meas} is the measurement range of the calorimetric flow meter, 80 stdLN2/min, and $Range_o$ is the output voltage range (0-5 V).The resulting uncertainty in flow rate measurement can then be calculated using equation (2.4) (=1.265 stdLN2/min). The error bars on each data point also include the uncertainty resulting from the calculation of mixture properties at ambient conditions (±0.5°C and ±0.05 mmHg) needed for the correction of specific heat, yielding a cumulative uncertainty of 0.026 g/s.

$$U_{cal} = \sqrt{U_{ins}{}^2 + U_{res}{}^2} \tag{2.4}$$

.

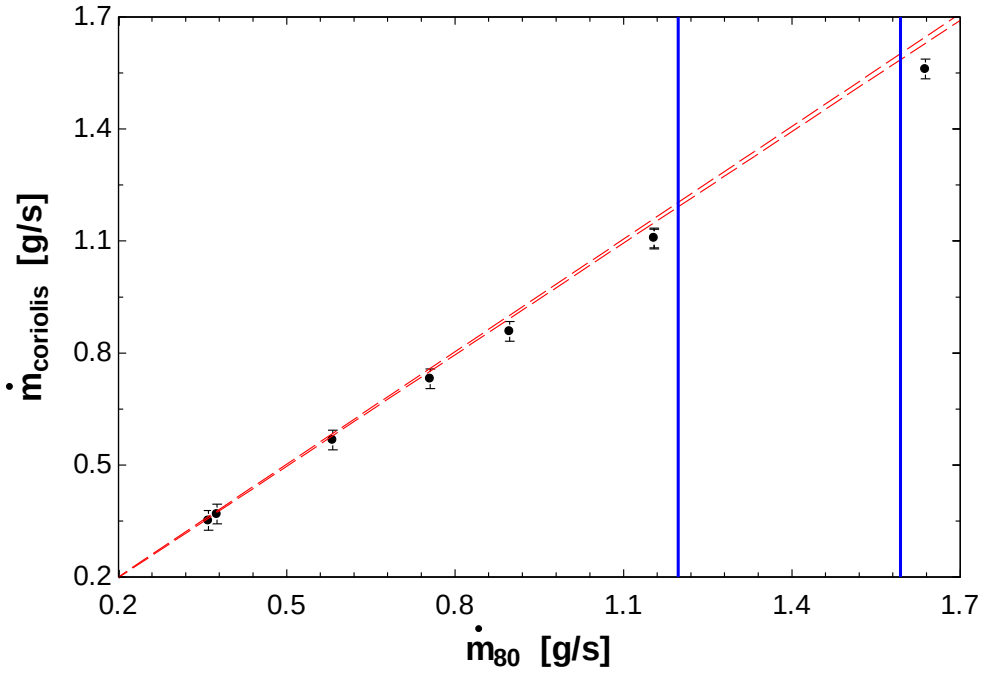

Figure 2-4: Eight point comparison between the Coriolis and calorimetric flow meter. Uncertainty in the Coriolis reading is detailed by the dashed lines. Solid lines highlight the operating range of the flow meter for the tests conducted in this research.

After the calorimetric flow meter was installed and the cycle charged with R410A, significant errors in the high side pressure transducer reading, P7 from Figure 2-2, were observed. During the initial system startup, the pressure repeatedly spiked over 400 psig, above the upper operating limit established by the system manufacturer. In order to correct this issue, an Omega PX309-500G5V pressure transducer with an instrument uncertainty of ±2% of full scale (reported total error band) was installed after the condenser for the 1st stage (improved uncertainty as compared to the original meter). This sensor is represented by P7 (new) in Figure 2-2. It was verified by the manufacturer that exposure to vacuum, specifically during the triple evacuation procedure required for refrigerant change out, would not result in damage to the sensor. Again, the overall uncertainty in pressure measurement is due to a combination of instrument error and the resolution of the NI6036E data acquisition

system. Adjusting equation (2.3) for the maximum pressure and output voltage range of the sensor (Max_{meas}=500 psig, and $Range_o$=5 V, respectively), the cumulative uncertainty is calculated as ±10psig. This uncertainty could be reduced by future calibration. In addition to the added sensor, a VCR bypass valve was installed on the 1st stage cycle and a compressed air back flush through the Dewar side of the system was performed. The purpose of the compressed air-back flush was to remove any oil/particulates that may have accumulated at the tip of the expansion valve. The VCR bypass valve, which was installed just after the flexible cryoprobe lines from the compressor cabinet, could be used in the future for independent regulation of the 1st stage mass flow rate and provides added protection against a compressor dead head condition in the event of line plugging or freeze up at the tip of the expansion valve. These changes are pictured in Figure 2-5 below.

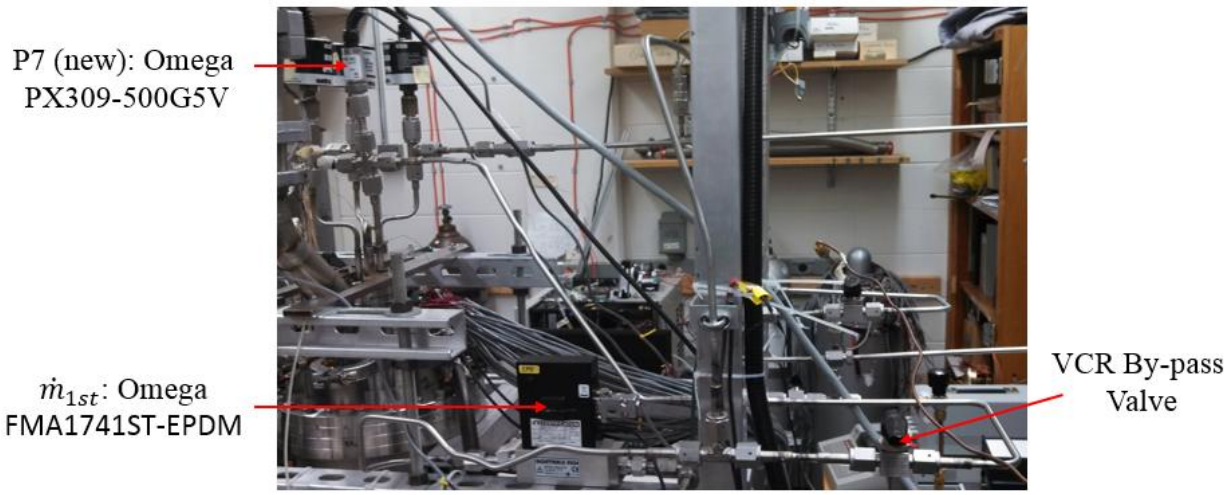

Figure 2-5: Picture detailing modifications made to the 1st stage cycle for the cryoprobe test facility.

2.2.2 2nd Stage (GMC) Cycle

Some minor modifications were also made to the second stage cycle during the experimental test phase. In an effort to improve measurement accuracy, pressure transducer P1 (reference Figure 2-2) was removed and calibrated using a dead weight tester. After reinstallation a calibration of the remaining pressure sensors was performed *in situ* using the reference transducer. During preliminary experimental testing, significant drift errors, as large as 0.4 psig/hr, were observed from the P3 measurement sensor. As a result of this, the pressure sensor was removed and replaced with a comparable model, a Setra Model 206 (0-500 psig measurement range). This new sensor was then used as a reference in a second *in situ* pressure transducer calibration for the 2nd stage cycle.

A detailed overview of the absolute measurement uncertainty for all remaining cycle instrumentation, including P3, is presented in Table 2-2. In addition, a three point test to determine the uncertainty in circulating mixture composition was conducted at two different steady state operating conditions for the cryoprobe. Both operating conditions were at relatively low values of input load to ensure that thermodynamic equilibrium was maintained regardless of the small changes in the 2nd stage charge pressure from sampling. The standard deviation from the mean in these three values is used as an estimate in the uncertainty of the reading output from the gas chromatograph by the integrator.

Table 2-2: List of measurement instrumentation used in the experimental test facility (adapted from Skye (2011)).

Measurement	Label on Figure 2-2	Manufacturer	Part #	Uncertainty
Temperature - PRT	PRT 10, 11, 12, 13, 14, and 15	Lakeshore	PRT-111	±0.5 K
Temperature - PRT	PRTi1-9	Lakeshore	PRT-111	±0.5 K
Temperature – thermocouple	TC 1, 2, and 3	Lakeshore	9006-004	±1.0 K
Mixture high pressure	P1 and P2	Setra	206-500G	±3.0 psi
Mixture low pressure	P3 and P4	Setra	206-100G	±1.5 psi
Mixture low pressure	P5	Ashcroft	-	±1% relative
Pure fluid high pressure	P7 (new)	Omega	PX309-500G5V	±10.0 psi
Pure fluid low pressure	P6	Setra	206-100G	±1.5 psi
1st stage mass flow	Calorimetric flow meter	Omega	FMA1741ST-EPDM	±0.026 g/s
2nd stage mass flow	Coriolis flow meter	Endress+Hauser	Promass 83A	±1% relative
Cryoprobe load	$\dot{Q}_{load}$	-	-	±1% relative
Heater voltage	V_{load}	-	-	±0.005 V
Heater current	I_{load}	-	-	±0.002 A
Mixture composition	GC ($\bar{y}_{2nd}$)	HP	5890 Series II	±0.027 (R14 mole fraction)

3 Empirical Model Development and Revision

3.1 Objectives

One of the goals of this research was to determine the effects of cryoprobe system component selection on mixed gas Joule-Thomson cycle performance *a priori* (i.e. without requiring experimental measurements). In order to accomplish this objective, an iterative thermodynamic model of the second stage of the cycle was formulated in EES (Klein, 2013a); this mode built upon those previously developed by Skye (2011) and Passow (2012). The evolution of the Joule-Thomson cycle model began with work completed by Keppler et al. (2004). Its usefulness was verified in the design of a single-stage cryosurgical system by Fredrickson (2004) who incorporated a numerical model which predicted the development of a cryolesion in living tissue. This improvement allowed for mixture optimization based on medically relevant quantities such as the extent of cell death induced, as opposed to less directly applicable thermodynamic figures of merit such as refrigeration power at a specific temperature. The primary focus of these early models was optimization of the mixture composition and the relationships\tradeoffs between cryoprobe tip temperature and cooling effect.

The first empirical model for a two stage Joule-Thomson cycle based on experimental data was formulated by Skye (2011). It was predicated on the same numerical heat exchanger analysis for the recuperator that was implemented by Keppler et al. (2004) but utilized experimentally determined conductance correlations to approximate the thermodynamic behavior of a commercial cryoprobe of given physical specifications. Passow (2012) expanded the model to include a more physics-based prediction of the pressure drop through

both the precooling and recuperative heat exchangers. A compressor map for the mixed gas cycle was also developed which related system operating pressure and suction side thermophysical fluid condition to the mass flow rate of the 2nd stage mixture. This yielded a more robust cycle optimization but did not include a provision for correlating the cycle pressure drop to orifice diameter or system static charge pressure.

In an effort to further verify previous work and expand upon it, a revised thermodynamic model of the 2nd stage cycle is the focus of this report. Section 1.2 details the underlying numerical heat exchanger analysis that allows for a prediction of the recuperator conductance. The addition of empirical correlations used to relate model outputs to cycle component geometry are discussed in Section 1.3. Section 1.4 details the iterative solution procedure as well as techniques implemented to ensure model convergence over a wide range of cycle operating conditions. Additionally, a brief comparison of thermodynamic property databases and computation techniques is included in Sections 1.2.4 and 1.2.5.

3.2 Formulation of MGJT 2nd Stage Model

3.2.1 Analysis Summary

This section describes the ε-NTU heat exchanger analysis required to most accurately model the thermodynamic behavior of the mixture as it passes through the recuperator. Initially a simple pinch point model is presented so that a preliminary design analysis can be conducted. Thereafter, a geometric model relating the conductance of the heat exchanger under consideration to its physical size and operating conditions may be used to achieve numerical convergence directly. A brief overview of the empirical correlation used here is presented.

3.2.2 Cycle Overview

A schematic of the MGJT system with measurement instrumentation is detailed in Figure 3-1. Note the modification to the numbering scheme identifying each sensor as compared to Figure 2-2. This is done to avoid confusion when referencing state numbers during calculations. Highlighted by the dashed line is the portion of the second stage cycle analyzed by the model, which spans from the inlet of the recuperative heat exchanger to the suction side of the compressor, states 1 along with 4 through 7. Basic assumptions required for this analysis include: isenthalpic expansion across the JT orifice between states 5 and 6, and negligible pressure drop or heat transfer within the piping between system components. The first assumption is a common one for throttling valves or restrictors (S. A. Klein & G. Nellis, 2012) and also follows directly from previous experimental analysis (H. M. Skye, 2011). The second is justified by ensuring the ratio of tube length to diameter for the connective piping is much smaller as compared to the heat exchangers.

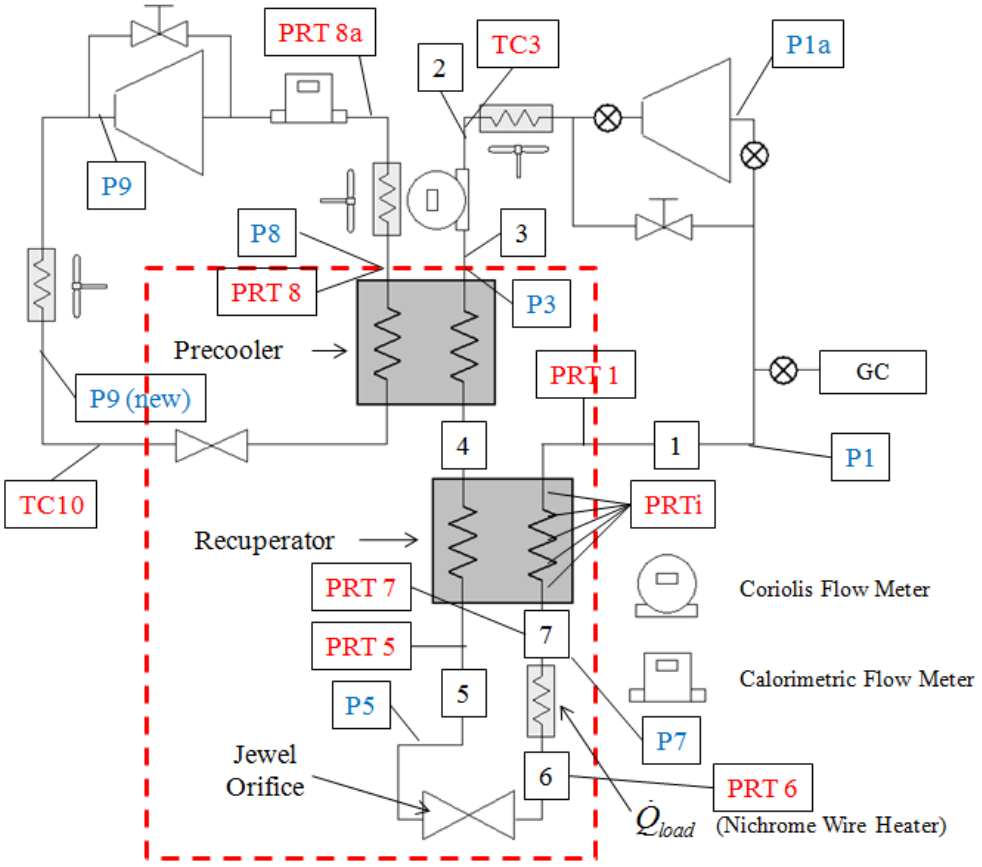

Figure 3-1: System schematic highlighting the second stage of the heat exchanger and integrated measurement instrumentation.

The first stage, represented as states 8 and higher, is a simple JT refrigeration cycle utilizing a pure synthetic refrigerant. The amount of cooling provided by this cycle is based on a combination of factors including the pressure drop through the heat exchanger piping and precooler conductance. The latter will depend largely on the convective heat transfer coefficient of the 2nd stage mixture which varies with molar composition and the pressure at state 3 (as discussed in Section 1.3.3).

3.2.3 Thermodynamic Heat Exchanger Model

The cooling load for the 2nd stage cycle is entirely limited by the minimum enthalpy difference that can be achieved across the operating temperature range of the recuperative heat exchanger (H. M. Skye, 2011). For a pure fluid that does not experience a phase or pressure change at any point within the heat exchanger, evaluation of the pinch point temperature difference is trivial. However, a simple effectiveness-NTU or log-mean-temperature difference (LMTD) approximation becomes exceedingly inaccurate when the working fluid experiences large changes or discontinuities in specific heat with temperature. In such a case, the pinch point cannot be assumed to occur at the inlet or outlet of the recuperator. In order to account for this, it has been shown that an accurate solution may be obtained via discretization of the heat exchanger into smaller sub-sections, each of which account for an equal portion of the total heat transferred (Nellis & Klein, 2009). The resolved effectiveness-NTU calculations allow for an approximation of the specific heat capacity at several locations throughout the heat exchanger and thus a more physically accurate solution.

Discretization of the heat exchanger begins by assuming a temperature difference on one side of the recuperator and the following cycle operating parameters: cryoprobe load temperature, T_7; the temperature of the precooled mixture entering the recuperative heat exchanger, T_4; the compressor suction and discharge pressures, $P_{low,2}$ and $P_{high,2}$, respectively; and the molar composition of the 2nd stage refrigerant mixture. For the purposes of this procedure, the hot side/warm end temperature difference is selected.

$$T_1 = T_4 + T_{rec,h,diff} \tag{3.1}$$

For this portion of the analysis, the pressure drop across the precooling and recuperative heat exchangers is assumed to be negligible, thus the enthalpy at states 1, 4 and 7 can be determined (h_1 is shown here directly for demonstration).

$$h_1 = enthalpy(T_1, P_{low,2}) \tag{3.2}$$

Next, an energy balance is implemented on the cold side of the recuperator as depicted by CV1 in Figure 1-2 below in order to determine the total amount of heat transfer per unit mass flow rate.

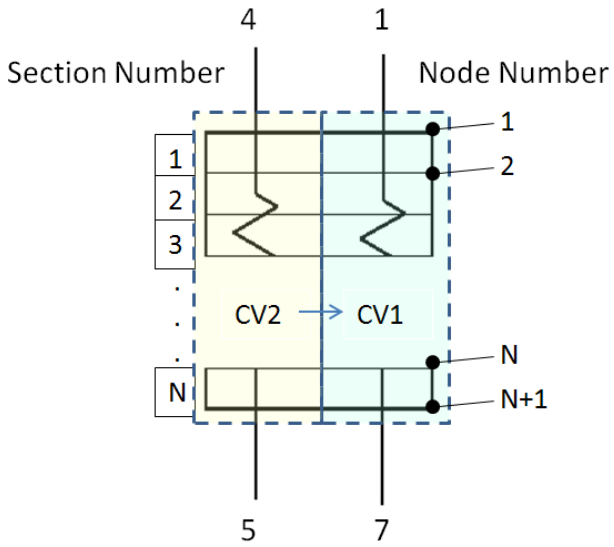

Figure 3-2: Recuperative heat exchanger divided into N sub-sections with N+1 nodes.

$$\frac{\dot{Q}_{rec}}{\dot{m}} = (h_1 - h_7) \tag{3.3}$$

A corresponding energy balance is performed over CV2 in Figure 1-2 to determine the enthalpy at state 5, from which the temperature can be determined.

$$h_5 = h_4 - \frac{\dot{Q}_{rec}}{\dot{m}} \tag{3.4}$$

The amount of heat exchange calculated via an energy balance over the cold side of the recuperator is then divided evenly among the N recuperator sections. The number of divisions required is related to the mixture composition and experimental operating conditions. Thus an analysis must be performed to verify the minimum number of sections needed for model stability and desired accuracy. To accomplish this, a key system performance metric, the cryoprobe cooling load is examined. Distribution of the heat transferred within each section of the recuperator is accomplished as follows:

$$\frac{\dot{Q}_{rec}}{\dot{m}}[i] = q_{rec}[i] = \frac{\dot{Q}_{rec} / \dot{m}}{N} \tag{3.5}$$

An energy balance is then performed over the hot and cold side of each sub-heat exchanger in order to determine the spatially resolved recuperator temperature profile. It is important to note that *i=1* corresponds to the warm end of the recuperator, i.e. node 1 is located on the same end as states 1 and 4 in Figure 1-2.

Hot side (for *i=1..N+1*):

$$h_{rec,h}[i] = h_{rec,h}[i-1] - \dot{Q}_{rec} / (N * \dot{m}), \tag{3.6}$$

$$T_{rec,h}[i] = temperature(P_{rec,h}, h_{rec,h}[i]) \tag{3.7}$$

Cold side (for *i=1..N+1*):

$$h_{rec,c}[i] = h_{rec,c}[i-1] - \dot{Q}_{rec} / (N * \dot{m}), \tag{3.8}$$

$$T_{rec,c}[i] = temperature(P_{rec,c}, h_{rec,c}[i]) \tag{3.9}$$

There are two methods that can be implemented in order to calculate the specific heat in each section; the specific heat capacity is defined as the partial derivative of enthalpy with respect to temperature at constant pressure. Since the pressure change over an individual section is small, one may simply determine the average of the specific heat at either end of the section. A more computationally efficient and straightforward method is presented below. This calculation is repeated to determine the average specific heat capacity for the cold side.

$$\frac{\dot{C}_{rec,h}}{\dot{m}}[i] = c_{rec,h}[i] = \frac{h_{rec,h}[i] - h_{rec,h}[i+1]}{T_{rec,h}[i] - T_{rec,h}[i+1]} \quad for\ i = 1..N \tag{3.10}$$

In addition to the specific heat capacity, the nodal temperature distribution can be utilized to calculate the minimum temperature difference or pinch point within the recuperator.

$$\Delta T_{pp,rec} = \min\left(T_{rec,h}[i] - T_{rec,c}[i]\right) \quad for\ i = 1..N+1 \tag{3.11}$$

The pinch point temperature difference is related to the physical size of the heat exchanger and, as indicated in Section 1.2.1, it may be used as a model constraint early in the development process to ensure proper formulation of the numerical model.

In order to determine the conductance of each heat exchanger section, the effectiveness must be calculated. This is accomplished by taking the heat transferred in each section and dividing it by the both the maximum temperature difference within the heat

exchanger and the minimum specific heat capacity for that section (between the cold and warm fluid streams).

$$\varepsilon_{rec}[i] = \frac{q_{rec}[i]}{\min\left(c_{rec,h}[i], c_{rec,c}[i]\right) * \left(T_{rec,h}[i] - T_{rec,c}[i+1]\right)} \quad for\ i = 1..N \tag{3.12}$$

The corresponding number of transfer units (NTU) is calculated using correlations presented in Nellis and Klein (2009) for a counter flow heat exchanger configuration. The conductance of each section is then computed directly.

$$\frac{UA_{rec}}{\dot{m}}[i] = NTU_{rec}[i] * \min\left(c_{rec,h}[i], c_{rec,c}[i]\right) \quad for\ i = 1..N \tag{3.13}$$

Once the fluid stream passes through the cold side of the recuperator, it expands isenthalpically (according to the first assumption in 1.2.2), from states 5 to 6. An energy balance over the expansion orifice yields the following:

$$h[5] = h[6] \tag{3.14}$$

Thus for a given (assumed) value of the recuperator warm end temperature difference, all thermodynamic states are fully defined. The potential difference between the enthalpy at states 6 and 7 determines the primary figure of merit, the cryoprobe cooling load.

$$\frac{\dot{Q}_{load}}{\dot{m}} = h[6] - h[7] \tag{3.15}$$

Note that an optimized cryosurgical probe will maximize cooling capacity while minimizing heat exchanger surface area (or size). However, for a predefined pinch point temperature difference or geometric size, these two variables are interrelated.

As previously indicated, model accuracy and stability are dependent on the number of sections used for the analysis as well as the thermodynamic condition of the fluid flowing through the hot and cold sides of the recuperator. For a nominal mixture and operating conditions, the mixture might enter the heat exchanger with quality near 1 (an optimized test case will be presented in subsequent sections). As the fluid moves through the hot side of the recuperator, the quality will decrease until it is expanded isenthalpically in the orifice (just before reaching the load location). As will be shown in Section 1.3.1, the conductance varies most appreciably inside of the 2-phase regime. Therefore, this analysis should take into consideration the location of the vapor dome of the mixture for a given operating point as conductance variation results in the largest model inaccuracy and instability (due to low section number). A study may then be conducted to verify the optimal number of sub-heat exchangers required for a given system analysis. Such a study is demonstrated in Figure 1-3 below.

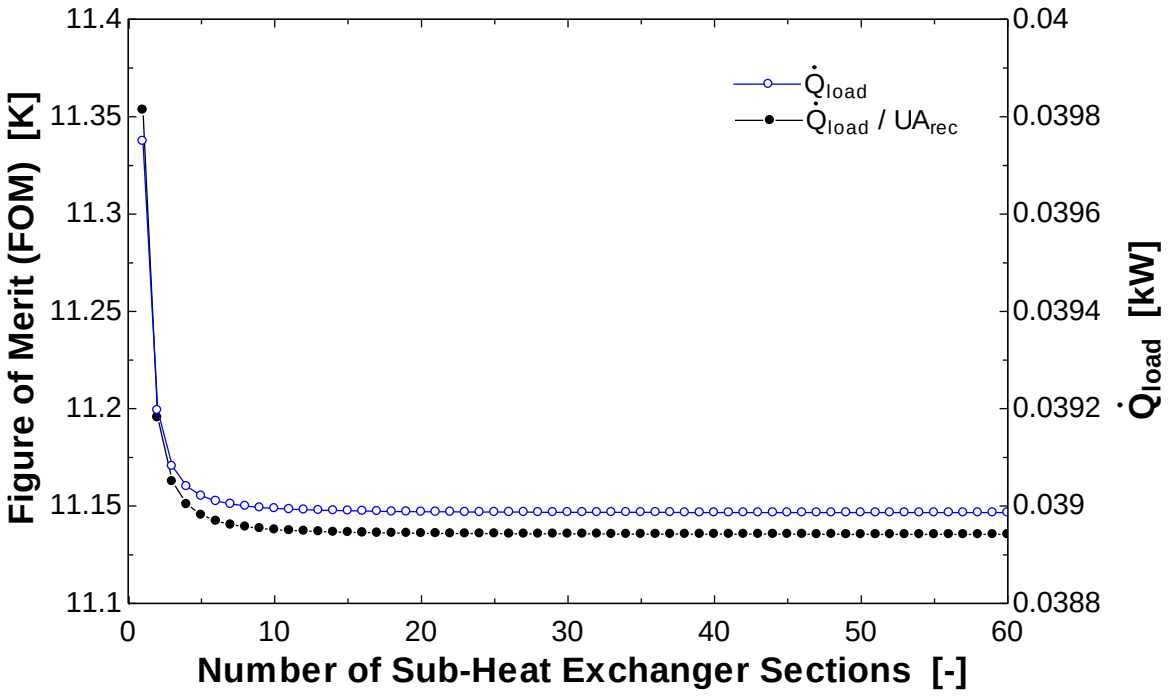

Figure 3-3: Cryoprobe cooling load and cooling load normalized by recuperator conductance as a function of the number of sub-heat exchanger sections (using argon as the working fluid)

The plot shows, for a typical operating condition, that as the number of sections increases the cooling load decreases until model stability is achieved. The figure of merit used here is the cryoprobe cooling load divided by the recuperator conductance. Note that for different operating conditions the shape of this function will change. Working fluids with multiple components will also exhibit a slightly different response depending on the molar mixture composition. Engineering judgment should be used in selecting the optimal number of sections for a given operating range. Figure 1-4 details an analysis on a binary mixture of R14 and R23, with cooling load as a function of the number of sections and R14 concentration (molar).

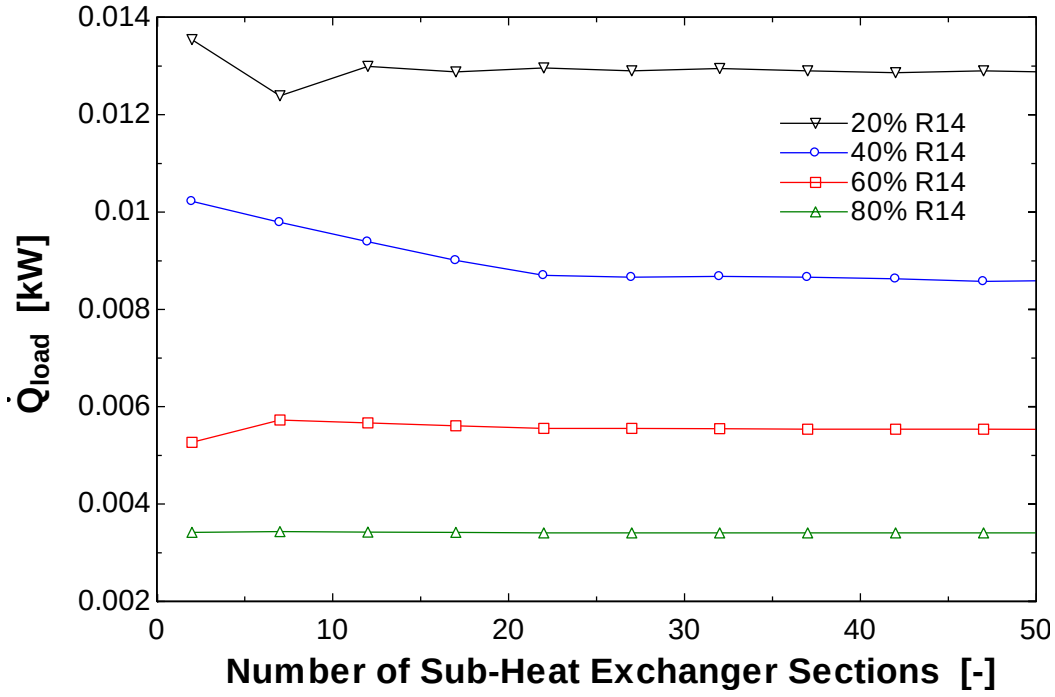

Figure 3-4: Cryoprobe cooling load for 4 different mixture compositions as a function of the number of sub-heat exchanger sections (R14+R23 working fluid)

For a given set of operating conditions, the cooling load achieved increases along with recuperator conductance. This relationship can be observed from Figure 1-3, as the conductance normalization yields no further information with regard to model stability as the number of sections increases. As a result of this only one of the two metrics is required for the purposes of this analysis. For the case shown above, the variation with the number of sub-heat exchangers is relatively small. 15 sections are chosen for further analysis as this provides a good balance between model accuracy and computation time (the error associated with using 15 section is less than 7% for all cases considered based on a 50 sub-section reference).

3.2.4 Thermodynamic Property Database Comparison

A simple extension of the preliminary pinch point model allows the user the ability to analyze a system utilizing a multi-component mixture. Two current mixture property programs may be called as external libraries by EES as of the date of this writing. The first, and most accurate, is the NIST Standard Reference Database 23 or Refprop database (Lemmon, Huber, & McLinden, 2013). This program uses a complex equation of state to determine pure fluid and mixture thermodynamic and transport properties. The second is the NIST Standard Reference Database 4 or Supertrapp version 4 (Ely & Huber, 1992) (referred to subsequently as NIST4). NIST4 utilizes less complex equations of state, i.e. the Peng Robinson and the Extended Corresponding States model. The result is reduced computation time and increased convergence reliability but, as a result of the reduction in accuracy, NIST4 is primarily only utilized for early model debugging or when optimization is time limited.

In order to directly compare the predictive capability of both databases, a procedure was added to the model to generate an array of pressure-enthalpy points that form the saturated liquid and vapor lines for a given mixture and molar composition. This array was coupled with a macro that automatically plots cycle state points and then overlays the vapor dome for the mixture and composition of interest. Figure 1-5 details such a comparison between the two programs.

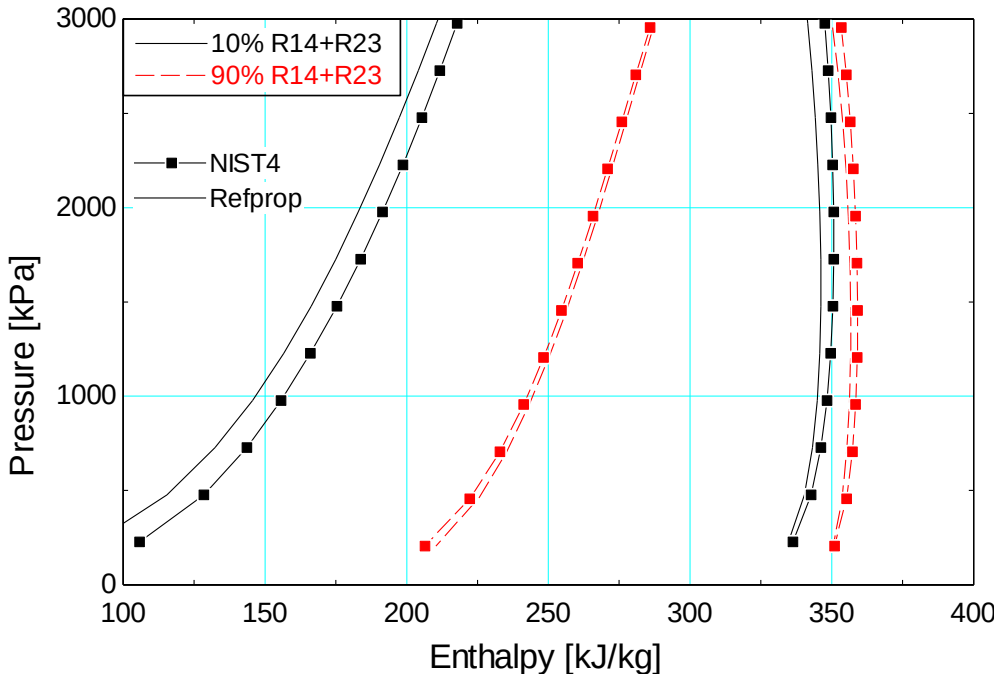

Figure 3-5: Pressure vs. enthalpy plot for an R14-R23 binary pair of the following mixture compositions: (a) a mixture of 10% R14 to 90% R23, and (b) a mixture of 90% R14 to 10%R23.

As can be seen from the plot, the location of the dew point and bubble point lines predicted by each database differs depending upon the mixture composition being evaluated. For mixture (a), NIST4 predicts the bubble and dew point lines at a higher enthalpy/temperature for a given pressure than Refprop whereas for mixture (b) the NIST4 bubble line is actually at a lower value of enthalpy/temperature than Refprop. Previous data presented by Skye (2011) compared the Joule-Thomson effect predicted by NIST4 and Refprop to that obtained experimentally over a range of thermodynamic quality. Results were shown for both a pure fluid and 2 different mixtures. His data demonstrated Refprop's superior predictive capability over NIST4 specifically near the bubble line for the 3 component mixture analyzed. NIST4's tendency to over-predict the location of the dew point line (as shown in Figure 1-5 for both mixture blends) also led to pinch point violations in the experimental model. For this reason,

all empirical relations generated were computed using Refprop exclusively. Therefore, the use of NIST4 in this project is limited to model debugging and time sensitive approximation only.

3.2.5 Interpolation Tables and Computation Techniques

As briefly detailed in section 1.2.4, the complex equation of state utilized by Refprop substantially increases the time required to calculate thermodynamic mixture properties. A quantitative comparison of calculation time between the different databases for a pure fluid (argon) is presented in Table 1-1 below.

Table 3-1: Comparison of model calculation time for a nominal pure fluid test point using Refprop, NIST4, and EES. Modeled test condition: pure fluid: argon; T_4=298.1 [K], T_7=193.2 [K], $P_{low,2}$=1000 [kPa], $P_{high,2}$=19000 [kPa] (absolute pressures – no system pressure drop).

Database	Refprop	NIST4	EES
Computation Time (s)	25.9	5.7	0.7

As can be seen from the table, the amount of time required by NIST4 is approximately 8 times that required for model convergence using EES and more than 30 times greater when using Refprop. It is important to note that EES is not currently configured to calculate thermodynamic properties for mixtures and thus is only presented here for comparison of a pure fluid test point.

Based on the data above it is apparent that the majority of calculation time is spent iterating through the temperature profile in the recuperative heat exchanger in order to achieve a desired pinch point temperature. For the test case presented here, an empirical correlation relating the cryoprobe conductance to the length of finned tubing in each section, as will be described in section 1.3, was used. Two energy balances are required to fully

specify the fluid thermophysical condition at each of the four nodes for each section. The total number of mixture fluid property calls, N_{calls}, is therefore directly proportional to the number of heat exchanger sections, *N#*, multiplied by the number of iterations (modification of the hot or cold side temperature difference, depending on model setup).

$$N_{calls} = 2C_{iterations}(N\#) \tag{3.16}$$

The number of iterations depends primarily on the initial guess values and iteration scheme implemented. For the study detailed in Table 1-1 which utilized the root finding scheme described in section 1.4.2, an average of 720 property calls were required for the recuperative heat exchanger alone. In order to reduce computation time, Keppler et al (2004) utilized enthalpy interpolation tables for the iterative calculation of nodal fluid properties. Skye (2011) incorporated interpolation tables into his model as well, evaluating model accuracy for different values of interpolation table entries via a numerical study. A similar analysis is presented in Figure 1-6 below for this model.

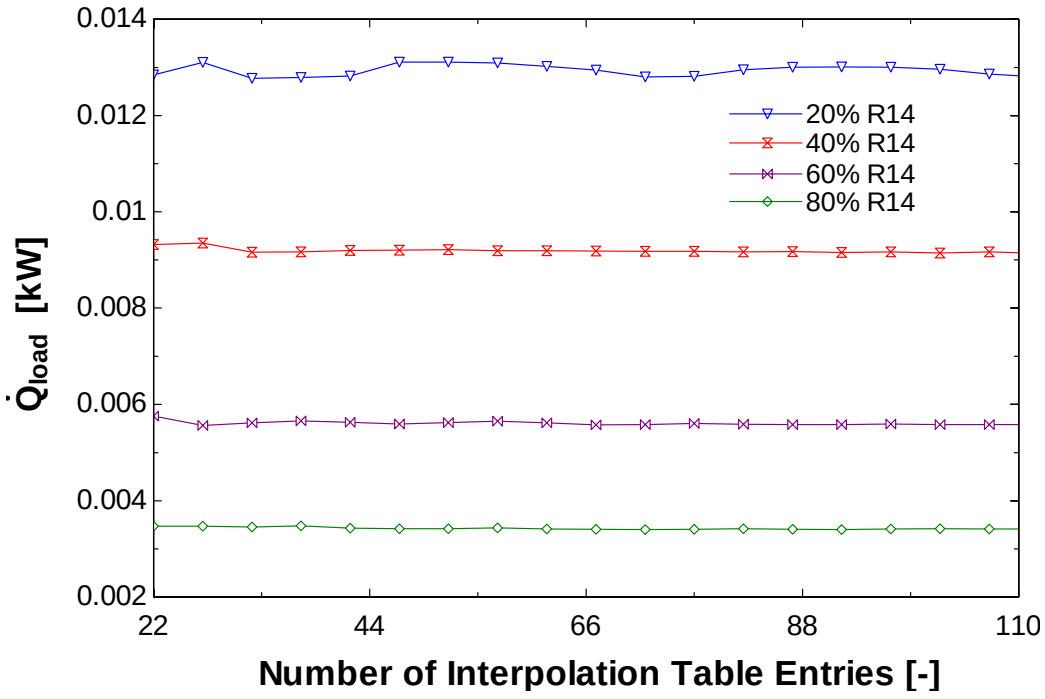

Figure 3-6: Cryoprobe cooling load for four different mixture compositions as a function of the number of interpolation table entries (R14+R23 binary mixture).

As can be observed from Figure 1-6, for the operating point analyzed, there is not significant scatter even below approximately 50 entries. It has been observed, however, while using this model to evaluate operating points with low compressor suction pressure, that an inadequate number of interpolation entries will prevent model convergence. This is as a result of the under-prediction of recuperator length at very low values of the cold side temperature difference. Poorly distributed enthalpy entries at constant pressure reduce the accuracy of the model in predicting the saturated liquid and vapor lines for the fluid which, in turn, can cause an underestimation of the effectiveness for each section. For this reason, when implementing linear interpolation tables, it is recommended that no fewer than 50 entries be used. In order to combat this issue, and increase model accuracy per entry, both quadratic and cubic interpolation methods in EES were also evaluated. A qualification of the

relative accuracy of each method was obtained by plotting the temperature range of a binary mixture of R14 and R23 (at constant pressure) versus fluid enthalpy. First, a curve was produced using 250 points directly from Refprop. Then, using tables generated with 25 entries, an interpolation curve was overlaid onto the plot for each method calling the same 250 points. The mixture transition points were then analyzed to highlight any discrepancies. Figure 1-7(a) and (b) below show these areas in additional detail.

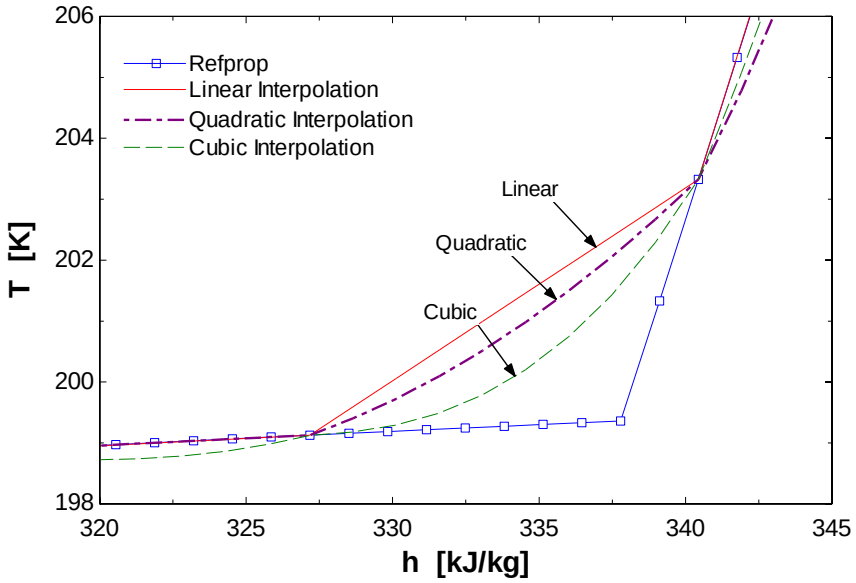

(a)

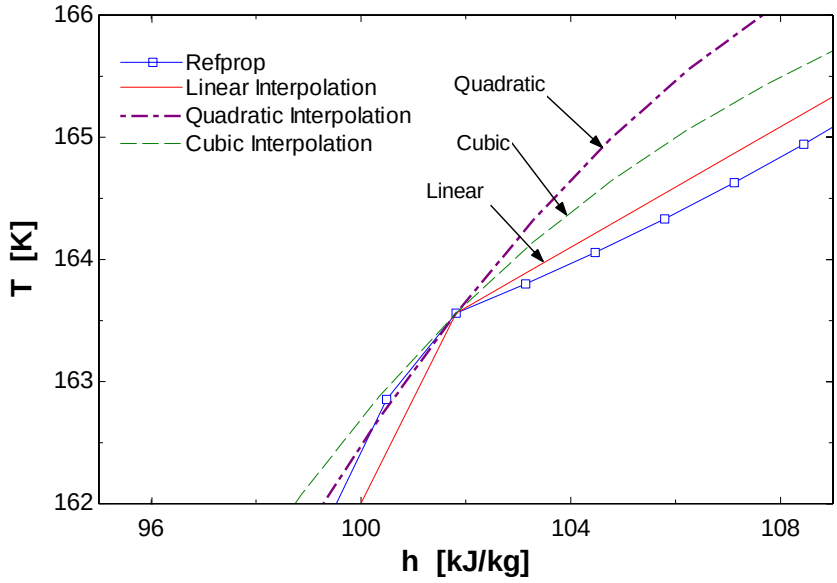

(b)

Figure 3-7: Qualitative interpolation method comparison for a nominal test point. (a) relative approximation of dew point location. (b) relative approximation of bubble point line.

As can be seen from Figure 1-7(a), the quadratic and cubic interpolation methods show minor improvement over the linear case at the liquid line. However, both methods deviate from the near linear trend displayed by Refprop on either side of the line in the superheated vapor and high quality two phase regions. A similar yet more apparent deviation is shown in Figure 1-7(b) in the low quality two phase region, where the linear trend actually displays the best fit. Although both higher order methods provide a slightly better approximation of the saturated liquid and vapor lines, as a result of the near linear trend within each flow region, linear interpolation is favored.

As will be shown in section 1.3, the mass quality in each section of the recuperator significantly affects the fluid conductance in the two phase regime. As a result of this, interpolation tables are also used to determine the mass quality of the mixture at each node of the heat exchanger. In order to verify the increase in model efficiency due to the inclusion of these tables, a study, similar to that performed in Table 1-1 was conducted to verify differences in model convergence time. These results are presented in Table 1-2 below.

Table 3-2: Comparison of model calculation time using Refprop and NIST4 both with and without the use of interpolation tables. Results for a nominal test condition using a mixture of R14+R23 with 50 interpolation table entries.

Database	Refprop (w/ tables)	Refprop (w/o tables)	NIST4 (w/ tables)	NIST4 (w/o tables)	Tables Pre-generated
Computation Time (s)	43.4	130.4	10.6	73.5	14.4

As can be seen from Table 1-2, for a nominal test case using a binary mixture of R14 and R23, the incorporation of temperature and quality interpolation tables results in almost a

67% decrease in computation time (when using Refprop). The most significant portion (>50%) of that time is spent generating the interpolation tables themselves.

Depending on the guess values used for a given model condition, and the interpolation method implemented, it is possible that the enthalpy for one or more heat exchanger nodes may exceed the range of the interpolation tables. Often the model will still converge onto the correct solution (as the interpolation method will extrapolate to data points outside the range); however, for this reason it is recommend that a margin of safety of approximately 5% of the total range be added to either end of the table.

3.3 Empirical Tuning of Thermodynamic Model

In order to increase the accuracy of the predictive model for the cryosurgical system, empirical models relating the fluid condition at different cycle states to the conductance, pressure drop, and mass flow rate are utilized. A brief overview on their formulation and implementation into the model is subsequently described. It is important to note that these correlations are primarily applicable to the experimental system under analysis. In order to effectively analyze another system, a procedure similar to that followed in the referenced texts would need to be performed and the correlations updated.

3.3.1 Conductance Correlations

In Section 1.2.3 a preliminary thermodynamic model is described that takes into account the variation in the working fluids heat transfer coefficient throughout the recuperator, iterating over the warm side temperature difference until a specified pinch point

temperature within the heat exchanger is obtained. As the temperature profile throughout the recuperative heat exchanger is dependent on the mixture and operating point being analyzed, it is logical to assume that the actual pinch point temperature difference will vary between test points. In an effort to make the predictive model more applicable to a range of operating conditions and mixture formulations (as well as more accurate), Skye (2011) formulated a correlation relating the recuperator conductance per unit length to experimental variables which directly impact fluid flow distribution and void fraction. Estimation of the heat transfer coefficient *a priori* for a multi-phase, multi-component fluid is not currently possible as no general correlations exist. As the same experimental system was utilized to develop the empirical correlation, the results presented by Skye (2011) are directly transferable to this case.

Figure 1-1 in Section 1.2.2 provides a schematic of the fully instrumented experimental system. Of particular interest are the diametrically opposed PRTs, evenly spaced along the length of the heat exchanger (shell/cold side). These allow for a finer resolution of the temperature profile throughout the recuperator. The process of determining the conductance for each section mirrors that described in Section 1.2.3 for the thermodynamic model. The section temperature is determined by averaging values from the PRTs on either side of the shell. All sections, 6 in total, are then further subdivided by the experimental model into N_{sub}=10 sub-sections each of which exchange an equal portion of energy. These measurements allow for a more accurate approximation of the conductance of each section in the two phase regime (the section conductance being equal to the sum of the conductances calculated for every sub-section in it).

The experimental data used to formulate the empirical correlation were collected over a large range of fluid thermodynamic quality using a binary mixture of R14 and R23 by varying the mixture composition, mass flow rate, and input load. The conductance of each section was then normalized by the length of finned tubing it encompassed, compiled as a single data point (5 data points for a single test as one section includes only unfinned tubing), and separated by flow regime for further analysis. Of particular interest is the two-phase conductance data, which are shown in Figures 1-8(a) and (b) below. It should be noted that data from one other recuperator section was omitted in the two phase regime due to the fact that it extends significantly beyond the finned tubing, encompassing the area between the precooler sheath and stainless steel shell.

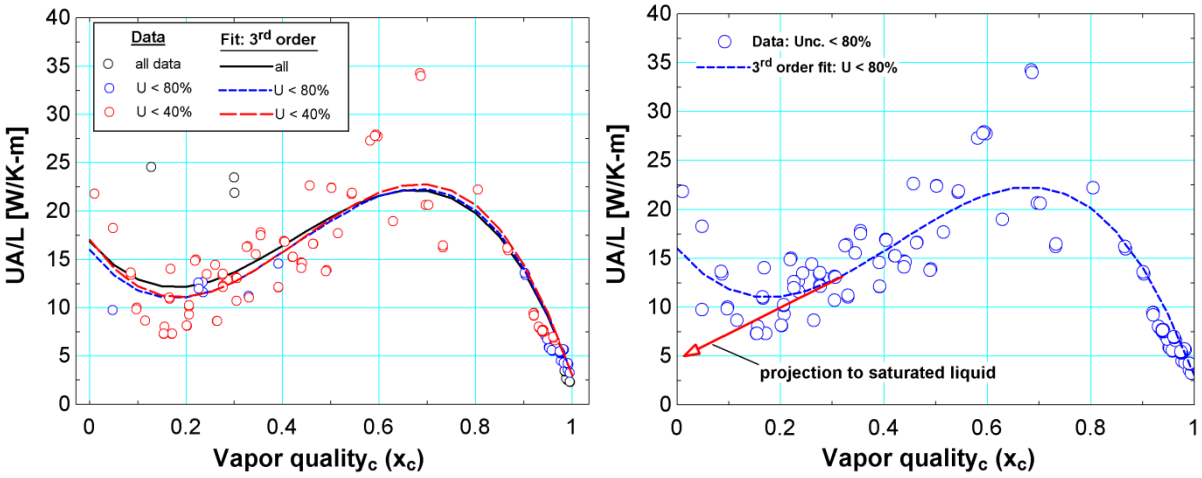

Figure 3-8: Recuperator conductance normalized by finned tube length as a function of cold stream vapor quality. (a) shows the variation in curve fit between the various uncertainty filters, and (b) shows the 80% data with a projection toward saturated liquid from a quality of about 0.3. (Skye 2011)

A 3rd order polynomial fit was applied with varying levels of uncertainty and the <80% uncertainty data retained to eliminate a few of the more significant outliers. It is

important to note the amount of scatter present in the data, specifically for values of quality below 0.8. Additionally, the fluid heat transfer coefficient in the liquid regime should not exceed that observed in the bulk of the two phase region. Thus the fit is forced to follow the roughly linear trend shown for vapor qualities between 0.3 and 0.5 in the correlation.

For the vapor regime, the conductance data was normalized by both finned tube length and cold stream thermal conductivity and plotted vs. the cold stream average Reynolds number. No additional collapse was observed with the latter normalization, however, nor was any significant variation observed over the range of cold stream Reynolds numbers examined. For this reason they are omitted from the final correlation.

A very small subset of data was collected in the liquid regime, thus a liquid conductance correlation was not explicitly developed but assumed nominally constant (as was exhibited by the vapor regime data) and equal to the conductance per unit (finned) tube length for 0 vapor quality in the two phase regime. Table 1-3 below summarizes the findings from all three flow regions.

Table 3-3: Recuperator conductance correlation over the entire range of cold stream quality (Skye 2011)

Quality Range	(UA_{rec}/L_{rec}) Correlation [W/K-m]
$x_c < 0$	5.238
$0 \leq x_c < 0.3$	$5.238 + 25.0x_c$
$0.3 \leq x_c \leq 1$	$15.99 - 62.49x_c + 224.6x_c^2 - 175.1x_c^3$
$x_c > 1$	2.99

Implementing the empirical correlation is relatively straightforward as the conductance of each section is already calculated by model. Since the fluid thermophysical condition is known throughout the recuperator, the mass quality can easily be computed for each node on the cold side of the heat exchanger (ideally using interpolation tables as discussed in section 1.2.5). Using the average quality between section nodes, a separate function was created in EES that computed the conductance per unit length (finned) tubing for each recuperator section based on the mass quality in that section. The total finned tube length can then be computed as shown:

$$L_{tube,f,rec} = \sum_{i=1}^{N_{rec}} \frac{UA_{rec,i}}{\frac{UA_{rec}}{L_{rec}}(x_{c,i})} \tag{3.17}$$

where N_{rec} is the number of sub-heat exchanger sections. $UA_{rec,i}$ can be calculated directly once the mass flow rate in the system is known. An empirical compressor map correlation that provides a relationship between the compressor suction and discharge pressures and the second stage cycle mass flow rate will be presented in Section 1.3.4.

The finned tube length calculated by the predictive model can be compared to the measured fin tube length within the recuperative heat exchanger and used to direct the iteration method as described in Section 1.4.2.

3.3.2 Recuperator Pressure Drop

The thermodynamic system model detailed in Section 1.2.3 doesn't take into account the pressure drop through either the recuperative or precooling heat exchangers in the mixed fluid cycle. As there is no means of measuring the pressure between the heat exchangers

experimentally, an approximation must be made. The original correlation formulated by Skye (2011) for this experimental system was predicated on the assumption that the pressure drop through the recuperator and precooler were about equal (reference Figure 1-1).

$$P_4 = \frac{P_3 + P_5}{2} \tag{3.18}$$

This assumption is justified by the fact that the largest pressure drop will occur in the warmer areas of both heat exchangers, where the density is low and fluid velocity is high. Although the mixture flow passage length through the precooler is only about 1/3 of the (finned) tube length contained within the recuperator, the fluid is much warmer throughout it. Experimental data, including those used to formulate the conductance correlation in Section 1.3.1, were compiled and compared to the general form of the single phase pressure drop equation, $\Delta P = f(Re, e, D)\rho v^2$, where f is the friction factor. All terms in this relation are computed at the warm end of the heat exchanger (state 4 for the hot side and state 1 for the cold side). The relative roughness, tube length and diameter are all constant between tests. Additionally the Reynold's number was not observed to vary significantly over the range of test points. Therefore, the correlation assumes the following form:

$$\Delta P = \frac{1}{2}\rho v^2 \tag{3.19}$$

The data and corresponding fit are shown in Figures 1-9(a) and (b) below.

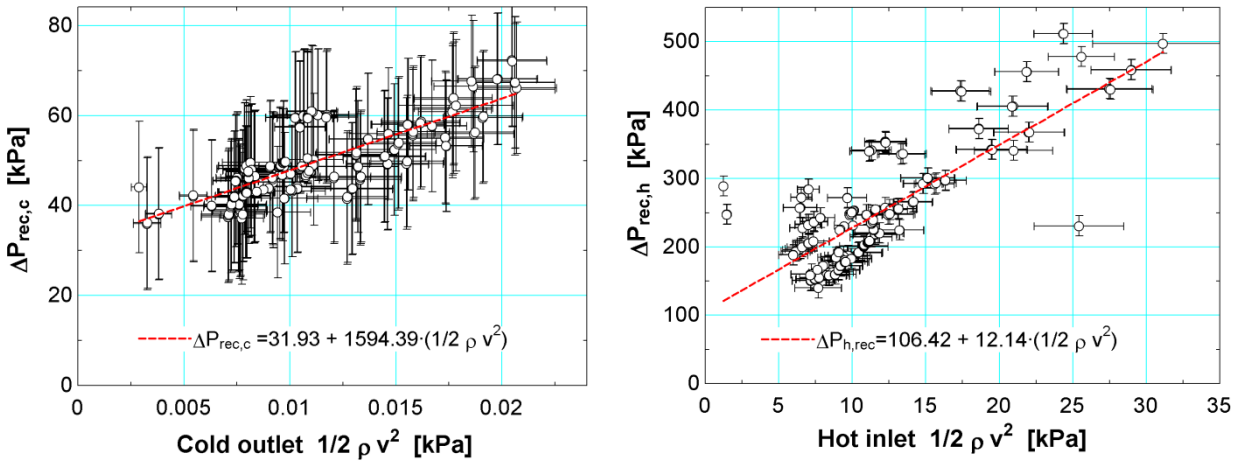

Figure 3-9: Recuperator pressure drop empirical correlations for the (a) cold, and (b) hot streams of the recuperator. (Skye 2011)

Both sets of data display a roughly linear trend as shown in Figure 1-9. The correlation is summarized along with curve fit statistics in Table 1-4.

Table 3-4: Recuperator pressure drop correlation coefficients and curve fit statistics. (Skye 2011)

Correlation Form	a_0 [kPa]	a_1 [-]	RMS error [kPa]	R^2	N_{points}
$\Delta P_{rec,c} = a_o + a_1(1/2\rho_{rec,c,out}v^2_{rec,c,out})$	31.93	1594.39	4.78	0.62	198
$\Delta P_{rec,h} = a_o + a_1(1/2\rho_{rec,h,in}v^2_{rec,h,in})$	106.42	12.14	50.0	0.61	198

Implementing this correlation is straightforward for the case where the predictive model iterates on the hot side temperature difference, $T_{rec,h,diff}$, as the condition of the fluid on the suction side of the compressor is fully defined at the beginning of each iteration. For reasons discussed in section 1.4.3, the computation scheme utilized by the predictive model

was modified such that the temperature difference on the cold end of the recuperator was varied as follows:

$$T_5 = T_7 + T_{rec,c,diff} \tag{3.20}$$

As a result of iterating over the cold side temperature difference, the equations governing the pressure drop through the recuperative heat exchanger must be solved implicitly. This process begins by inputting a guess value of pressure drop through the warm and cold sides of the recuperator (for the purpose of this description assume a pressure drop of 0 [kPa]). This fully defines all inlet/exit conditions. The pressure drop correlations may then be implemented and enthalpies at the cold (distal) end of the heat exchanger recalculated. There are a few different metrics that can be used to evaluate convergence with respect to pressure drop. The one implemented by this model is the recuperative heat transfer rate normalized by the mass flow rate, or the enthalpy difference on the cold side of the heat exchanger:

$$\frac{\dot{Q}_{rec}}{\dot{m}} = h_1 - h_7 \tag{3.21}$$

Using this metric provides similar accuracy to direct evaluation of the temperature on the suction side of the compressor (within 1%) but decreases computation time by just over 9% (for a nominal test case using a binary mixture of R14+R23).

Since the pressure drop over the hot side of the recuperative heat exchanger is governed entirely by the temperature and pressure of the gas mixture at state 4, the only complication added by the precooler is that the pressure at state 4 will also need to be iteratively solved; i.e. originally assume a pressure drop of 0 [kPa] to state 4 (compressor

discharge pressure), solve for the pressure drop over the recuperator and deduct that from the original (discharge) pressure, repeating until a solution is obtained.

3.3.3 Omitted Correlations and Recent Empirical Correlation Improvements

An empirical correlation, similar to that formulated for the recuperator, was also created for the precooling heat exchanger. This correlation was not implemented in the version of the model used for experimental mixture selection and preliminary system analysis, however, as the 2nd stage fluid temperature exiting the precooler is approximately the same regardless of mixture composition (H. M. Skye, 2011). Skye (2011) provides 3 major assumptions that justify the near constant temperature condition at state 4:

1. The pure synthetic refrigerant (R410A) contained within the precooling vapor compression cycle will be saturated and thus will remain at relatively constant temperature given the pressure drop through the heat exchanger is small.
2. The thermal resistance of the mixed gas working fluid will dominate throughout the precooling heat exchanger (as a result of 1).
3. The gas mixture is generally superheated throughout the precooler.

It has been shown by Nellis et al. (2005), for vapor phase testing of mixtures in microtubes, that the heat transfer coefficients were well predicted by correlations for single phase – turbulent flow and found to be generally insensitive to small changes in composition. The main error associated with omission of this correlation will be related to changes in mass flow rate of the 2nd stage mixture through the precooler for a given

experimental test point. The impact on model accuracy will be more thoroughly evaluated and quantified in the data analysis and results review sections of this document.

Excellent agreement between the predictive empirical model and experimental data was observed using the Skye (2011) correlations for input loads <15W. For better performing mixtures (loads >15W), the empirical model generally under-predicted cycle performance, largely as a result of an overly conservative estimate of precooler effectiveness. In an effort to improve model accuracy, Passow (2012) incorporated a more physics based approximation of the pressure drop through the precooling and recuperative heat exchangers based on the Müller-Steinhagen and Heck two phase pressure drop correlation (simplifies to the appropriate single phase pressure drop correlation for single phase flow). Implementing these correlations in the predictive model increased computation time by more than a factor of 10. Thus they were instead used to reprocess the original experimental data presented by Skye (2011). Each of the correlations was then updated (except for the cold side recuperative pressure drop as states 7 and 1 which are measured experimentally) and new predictive model results compared to the original, Skye (2011), formulation. This comparison is presented in Figure 1-10 below for reference.

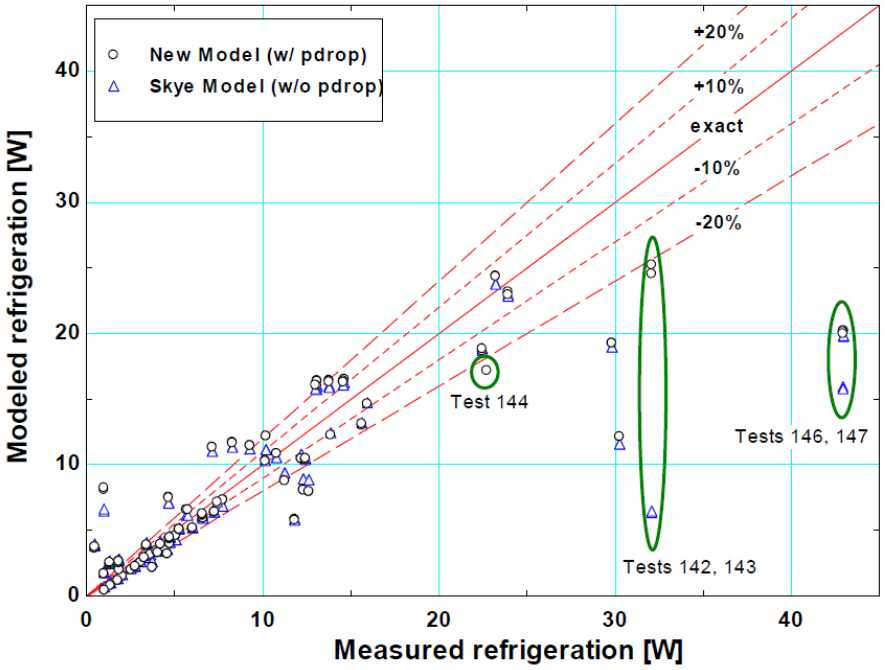

Figure 3-10: Measured refrigeration power compared to refrigeration predicted using the empirically tuned model comparing the results to the original, Skye (2011), model formulation. (Passow 2012)

As can be seen from the data, for low values of refrigeration power (<15W), there is negligible improvement over the original model, with error for tests using pure refrigerants and three-component mixtures of about 20%. Significantly improved agreement is exhibited for some of the better performing mixtures, of which the largest differences are highlighted in the figure.

The test input load for the experiments conducted in this research was below 5W and was selected partially based on minimizing measurement uncertainty at each test point. A more detailed presentation of experimental mixture and operating point selection will be provided as part of a future update. As a result of this, the current predictive model doesn't implement any updates to the pressure drop or conductance correlations beyond those created by Skye (2011).

3.3.4 Compressor Map/Volumetric Efficiency Model

In addition to the empirical model updates presented in section 1.3.3, Passow (2012) utilized a volumetric efficiency model to map the performance of the 2nd stage compressor (Danfoss model TFS4.5CLX). The result was a direct relation between the pressure ratio across the compressor and the mass flow rate through the system (whereas the first generation model required these as separate inputs). The general form of the semi-empirical model used is presented below (Popovic & Shapiro, 1995). The polytropic exponent *n* from the original correlation is replaced by the isentropic exponent *k*, which changes with mixture composition:

$$\eta_{vol} = \frac{\dot{V}_{suction}}{\dot{V}_{disp}} = 1 + C - C\left(\frac{P_{discharge}}{P_{suction}}\right)^{\frac{1}{k}} \tag{3.22}$$

where η_{vol} - volumetric efficiency
C - clearance volume ratio
k - isentropic exponent
$\dot{V}_{suction}$ - suction volumetric flow rate
$\dot{V}_{disp}$ - displacement rate

The suction and discharge pressures are measured directly by P1a and P3, respectively (refer to Figure 1-1). Eq. 1.1 neglects pressure drop through the compressor valves and includes the pressure drop through the flexible tubing between the compressor and P3 as measurement uncertainty. The suction side volumetric flow rate is used to calculate the mass flow rate for the mixed gas cycle as follows:

$$\dot{V}_{suction} = \dot{m} / \rho(T_{suction}, P_{suction}) \tag{3.23}$$

$T_{suction}$ is well approximated as being at room temperature as the fluid must pass through a long length of connective tubing, external to the dewar, before reaching the compressor inlet (additionally a Variac heater is utilized along a short length of tubing to eliminate the risk of fluid cavitation within the compressor). The polytropic exponent is also calculated using suction side properties as show below:

$$k = \frac{c_p\left(T_{suction}, P_{suction}\right)}{c_v\left(T_{suction}, P_{suction}\right)} \tag{3.24}$$

Passow (2012) evaluated three different methods in order to experimentally determine the volumetric displacement rate $\dot{V}_{disp}$ and clearance volume ratio *C*. All three methods utilized data from test runs with nitrogen and R23, due to the large difference in fluid physical properties. Ultimately, a two degree optimization was used to minimize the error between the calculated and measured volumetric efficiency (evaluated by iterating over the value of both unknowns). The volumetric displacement rate used in the error equation was the suction volumetric flow rate averaged from a series of short circuit experimental compressor tests, conducted by fully opening the bypass valve in the mixed gas cycle. With the bypass valve fully open, the suction and displacement volumetric flow rates, according to the above volumetric efficiency correlation, must be equal. Table 1-5 summarizes the results of the optimization:

Table 3-5: Compressor correlation data with corresponding RMS error values. (adapted from Passow 2012)

C [-]	$\dot{V}_{disp}$ [m^3/s]	E_{RMS} Nitrogen	E_{RMS} R23	E_{RMS} all data
0.03655	0.0001693	0.025	0.013	0.025

Implementing the compressor map into the predictive model is straightforward as the compressor suction and discharge pressures were inputs to the thermodynamic model described in section 1.2.3.

3.3.5 Charge Pressure and Orifice Diameter

It is generally desired by designers of cryosurgical systems to tune cycle operating parameters in order to yield a cryoprobe with optimal cooling capacity for a given heat exchanger size. The model detailed in section 1.2.3, combined with correlations discussed to this point, allows for cryoprobe optimization by modifying the following inputs: compressor suction and discharge pressures, load temperature, and recuperator hot side inlet temperature. In particular, assignment of the compressor suction and discharge pressures may not be straightforward or easily estimated without experimental data. Experimental components affecting cycle pressure ratio include the system static charge pressure and orifice diameter. Thus a physical relationship between these parameters and compressor suction and discharge pressures is required.

The working fluid for the second stage cycle analyzed in this research is a binary mixture of R14 and R23. Both pure substances (and thus any mixture blend of the two) are in the superheated vapor phase at ambient conditions (25 C and 1 atm) and thus will exhibit ideal gas behavior:

$$m = \frac{PV}{R_{specific}T} \tag{3.25}$$

As this is a closed system, the mass contained within the system under static conditions must necessarily be equal to the mass contained within the system at a given test

point (the high pressure and low pressure sides of the system), i.e. $m_C=m_H+m_L$, where the subscripts C, H, and L indicate charge, high, and low respectively. Substituting the ideal gas relation above and assuming constant temperature between the charge and operating conditions we get:

$$P_C V_H + P_C V_L = P_H V_H + P_L V_L \tag{3.26}$$

This relation assumes that the mass of refrigerant in the coldest portion of the system, which could be in the liquid phase, is negligibly small. Dividing Eq. 1.22 by the low side system volume yields:

$$P_C \frac{V_H}{V_L} + P_C = P_H \frac{V_H}{V_L} + P_L \tag{3.27}$$

Experimental data can then be utilized in order to evaluate the ratio of the high to low side cycle volumes. As more experimental data are collected this ratio will be compared to the charge pressure to verify the amount of scatter in the data as well as to ensure no trend exists. The mixture utilized for these data points will be the same as described in the mixture selection section of the next report (a binary mixture of R14 and R23).

In order to determine the correct orifice size for a given set of high and low side system operating pressures, an appropriate fluid expansion model must be incorporated. Two such models were evaluated for this system. The first is a simplification of Bernoulli's equation for steady and inviscid flow. Assuming negligible gravitational effects and that the fluid is incompressible this equation reduces to:

$$P_1 - P_0 = \frac{1}{2}\rho(v_0^2 - v_1^2) \tag{3.28}$$

where subscripts 1 and 0 indicate the upstream and orifice fluid conditions, respectively. The density term is evaluated immediately downstream of the contraction where the temperature is reduced due to the JT effect across the orifice, $\rho(T_{downstream}, P_{downstream})$. The experimental instrumentation utilized to evaluate each term is detailed in Table 1-6 below.

Table 3-6: List of orifice model measurement instrumentation, location and uncertainty.

Variable Name	Sensor Name (Figure 3-1)	Sensor Location	Measurement Uncertainty
P_1	P5	Immediately upstream of orifice	±3.0 psi
P_0, $P_{downstream}$	P7	Downstream of orifice after nichrome wire heater	±1.5 psi
$T_{downstream}$	PRT 6	Immediately downstream of orifice	±0.5 [K]

The simplified form of Bernoulli's equation can be further reduced by evaluating the relative magnitude of the velocity terms. As the fluid moves from an area of high pressure (upstream of orifice) through a very small contraction, the pressure will decrease and the fluid velocity will greatly increase. The diameter of the orifice for the experimental system may be less than 1% of the tube diameter leading into it; thus the velocity of the fluid upstream of the orifice is neglected yielding the final model form:

$$P_1 - P_0 = \frac{1}{2}\rho v_0^2 \tag{3.29}$$

As the mixed refrigerant mass flow rate is known from the correlation detailed in the proceeding section, this equation can be used to calculate the orifice diameter directly.

$$\dot{m} = \rho A_0 v_0 \tag{3.30}$$

Substituting the orifice diameter in for A_0 and rearranging:

$$d_{orifice} = \sqrt{\frac{4\dot{m}}{\pi \rho v_0}} \tag{3.31}$$

The second method used to evaluate the orifice diameter assumes isentropic flow across the contraction and follows directly from the derivation shown in section 16.3 of Klein and Nellis (2012). The isentropic model is an improvement over the Bernoulli approximation in that it accounts for fluid compressibility through the expansion device. The velocity in the area of the contraction is calculated by taking an energy balance between the fluid just upstream of the orifice and within the vena contracta region immediately beyond it (in order to get the correct fluid pressure at the location of the contraction). As we do not measure the pressure until after the nichrome wire heater, it is assumed that the pressure drop between the area just after the contraction and the pressure sensor is negligible. The simplified energy balance is presented below, again neglecting gravitational effects and assuming the velocity contribution upstream of the device is negligible (as in the Bernoulli derivation):

$$h_1(T_{upstream}, P_{upstream}) = h_0(P_{downstream}, s_1) + \frac{v_0^2}{2} \tag{3.32}$$

Note that s_1 is calculated in the same manner as h_1. Using experimental data from tests with a binary mixture of R14+R23 compiled from Skye (2011), the accuracy of each method was evaluated. Each test utilized a constant orifice diameter of 0.0175in. The average diameter error from 48 data points with varying composition and upstream/downstream fluid conditions is shown in Table 1-7.

Table 3-7: Comparison of two different orifice modeling techniques in terms of % error deviation from the actual (known) value.

Method	Average Error (%)	Maximum Error (%)
Bernoulli Model	10.24	40.97
Isentropic Model	12.88	36.39

As can be seen from the data in Table 1-7, both models are within about 15% (on average) of the actual orifice diameter. Due to the lower average error associated with the Bernoulli method, it is the one currently employed within the predictive model. However, work to improve the isentropic orifice diameter approximation is ongoing and includes the incorporation of a discharge coefficient and a condition that determines the orifice diameter based upon choked flow conditions.

All states required by both the charge pressure and Bernoulli models are completely defined at the end of each predictive model iteration ($T_{rec,c,diff}$ or $T_{rec,h,diff}$). Therefore, both may be directly added to the final lines of the main function/procedure. It is worth noting that, if formulated in the manner described in subsequent sections, the charge pressure and orifice diameter can still only be viewed as outputs to the predictive model (we are able to enter them as inputs only as a result of the implicit equations solving technique used by EES). Further discussion regarding this will be provided in the subsequent section.

4 Solution Methodology

4.1 Overview

The predictive model formulation outlined in Chapter 3 progresses logically through a series of calculations based on the temperature difference between the two fluid streams at one end of the recuperator. As presented, the model requires specification of the following three inputs: 1) the compressor suction and discharge pressures ($P_{suction}$/$P_{low,2nd}$ and $P_{discharge}$/$P_{high,2nd}$, respectively), 2) the mixture composition ($\bar{y}_{2nd}$), and 3) the temperature at the tip of the cryoprobe (T_7). The most basic implementation of the model determines the sensitivity of the primary figure of merit, the cooling capacity, to these three independent parameters (ideally covering all input variables that govern the performance of a cryoprobe of a given compressor and heat exchanger size). However, the iteration method is implicit to the calculations detailed in chapter three. Its formulation is discussed in this chapter along with details on the general organization of the model.

4.1.1 Language Selection and Model Setup

The original model formulation took advantage of the algebraic equation solver native to EES. Additional features including unit checking and thermodynamic property data for pure fluids greatly simplified debugging and hastened the modeling process. Although these features, combined with the canned optimization routines, make EES an attractive option for the thermodynamic cryoprobe model; the solution methodology detailed in this section could be easily migrated to an assignment style programming language.

Regardless of the software or programming language used, in order to evaluate thermodynamic and transport properties for mixed refrigerants, an external call to the RefProp (Lemmon et al., 2013) or NIST4 (Ely & Huber, 1992) database is required. In order to facilitate the use of either database within EES, an interface program must be used. The RefProp interface program is aptly named EES_REFPROP (Klein, 2012b) and the NIST4 program EESNIST4 (Klein, 2012a). The mixture composition and two internal intensive properties need to be provided to either database to fully define the thermodynamic condition of the fluid in the 2nd stage cycle (this includes temperature and pressure in the vapor dome as a result of the temperature glide exhibited by mixtures). Both interface programs require specific units of measure for all input and output parameters. Thus, in an effort to avoid repeated unit conversions and simplify programming, all RefProp and NIST4 database calls are made within separate functions in the main equations window. These functions are sorted by the thermodynamic property of interest.

4.1.2 Suggested Organization

For the reasons described in section 4.2, the final revision of the predictive model separates the numerical heat exchanger and pressure drop calculations into procedures that are callable from the main equations window. All input variable information and convergence criteria are defined outside of these procedures. Logic control statements allow the user to restrict the scope of the analysis to certain output variables or analyze the experimental data independently from the predictive model. Additionally, code nested in the main equations window allows the user to optionally store data at the end of an analysis to a .txt file for further review.

A basic analysis, with the inputs as specified in section 4.1 (cryoprobe tip temperature, compressor suction and discharge pressure, and mixture composition), calls a procedure that controls iteration of the approach temperature on the warm or cold end of the heat exchanger, $T_{rec,h,diff}$ or $T_{rec,c,diff}$, respectively. Based on the input parameters fed to this procedure, 1D or 2D interpolation tables can be constructed (the latter only if pressure drop is included). The procedure containing the thermodynamic heat exchanger and component level modes (presented in Chapter 3) is then recursively called until a condition representative of the actual heat exchanger geometry, to within an acceptable error tolerance, is obtained. The subsequent section justifies the use of a separate iteration procedure as well as its formulation.

4.2 Root Finding Algorithm (Load Temperature Input)

In order to evaluate convergence using the native iterative solver in EES, the finned tube length calculated by the predictive model, $L_{rec,f}$, was compared directly to the known (measured) finned tube length on the hot side of the recuperator, $L_{f,actual}$ (=1.171m):

$$Residual = \sqrt{(L_{rec,f} - L_{f,actual})^2} \tag{4.1}$$

where the residual was set equal to 0 m^2. Given an appropriate set of guess values for the enthalpy at all seven states for the mixed gas cycle (see Figure 3-1) EES is able to numerically solve the coupled system of equations for a steady state operating condition. Determination of these guess values may not be trivial and varies to some degree along with each of the input parameters. By reformulating the thermodynamic model within a procedure, the iteration process can be forcibly guided by changes in $T_{rec,h,diff}$ or $T_{rec,c,diff}$ only. In

addition, solution progress can be tracked and optimized. As an understanding of the relationship between the predicted finned tubing length and the hot or cold side recuperator temperature difference is required to guide iteration, model issues can be more easily recognized and corrected.

4.2.1 Iteration Procedure

The original model was guided by changes to the temperature difference between fluid streams on the warm end of the recuperator, $T_{rec,h,diff}$. Using this metric (as opposed to the cold end recuperator approach temperature) simplified the calculation of the pressure drop on the shell (cold) side of the heat exchanger as described in section 3.3.2. In order to determine its effects on the finned tube length output by the predictive model, $T_{rec,h,diff}$ was varied between the bounds specified in equation (4.2) below. The results of this analysis are plotted for two different mixture blends in Figure 4-1. Note that an almost identical relationship can be observed between the finned tube length and temperature difference at the cold end of the heat exchanger.

$$0\,[K] < T_{rec,h,diff} < (T_4 - T_7) \tag{4.2}$$

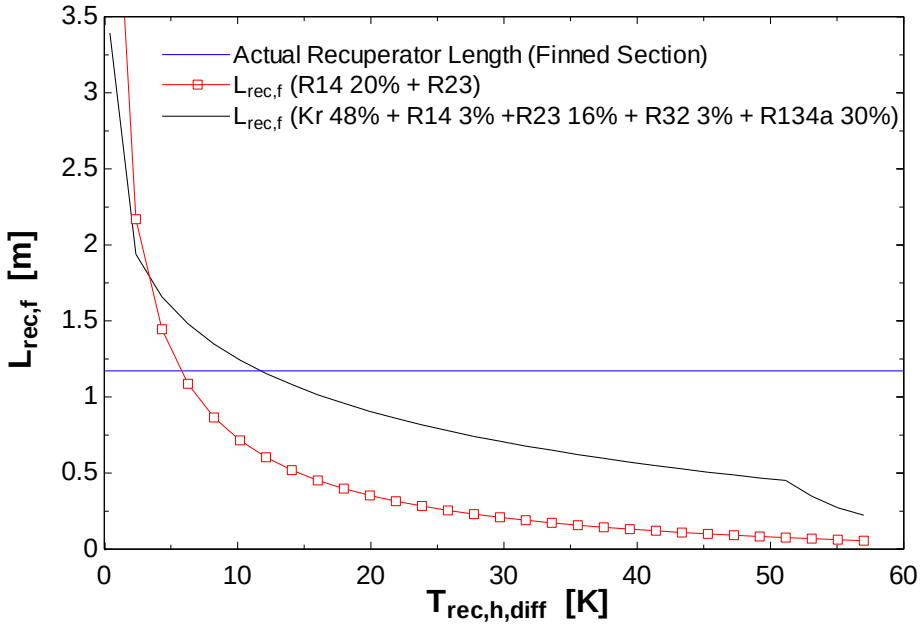

Figure 4-1: Recuperator finned tube length as a function of the temperature difference between the two fluid streams at the warm end of the recuperator (no pressure drop. The actual finned tube section length is indicated by the blue line.

As shown in Figure 4-1, as the temperature difference at the warm end of the recuperator decreases the effectiveness increases. The increased effectiveness results in an increase in the finned tube length predicted by the empirical model. As the effectiveness approaches unity, the conductance correlation accurately predicts a dramatic increase (towards infinity) in the size of the required heat exchanger. The opposite effect is observed with higher values of $T_{rec,h,diff}$, i.e., as the temperature difference increases, the required length of the finned tube is reduced. The exact shape of this function varies with the composition of the 2nd stage refrigerant as well as the operating point analyzed. Nonetheless a simple iterative solution procedure can be constructed based on the form of the solution shown.

During the course of this analysis, it was determined that very low values of the warm end heat exchanger approach temperature result in a condition where the enthalpy at state 5

(from Figure 3-1) was outside of the thermodynamic database bounds (of both Refprop and NIST4). The lower bound on cycle enthalpy can be approximated using the lowest cycle operating temperature and compressor discharge pressure.

$$h_{min} = h(P_{high,2nd}, T_4, \bar{y}_{2nd}) \tag{4.3}$$

The minimum allowable warm side temperature difference may then be computed by substituting the lower bound on cycle enthalpy for h_5 and back solving for the enthalpy at state 1 using equations 1.9 and 1.10 from chapter 3. This process limits the (highest) temperature at state 1 and thus $T_{rec,h,diff}$. This complexity can be avoided altogether by iterating over the cold end approach temperature, $T_{rec,c,diff}$, which directly bounds state 5 to be between the temperature at the load location and the temperature of the mixed gas exiting the precooling heat exchanger. The latter method was ultimately selected in revision of the predictive model. However, the majority of failure modes that will be discussed subsequently and in section 4.3 still apply when the warm end temperature difference is used.

A single failure mode is apparent from Figure 4-1, namely that the value of sub-heat exchanger effectiveness can become greater than unity as $T_{rec,c,diff}$ approaches 0K (corresponding to a pinch point condition at the cold end of the recuperator). This condition (reference issue number one in Table 4-3) prohibits the calculation of the number of transfer units (NTU) inside of the thermodynamic model and thus must be captured prior to the use of the effectiveness-NTU relations. If this condition is encountered, an arbitrary value of the finned tube recuperator length, outside of the solution bounds, can be specified to correct the subsequent guess value.

The iterative solution process begins by assuming the temperature at state 5, which is limited by the temperature at the load location (T_7) and the temperature of the mixed gas exiting the precooler (T_5), is halfway between the two. This value is then modified depending on the finned tube length returned by the thermodynamic model until a physical solution is obtained; i.e. the guess value of $T_{rec,c,diff}$ allows for the use of the effectiveness-NTU relations in the procedure containing the thermodynamic model. The iterative solver accomplishes this task by adjusting the upper or lower limit on $T_{rec,c,diff}$ depending on the failure condition encountered (the value returned by $L_{rec,f}$) and bisecting the two for the subsequent iteration. If, for example, the value of $L_{rec,f}$ returned by the thermodynamic model is too large, the iteration procedure resets the lower limit on $T_{rec,c,diff}$. It then bisects towards the upper limit as shown in equation (4.5).

$$limit_{lower} = T_{rec,c,diff}[i] \tag{4.4}$$

$$T_{rec,c,diff}[i+1] = T_{rec,c,diff}[i] + 0.5(limit_{upper} - limit_{lower}) \tag{4.5}$$

Bounds on the calculated finned tube recuperator length are also tracked which simplifies model debugging as issues arise.

Once a physical solution is obtained, the previous guess value of $T_{rec,c,diff}$ is incremented by a fixed ΔT. The value of this fixed temperature increment is set as a parameter in the main equations window. Depending on the magnitude of the temperature increment used, the routine will extrapolate linearly or use linear interpolation to estimate the

actual value of $T_{rec,c,diff}$. The following example illustrates this methodology for a binary mixture of R14 and R23 with inputs as specified in Table 4-1.

Table 4-1: Input parameters to illustrate solution methodology. Mixture constituents are R14 and R23.

Input Parameter (reference Figure 3-1)	Value
$\bar{y}_{2nd}$	.67
$P_{low,2nd} = P_{suction}$	7.1 [psig]
$P_{high,2nd} = P_{discharge}$	178.5 [psig]
$T_7 = T_{load}$	222.2 [K]
T_4	246.1 [K]
P_{amb}	743.9 [mmHg]
T_{amb}	298.2 [K]

Initially, a guess value of the recuperator cold end approach temperature is made:

$$T_{rec,c,diff}[1] = \frac{(T_4 - T_7)}{2} = 11.9\,[K] \tag{4.6}$$

The upper and lower bound on the cold end approach temperature are also initialized, based on the solution bounds shown in equation (4.2).

$$limit_{lower}[1] = 0\,[K] \tag{4.7}$$

$$limit_{upper}[1] = (T_4 - T_7) = 23.9\,[K] \tag{4.8}$$

Using the thermodynamic model, the corresponding finned tube heat exchanger length is calculated. This is highlighted by point 1 on Figure 4-2, which details the functional

relationship between the cold end approach temperature and $L_{rec,f}$ for this example. A step of 1K is taken in the direction of the lower bound (point 2), and a two point linear curve fit applied as shown by the dashed line. The subsequent guess value for the cold end approach temperature can be determined from this curve fit. For this example, $T_{rec,c,diff}[2] = -31.4\ K$. Using this guess value in the thermodynamic model will result in an error as the cold side outlet temperature, T_5, is lower than the cryoprobe tip temperature, T_7 (a second law violation). In order to correct this issue, the current model revision will bisect the physical solution and the initial lower bound on the cold end approach temperature (given by equation (4.7)) until the following condition is satisfied:

$$L_{rec,f} \geq L_{rec,f,actual} \tag{4.9}$$

After each iteration, the upper limit on $T_{rec,c,diff}$ is reset. The results from the lower limit bisection for this example are presented in Table 4-2

Table 4-2: A portion of the iteration table detailing the lower limit bisection process.

Iteration	$T_{rec,c,diff}$ [K]	$L_{rec,f}$ [m]	$limit_{upper}$ [K]	$limit_{lower}$ [K]
1	11.93	0.1199	23.86	0
2	5.966	0.3854	23.86	11.93
3	2.983	0.9162	23.86	5.966
4	1.491	1.977	23.86	2.893

Linear interpolation is then used recursively between the lower and upper limits on the cold end approach temperature until the convergence criteria is met. In this example, the two

points used for the initial interpolation are specified in rows three and four of Table 4-2. The corresponding two point curve fit is depicted by the 'two point interpolation' line in Figure 4-2. A better initial guess value or modified step size would eliminate the need for linear interpolation. Alternatively, a higher order curve fitting technique would be well suited for this problem and is included as part of the recommended future work.

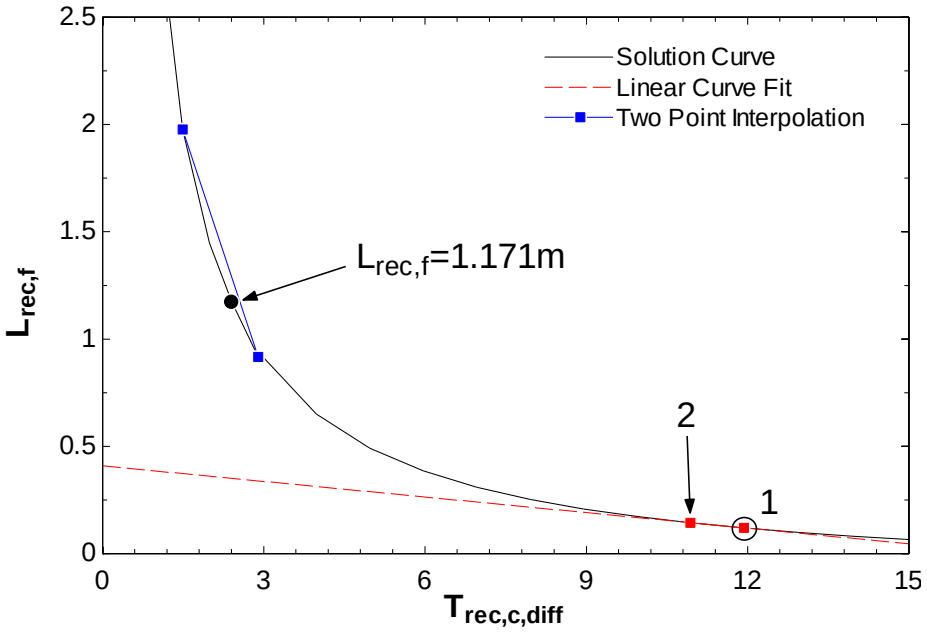

Figure 4-2: Finned tube recuperator length as a function of cold end approach temperature for a binary mixture of R14 (67%) and R23.

4.2.2 Computation of Load Temperature from Input Load

The iterative solution procedure outlined in section 4.2.1 allows for the determination of the cold or warm end recuperator approach temperature for a given value of T_7. Experimentally, the temperature at state 7 (at the load location) can be controlled by carefully varying the applied load from the Nichrome wire heater until thermodynamic equilibrium is achieved. This temperature could be most easily controlled by utilizing the PID control loop

mechanism on the Lakeshore 332 unit powering the heater. However, in an effort to reduce the time required for data collection, the input load for all experimental data was set directly within the LabView interface and the corresponding steady state tip temperature was recorded. Since the refrigeration load is set as an input to the experimental test facility, it seems logical to allow its use as an input in the predictive model. In pursuit of this objective, a second iterative procedure was formulated which varies the load temperature until the desired refrigeration load, $\dot{Q}_{load}$ is achieved. In order to ensure a robust solution procedure, an investigation similar to that presented in section 4.2.1 was conducted, with load curves generated for two different experimental data points. The results of this analysis are shown in Figure 4-3. The curves are identified by the actual load temperature measured experimentally (at steady state), with a given applied heat load from the nichrome wire heater. Results are shown both with and without the empirical pressure drop correlations in the predictive model. The actual heat load applied to the tip of the cryoprobe for both points is also detailed.

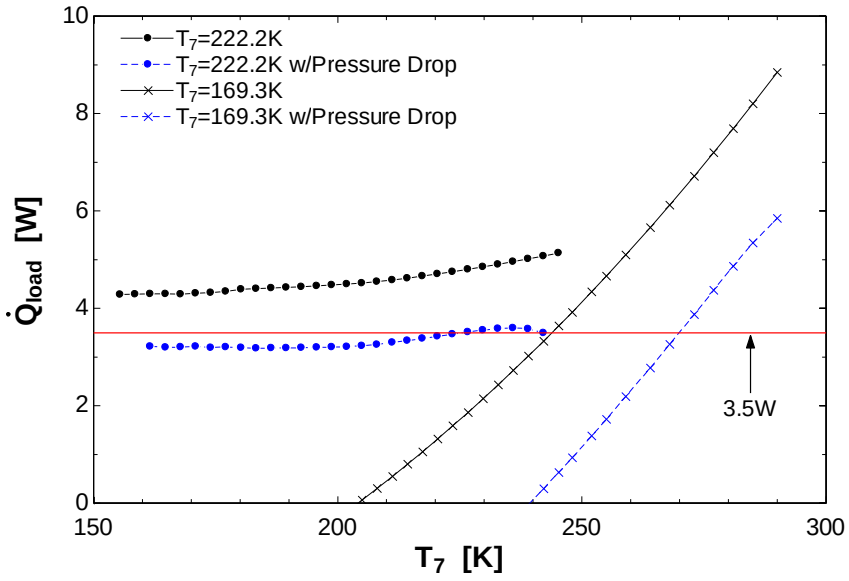

Figure 4-3: Cooling load as a function of cryoprobe tip temperature for two different experimental data points. For both points, a binary mixture of R14 and R23 was used.

Neglecting pressure drop through the precooling and recuperative heat exchangers, the results closely match the general form of curves presented by Fredrickson et al. (2006) for synthetic refrigerant mixtures. The addition of the empirical pressure drop correlation shifts each curve to lower values of cooling load for a given tip temperature. For the T_7=222.2 K curves, deviation from previously observed trends can be seen when the empirical pressure drop correlations are used. Specifically, a decrease in cooling load with increasing load temperature is observed for values of T_7 that are near the upper and lower solution bounds. This incorrect trend can be directly attributed to numerical error in the heat exchanger model, but is considered in formulation of the algorithm. Initially, a guess value of the cryoprobe tip temperature is made. As none of the experimental data points had a tip temperature less than 160 K, T_7 is assumed to lie between the temperature at state 4 and 160 K, values also used as initial bounds.

$$160\ K < T_7 < T_4 \tag{4.10}$$

The corresponding refrigeration load output guides the subsequent iteration, with the iterative solver resetting the upper bound on load temperature if $\dot{Q}_{load}$ is too large and the lower bound if $\dot{Q}_{load}$ is too small. The solver then bisects the upper and lower bound towards a solution. If the cooling load is observed to trend incorrectly, a warning message is generated and calculations cease. A similar result occurs if either the upper or lower bound remain at their initial values and bisection yields a change in temperature of less than 1 K. As iteration progress is tracked within lookup/array tables, the user can determine if a correction can be made and the solver improved.

4.3 Failure Modes

A significant amount of time was spent debugging and correcting issues with predictive model convergence. These were most often related to flaws in the iterative solution procedure or errors generated within the thermodynamic model. In an effort to increase the efficiency of future modeling endeavors, several key failure modes will be reviewed in this chapter and the resulting (recommended) model modifications discussed. First, basic thermodynamic model improvements will be presented. These will be followed with a review of some of the more complex failure modes, resulting from inclusion of the empirical pressure drop correlations.

4.3.1 Without Pressure Drop

As detailed in section 4.2.1, thermodynamic model failures result from the use of the effectiveness-NTU relationships with unbounded values of recuperator sub-section effectiveness. A condition yielding an effectiveness greater than one has previously been

discussed. Although a simple catch can also be inserted into the thermodynamic model to prevent the calculation of the number of transfer units in the event that the effectiveness is less than zero, an understanding of the underlying causes is needed to direct iteration. Figure 4-4 details such a condition (reference issue number two in Table 4-3). Since the mixed gas generally crosses the dew point line at lower values of temperature on the shell (cold) side of the recuperator, it has a smaller capacitance rate as compared to fluid on the hot side. Combined with the low approach temperature guess value, the calculated recuperative load will force the temperature of the fluid exiting the cold side of the heat exchanger to be higher than the temperature of the fluid at state 4. An effectiveness less than zero condition can also be obtained if no upper bound is enforced on the cold end approach temperature, thereby allowing the hot side exit temperature to be greater than at state 4 (reference issue number three in Table 4-3). In order to account for these situations in the thermodynamic model, the returned fin tube length (that ultimately determines what action should be taken by the iterative solver) is made a function of $\dot{Q}_{rec}$ in addition to the sub-heat exchanger effectiveness. Note that in this case the error must be captured as part of the effectiveness condition. Since both the enthalpy and temperature trend incorrect, the hot and cold side recuperator capacitance rates will remain positive.

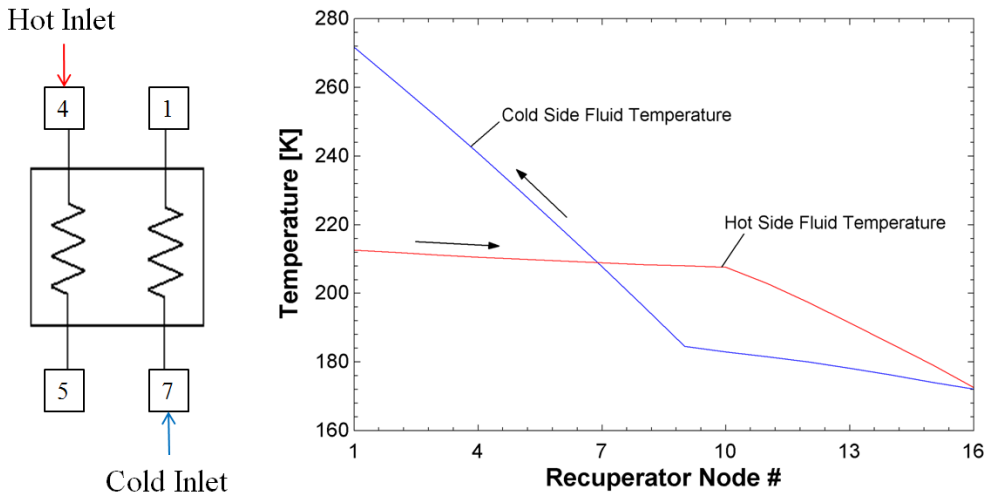

Figure 4-4: Recuperator temperature profile for a binary mixture of R14 and R23 for the case of a low cold end approach temperature guess.

4.3.2 With Pressure Drop

Incorporation of the empirical pressure drop correlation into the thermodynamic model provides an additional degree of freedom to the enthalpy distribution on both the hot and cold sides of the recuperator. There are two specific cases that warrant further discussion, both of which result from the cold end approach temperature being too high. The first and most obvious is depicted by the solid arrow in Figure 4-5, which is overlaid on a pressure vs. enthalpy property chart for a binary mixture of R14 and R23 (reference issue number four in Table 4-3). The issue occurs when the cold end approach temperature nears the upper bound established in equation (4.2). As a result of the almost isothermal pressure drop through the hot side of the recuperator, the enthalpy will actually increase between states 4 and 5. A simple energy balance over the hot side fluid stream will result in a negative refrigeration load for the recuperator. Depending on the operating point analyzed, this situation may be realized at even moderate values of the cold end approach temperature (the pressure drop on

the hot side of the recuperator can be significant as it is inversely proportional to the warm inlet fluid density).

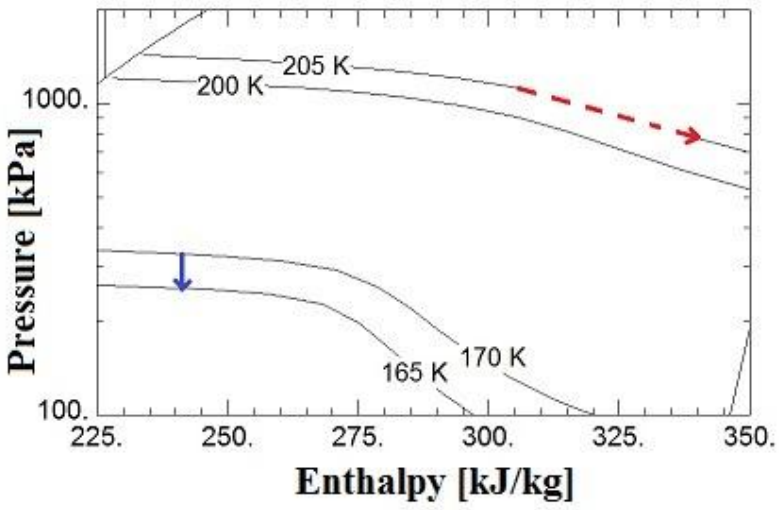

Figure 4-5: Pressure as function of enthalpy for a binary mixture of R14 and R23. The dashed arrow details isothermal pressure drop on the hot side of the recuperator. The solid arrow shows isenthalpic pressure drop, which can lead to a negative cold side capacitance rate.

A second failure mode is obtained as the cold end approach temperature is decreased from the proceeding condition (reference issue number five in Table 4-3). If the reduction in temperature is small, the heat exchanged between each sub-heat exchanger section will also be small. This situation results in an almost isenthalpic pressure drop over the shell (cold) side of the recuperator, forcing the temperature to decrease, as shown by the dashed arrow in Figure 4-5. Since the temperature trends incorrectly, the cold side capacitance rate will be negative in at least one heat exchanger sub-section, as shown in Figure 4-6. Care should be taken in imposing a condition on the cold side capacitance rate, however. If the predictive model predicts state 7 (reference the recuperator diagram in Figure 4-4) to lie in the subcooled regime (x_7<0), the cold end approach temperature should be forced to become

larger instead of smaller (pushing state 1 towards the saturated liquid line). In this instance a negative capacitance rate is observed due to a combination of the drastic increase in the specific heat along the bubble line and the linear pressure drop that is equally applied to each recuperator sub-section (reference issue number six in Table 4-3).

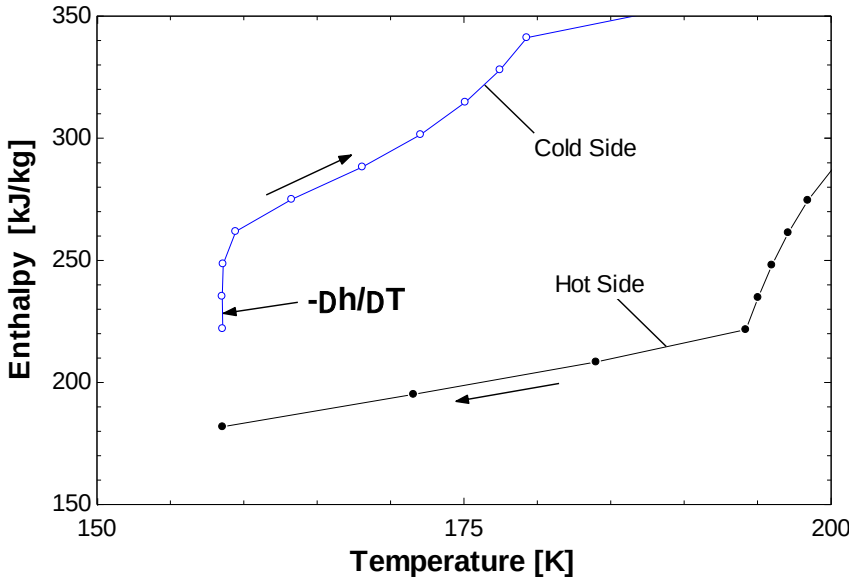

Figure 4-6: Enthalpy as a function of temperature for a binary mixture of R14 and R23. A negative cold side capacitance rate is observed in the first recuperator sub-section as a result of too large a value of the cold end approach temperature.

Table 4-3 summarizes the failure modes detailed in this chapter. Included are the finned tube lengths used to relay each condition back to the iterative solution procedure as well as the corrective action required. Errors not captured here are related to the use of Refprop in calculating thermodynamic property data. Currently, inputs to Refprop that result in convergence errors are tabulated in a separate procedure within the predictive model. Before a call is made to the thermodynamic property database, values are compared with those previously logged into the procedure. If a match is found, a small modification to one of the inputs is made (in the case of enthalpy this is on average ~0.05 kJ/kg; pressure changes

are approximately 0.1 kPa). Often this is all that is required to obtain a solution in Refprop and will not result in a significant increase in modeling error. This issue has been of particular concern for conditions near the bubble line (R14+R23 pair), specifically where the enthalpy at state 1 (h_1) is implicitly calculated by the thermodynamic model. In order to correct this issue, if the Refprop error procedure modifies variable values more than once (during iteration through the pressure drop section), calculation of h_1 is halted and the resulting residual/error in the implicit model reported to the user in a warning message.

Table 4-3: Overview of failure modes presented in chapter 4. In text superscripts can be referenced for additional information on each failure condition.

Issue #	Failure Condition	Reported $L_{rec,f}$ [m]	Solution
1	$\varepsilon \geq 1$	1000000	Increase $T_{rec,c,diff}$
2	$\varepsilon \leq 0$ AND $\dot{Q}_{rec} \geq 0$	2000000	Increase $T_{rec,c,diff}$
3	$\varepsilon \leq 0$ AND $\dot{Q}_{rec} < 0$	3000000	Decrease $T_{rec,c,diff}$
4	$\dot{C}_{rec,h} \leq 0$	4000000	Decrease $T_{rec,c,diff}$
5	$\dot{C}_{rec,c} \leq 0$ and $x_7>0$	7000000	Decrease $T_{rec,c,diff}$
6	$\dot{C}_{rec,c} \leq 0$ and $x_7<0$	5000000	Increase $T_{rec,c,diff}$

4.4 Optimization

The iterative solution procedure described in section 4.2.1 can be used along with one of the optimization algorithms that are available in EES in order to maximize cooling capacity at a given load temperature, T_7. The current model revision allows for independent optimization of either 1) the compressor suction and discharge pressures, $P_{low,2nd}$ and $P_{high,2nd}$ respectively, or 2) the 2nd stage mixture composition, $\bar{y}_{2nd}$. The compressor suction

and discharge pressures are directly related to the static cycle charge pressure and orifice diameter, both of which are provided as outputs to the predictive model.

A robust multi-dimensional optimization routine is required for mixtures with more than two constituents (as well as for case 1 above, regardless of mixture composition). Five multi-dimensional routines are available in EES at the time of this writing, including the conjugate directions method, the variable metric method, the genetic method, the Nelder-Mead simplex method, and the DIRECT algorithm. A brief description of each method may be found in Klein and Nellis (2012). For repeated or time sensitive optimizations, the direct search method is most appropriate. The direct search method does not require the derivatives of the objective function to be calculated and was found to converge reliably over a range of model inputs. Global optima (maximizing both compressor suction and discharge pressures as well as mixture composition) were identified using the genetic optimization algorithm, as the method is not affected by the starting values of the independent parameters or local optima (Keppler et al., 2004). For this reason it was also used in tuning of the compressor map based on the analysis of experimental data as will be discussed in Chapter 6. The disadvantage of using the genetic method is increased computation time.

4.5 Model GUI

A graphical user interface (GUI) was created using the diagram window in EES to facilitate the use of the predictive model, as shown in Figure 4-7. Users can adjust the input parameters and configure the model settings depending on the analysis objective. The GUI is currently setup for pure fluid (nitrogen or argon) and binary mixtures (R14 and R23) in the 2^{nd} stage cycle. It is assumed that R410A is used in the precooling stage. The ‘record array

values in .txt file?' setting controls whether the array parameters from the thermodynamic model or iterative solution procedure are saved in an external text file. Optimization can be conducted using the 'Min/Max' control button. Important cycle state points from an analysis are output onto the 2nd stage cycle schematic, which also details the resultant model convergence error. These points will also be displayed on a pressure-enthalpy property plot as shown.

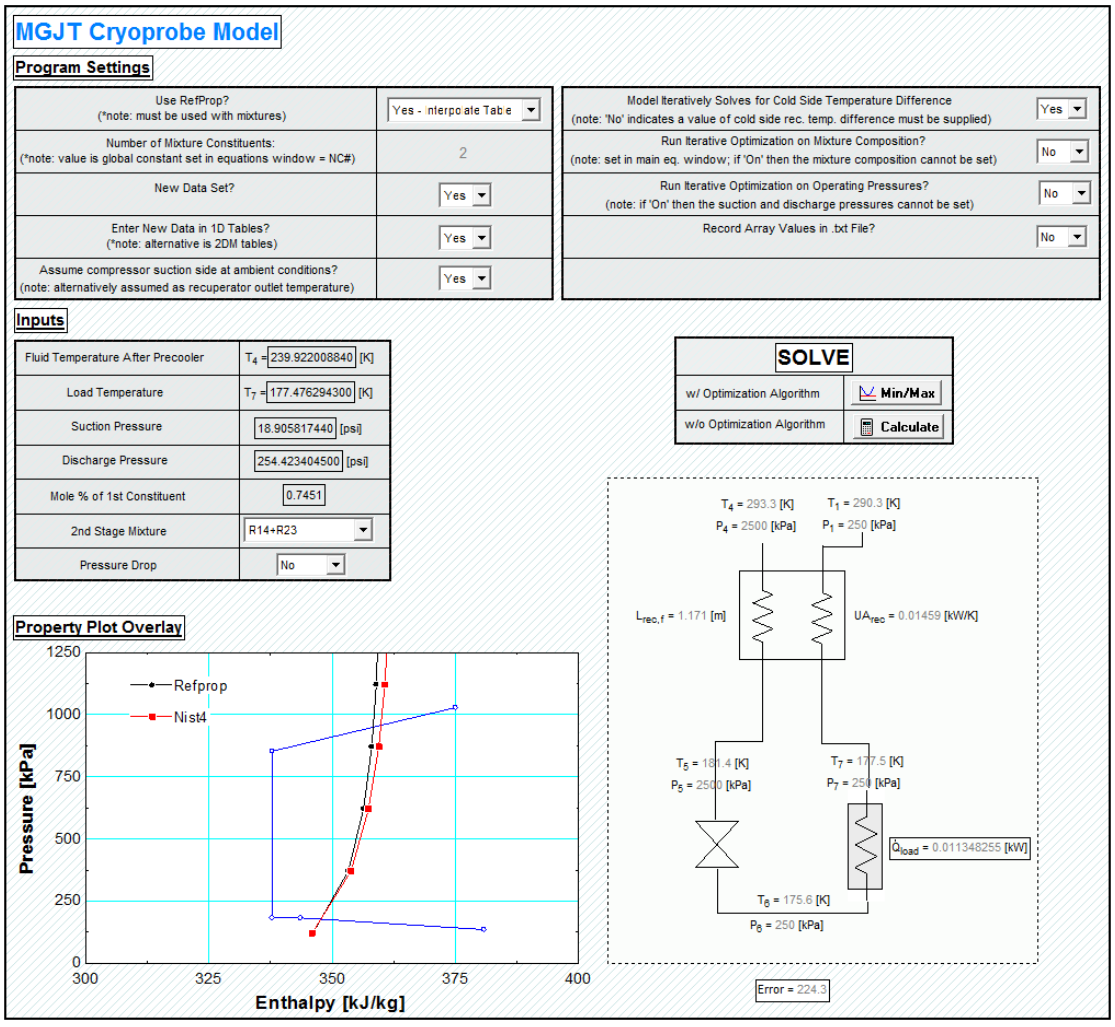

Figure 4-7: Detail of the predictive model graphical user interface.

A child diagram window can be accessed by selecting the recuperative heat exchanger in the cycle schematic. Included are plots of temperature, quality, and enthalpy as a function of axial recuperator position. The temperature and quality plots detail predicted trends for both the warm and cold fluid streams.

5 Experimental Test Plan and Data Analysis

5.1 Mixture Selection

One of the objectives of this research was to verify the predictive capability of the model for test points outside of the original conductance correlation dataset. Furthermore, it is desired to evaluate the usefulness of the model in system level optimizations, i.e. the accuracy of the compressor map as well as the ability of the model to determine the effects of the 2nd stage static charge pressure and orifice diameter on cryoprobe performance. One way to accomplish this is to independently vary one of the system input parameters while keeping the others constant, ensuring that the trends match those predicted by the model. In order to obtain as much experimental data as possible in a short timeframe, the following input parameters were varied: heat load at the tip of the cryoprobe, $\dot{Q}_{load}$ and the static 2nd stage cycle charge pressure (effectively the compressor suction and discharge pressures, $P_{low,2}$ and $P_{high,2}$, respectively). These parameters were chosen in favor of the orifice diameter as no disassembly of the vacuum enclosure or hardware modifications is required. The majority of data points used in development of the original conductance correlations were taken using a binary blend of R14 and R23; as a result, these two constituents are chosen for the experimental test mixture to eliminate any potential dependency related to the use of

different refrigerants. The effects of mixture composition and orifice diameter are included as part of the future work.

It is very difficult to maintain a constant mixture composition for each experimental data point. Changes in composition after the initial charge are as a result of preferential absorption of one or more of the mixture constituents into the compressor oil (H. M. Skye, 2011), differential pooling by condensation based on the individual component boiling points (during cycle operation), and losses associated with the modification of the static cycle charge pressure. Figure 5-1 details the shift in mixture composition for a binary mixture of R14 and R23 as a function of the cryoprobe tip temperature, T_7, for two different experimental data points. As shown by the plot, increases in the load temperature cause the mole fraction of R14 to decrease. In order to mitigate the effects of refrigerant absorption in the compressor oil, the system is initially charged to the highest static pressure for the test range of interest. The system is run for approximately one hour and allowed a period of at least 48 hours of non-operation prior to conducting an experimental test run. Additional data points taken at various system static charge pressures are overlaid on Figure 5-1. These points show a minimal shift in the overall mixture composition due to gas chromatograph sampling at steady state or changes in the static 2nd stage charge pressure between datasets.

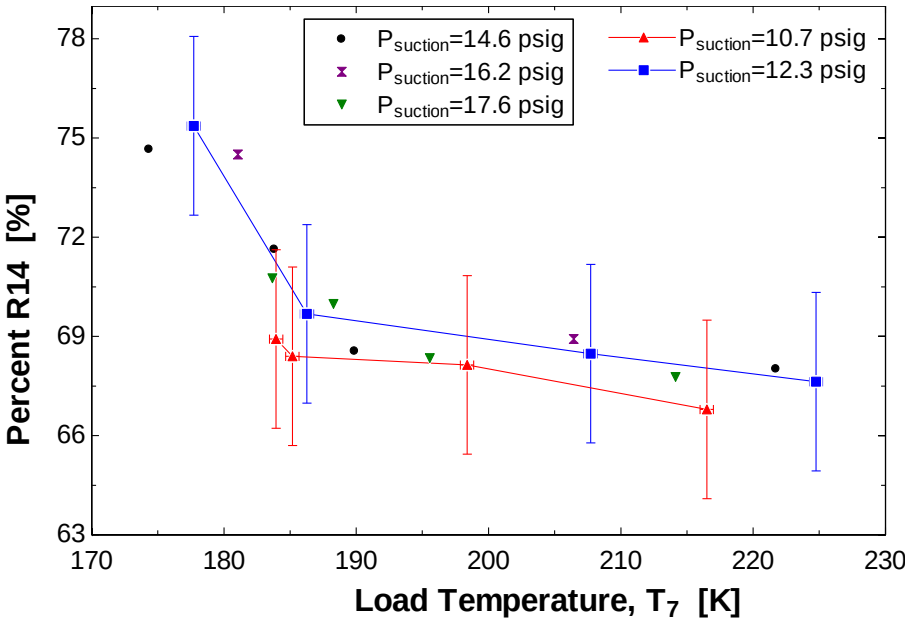

Figure 5-1: Mole percentage R14 as a function of the load temperature for a binary mixture of R14 and R23.

The 2nd stage cycle can be charged initially using a refrigerant premix or formulated from the pure refrigerant bottles. For a binary mixture, the individual components can be combined using Dalton's rule, presented in equation (5.1) (S. A. Klein & G. Nellis, 2012).

$$P = P_A + P_B \tag{5.1}$$

where P is the desired charge pressure of the refrigerant mixture and P_X represents the partial pressure of each constituent. Assuming each individual component behaves as an ideal gas at P, its partial pressure in the mixture is equal to the product of the constituent mole fraction and the total charge pressure.

$$P_X = y_i P \tag{5.2}$$

If, for example, a 40% blend (mole fraction) of R14 and R23 is desired at an initial charge pressure of 100 psig, the user could first charge the system to 40 psig with R14 (equal

to the partial pressure of R14 in the mixture) and balance the cycle charge with R23. Practical application of this technique with the experimental test facility proved to be tedious, and the observed composition after charging varied greatly. Thus, a premixed synthetic refrigerant mixture is used for all experimental testing.

5.1.1 Experimental Test Range

The performance characteristics of the 2nd stage refrigerant mixture are an important factor in experimental testing. The predictive model can be used to approximate experimental data trends based on the independent parameters of interest, in this case the 2nd stage static cycle charge pressure and the heating load applied to the nichrome wire heater. Since the static charge pressure cannot be measured during system operation, model analyses are performed using the compressor suction and discharge pressures. The approximate operating range of the experimental test facility is detailed in Table 5-1 and is based on previous data collected using a binary mixture of R14 and R23.

Table 5-1: Approximate test range for experimental two stage cryoprobe

Input Parameter	Range	Test Point
Compressor discharge pressure ($P_{high,2nd}$)	160-290 psig (1103-2000 kPa)	195 psig (1344 kPa)
Compressor suction pressure ($P_{low,2nd}$)	5-100 psig (34-690 kPa)	52.5 psig (362 kPa)
Load temperature (T_7)	165-210 K	175 K
Orifice diameter ($d_{orifice}$)	0.008-0.025 in. (0.20-0.64 mm)	-

Based on the range of the independent parameters in Table 5-1, a 110 point parametric study was conducted using an arbitrary mole fraction of R14 (R14 and R23 mixture) at a constant load temperature of 175 K. The results of this analysis are shown in

Figure 5-2. As shown by the plot, the cooling load, $\dot{Q}_{load}$, drops off rapidly for values of the compressor suction pressure between 15 psig and 27 psig. No significant trends in cryoprobe performance are observed with respect to the compressor discharge pressure. Including the empirical pressure drop correlations would further reduce the region over which a measurable cooling load could be achieved (the effects of pressure drop will be discussed more thoroughly in Chapter 6 but were not found to have a significant impact on experimental trends predicted by the model). Regarding the orifice diameter, the 0.21 mm contour is observed to trend incorrectly at low values of the compressor suction pressure (above $P_{high,2}$=290 psig). It is expected, based on the Bernoulli model, that the orifice diameter should increase with the downstream pressure and decrease with reducing upstream pressure. The error shown occurs as a result of curve extrapolation by the plotting software due to the limited resolution of the parametric study. Based on the plotted data, the optimal operating condition for this mixture would be achieved at an orifice diameter somewhere between 0.21 and 0.27 mm and at a compressor suction pressure near the low end of the test range.

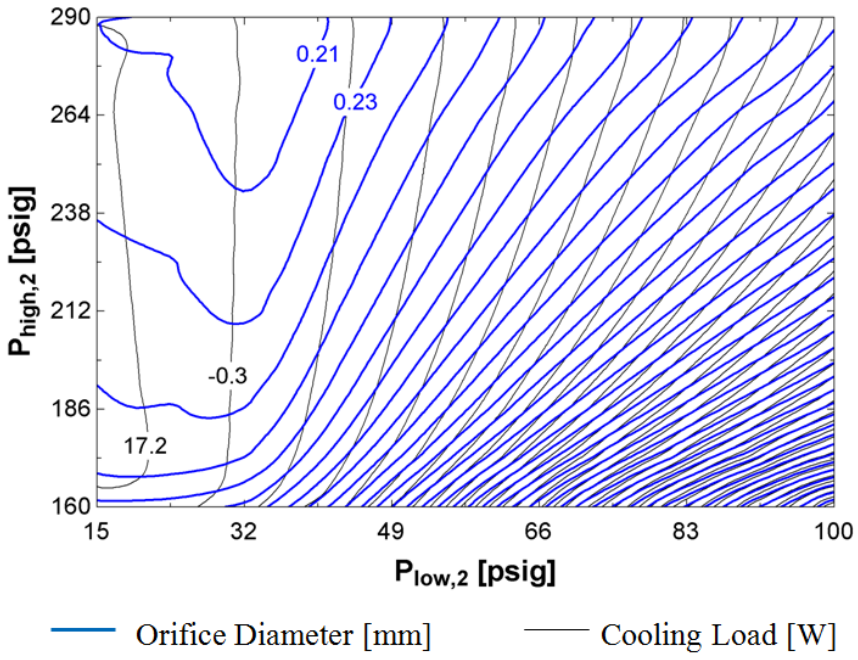

Figure 5-2: Compressor discharge pressure as a function of compressor suction pressure with contours of cryoprobe cooling load and orifice diameter for a binary mixture of R14 (20% mole fraction) and R23. Results shown are for the case with no pressure drop through the precooling or recuperative heat exchangers.

The poor trends in cryoprobe refrigeration performance exhibited by this mixture reduce its usefulness as an experimental test fluid for this investigation. The steep drop off in cooling load with the compressor suction pressure would act to further condense the allowable test range, which would result in an increase in experimental uncertainty. Additionally, a better understanding of the dynamic between cooling load and the high side pressure is desired. For these reasons, a study was conducted to obtain an R14+R23 mixture blend better suited for the purposes of this testing.

5.1.2 Optimization Matrix

Based on the discussion in section 5.1.1, an ideal refrigerant mixture for the experimental investigation would possess the following two characteristics.

1. Measurable values of cooling load over the range of compressor suction and discharge pressures. This condition must be met given a low cryoprobe tip temperature is used as an input to the predictive model (as higher load temperatures will result from increases in the input load to the nichrome wire heater).
2. An optimum operating condition near the center of the allowable test range for the experimental facility.

In an effort to improve upon the generic refrigerant mixture reviewed in Figure 5-2, the mixture composition optimization routine in the model was utilized to shift the optimum towards the center of the test range. The initial optimization was conducted based on the 'Test Point' values indicated in Table 5-1, assuming no pressure drop through the precooling or recuperative heat exchangers. The results of this analysis are provided in the second row of Table 5-2. The extremely low values of cooling load observed in this table are as a result of the over prediction in the compressor suction pressure (at the center of the test range). Previous data were collected using the 2^{nd} stage bypass valve to regulate the mass flow rate of refrigerant through the system, allowing for high compressor suction pressure at low 2^{nd} stage mass flow rates. For this investigation, all data points were obtained with the bypass valve fully closed as this represents the actual operating condition of the hardware in a surgical environment. It is also the only configuration which allows for the application of the volumetric compressor efficiency model presented in section 3.3.4. In order to ensure measureable values of cooling load were realized over the entire test range, an analysis was conducted after each optimization, similar to that shown in Figure 5-2 (a better measure than

the cooling load data provided in Table 5-2). Based on the data from the first optimization, the load temperature was increased by 5 K and a second mixture optimization conducted. Repeating this process at 185 K yielded a positive cooling load even at a low side pressure of 52.5 psig.

Table 5-2: Optimization matrix for a binary mixture of R14 and R23.

Mole Fraction R14 [-]	T_7 [K]	$\dot{Q}_{load}$ [kW]	Procedure
0.2	175	-0.051	Generic binary mixture
0.61	175	-0.032	Optimize R14 mole fraction (no pressure drop)
0.47	180	-0.0091	Increase T_7 by 5 K and optimize R14 mole fraction
0.38	185	0.0021	Increase T_7 by 5 K and optimize R14 mole fraction
0.38	185	-0.073	Included pressure drop correlations
0.60	185	-0.023	Optimized R14 mole fraction (with pressure drop)

The final mixture optimization was performed with the empirical pressure drop correlations included in the thermodynamic model. Interestingly, the results closely match those for row two in the table. An updated contour plot detailing the system response after the final optimization is shown in Figure 5-3. As can be seen from the plot, measureable values of cooling load are observed over the entire test range. In addition, the cooling load trends with both the high and low side system operating pressures. Since the load temperature used is near the center of the test range, additional increases will result in higher values of cooling load.

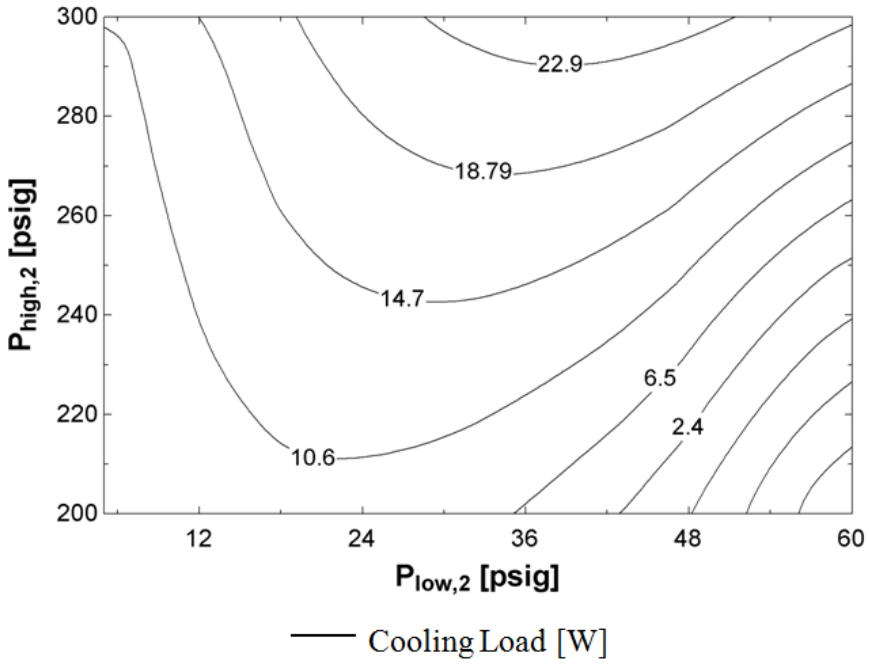

Figure 5-3: Cryoprobe cooling load as a function of the compressor discharge and suction pressures for an optimized mixture of R14 and R23 (at 185 K).

It is additionally useful to illustrate the dynamic between the cryoprobe cooling load and the 2nd stage static cycle charge pressure and orifice diameter, which is shown over the operating range of the experimental test facility in Figure 5-4. This plot emphasizes the design approach capability of the model, as the metrics analyzed can be tuned with no modifications to existing hardware. From this plot, the global optimum for the refrigerant mixture can be determined.

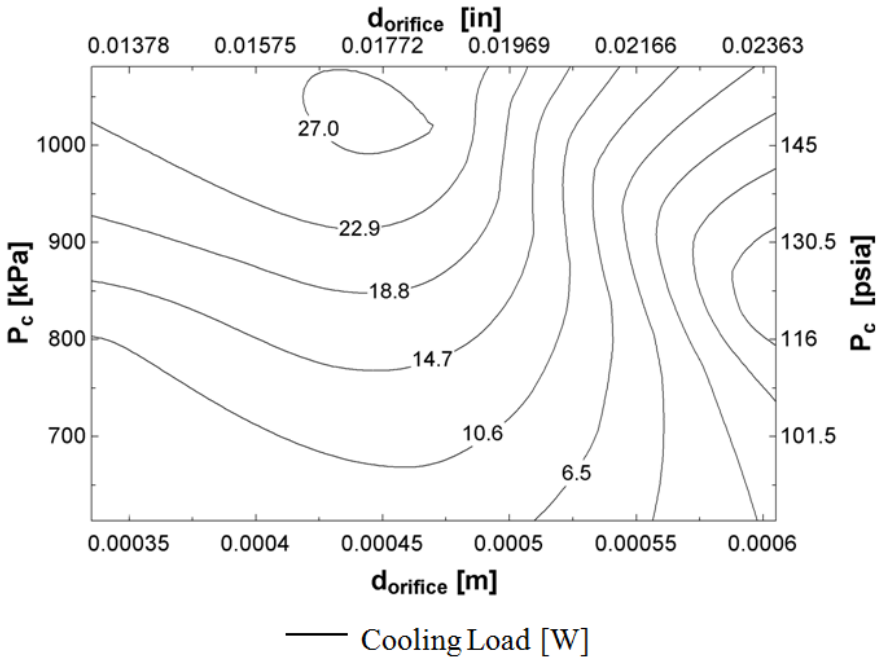

Figure 5-4: Cryoprobe cooling load as a function of the 2nd stage cycle static charge pressure and orifice for an optimized mixture of R14 and R23 (185 K).

5.2 Experimental Test Procedure

All data collected during this investigation was obtained with the 1st stage cycle operating at the manufacturer specified operating condition. A base charge of approximately 145 psig was used for the precooling refrigerant (R410A). Bypass valves on both the 1st and 2nd stage cycles were fully closed. For the 2nd stage this is required to allow for the use of the compressor map in the predictive model. Also, an orifice diameter of 0.0175 in. was used in the 2nd stage. The following sections detail the preliminary test plan and highlight important considerations for operation of the experimental test facility.

5.2.1 Test Matrix

The two independent parameters analyzed in this experimental investigation were the 2nd stage static charge pressure and the load applied to the nichrome wire heater. A test

matrix was formulated to help guide data collection and ensure that the measurement series captures system performance with adequate resolution. This is presented in Table 5-3. The limits on cooling load are based on a combination of preliminary experimental testing and outputs from the predictive model.

Table 5-3: Experimental test plan for the 2nd stage system.

$d_{orifice}$=0.175 in.						
Charge Pressure, P_c [psig]						
85	Cooling Load, $\dot{Q}_{load}$ [W]	2	3	4	-	-
	Load Temperature, T_7 [K]					
93	Cooling Load, $\dot{Q}_{load}$ [W]	2.5	3.5	5.5	-	-
	Load Temperature, T_7 [K]					
101.7	Cooling Load, $\dot{Q}_{load}$ [W]	2.75	3.75	4.5	5.5	6.8
	Load Temperature, T_7 [K]					
118.3	Cooling Load, $\dot{Q}_{load}$ [W]	3.5	5	6.5	8	10
	Load Temperature, T_7 [K]					
126.7	Cooling Load, $\dot{Q}_{load}$ [W]	3.5	5.25	6.75	8.5	11.17
	Load Temperature, T_7 [K]					
135	Cooling Load, $\dot{Q}_{load}$ [W]	3.5	5.25	6.75	8.5	11.17
	Load Temperature, T_7 [K]					
143.3	Cooling Load, $\dot{Q}_{load}$ [W]	3.5	5.25	6.75	8.5	11.17
	Load Temperature, T_7 [K]					

Significant changes in cycle charge pressure were observed during test facility operation as a result of refrigerant condensation within the coldest portions of the system. After shutting down the cryoprobe, it takes a few hours for the refrigerant to warm to ambient temperature as heat transfer is limited by radiation with the wall of the vacuum enclosure and conduction through the air. Thus, exact modifications in the system charge pressure based on Table 5-3 were very difficult to achieve. Instead, after each data run the charge pressure was reduced by between 5 and 10 psig from the low pressure 2nd stage cycle

Schrader valve. This eliminated experimental system downtime between data points and was found to still provide an adequate pressure distribution for analysis. Increments in heating load at each pressure also varied from that detailed in Table 5-3 depending on the observed response of the system. The experimental uncertainty increases as the temperature spanned by the recuperator decreases due to the ±0.5 K absolute temperature measurement uncertainty between the platinum resistance thermometers (PRTs) spaced throughout the shell side of the recuperator. Therefore, more data points were taken at lower values of heater input load.

5.2.2 Steady State Operating Conditions

The experimental test facility was carefully operated to minimize error between data points, and to maintain consistency with previously documented test methods. Cool down of the cryoprobe system to tip temperatures below 180 K, including the time required for system startup, was observed to take anywhere from 2 to 4 hours, depending on the static 2^{nd} stage charge pressure. Figure 5-5 shows a portion of the operating curve, detailing both the load temperature and 2^{nd} stage high side pressure with the former starting at about 288 K. The spikes shown in the compressor discharge pressure result from the actuation of bypass solenoid valves that allow oil captured by the two oil separators in the 2^{nd} stage cycle to drain back into the compressor. For many of the early data points the solenoids were activated at 30 min. intervals during system cool down (the precooling cycle solenoid valve was actuated every 1.5 hr.). As a result of the decrease in the pressure difference over the compressor, the temperature at the load location momentarily increases.

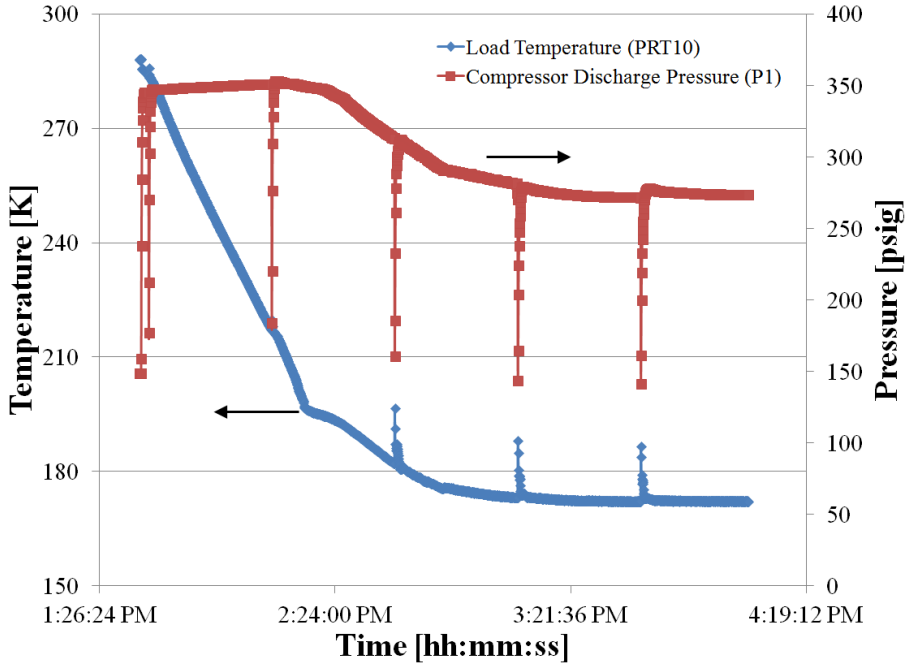

Figure 5-5: Load temperature and high side pressure as a function of time for the 2nd stage cycle using a binary mixture of R14 (~60%) and R23.

Following the compressor discharge curve a reduction in pressure is shown as the refrigerant mixture becomes saturated in the colder portions of the cryoprobe. For the experimental data point shown in Figure 5-5, the temperature change with time begins to decrease at 3:00 pm (as the refrigerant mixture is pushed further into the sub-cooled regime within both the recuperator and at the location of the expansion orifice). In order to minimize the duration of the cool down period, the nichrome wire heater was not activated until the temperature at the load location reduced to slightly less than what was anticipated at steady-state. This temperature was largely determined based on experience with previous data points, but for values of cooling load less than 2.5 W was often taken to be around 165 K. Once the nichrome wire heater is switched on (about 2:50 pm in Figure 5-5), the solenoid valves only need to be activated once every two hours. This allows the system more time to achieve an equilibrium condition.

Two different factors were examined in order to determine potential errors resulting from inconsistent operation of the experimental test facility. The first is related to the selection of a steady-state operating criteria (definition of a system equilibrium condition). Procedures outlined in previous research suggest that, at steady-state, the change in temperature at the load location should be no greater than 0.25 K during a 20 minute period (Passow, 2012). This deviation may be quantified by examining the change in internal energy at the location of the nichrome wire heater with respect to the applied heat load:

$$\frac{dU}{dt} = mc\frac{dT}{dt} \tag{5.3}$$

where m is the mass of the AISI type 304 ¼" stainless steel section along which the heater is coiled, c is the materials specific heat, and dT/dt represents the equilibrium condition previously defined. Based on equation (5.3) the change in internal energy is calculated as 95 milliwatts, which as a fraction of the lowest applied heat load examined during testing (1.25 W) is less than 7.6%. A similar calculation was performed for every test point, with some results exceeding the 0.25/20 K/min target. The average deviation was calculated to be less than 2.8%.

A separate analysis was performed in order to quantify errors associated with over-estimation of the load temperature at steady-state, i.e. approaching the steady-state load temperature from a value of T_7 higher than what is actually observed at a given operating condition. This test was performed over the course of four days, repeating tests at three different values of the applied heat load (approximately constant charge pressure). The results are shown in Table 5-4. As shown, the repeatability error is relatively small for both the 2.5 and 4.5 W cases. At 6 W, for the charge pressure analyzed, two very different

temperatures were obtained depending on whether the steady-state condition was approached from high or low values of the load temperature. At this point, the refrigerant mix operates very near to the edge of the vapor dome throughout a portion of the recuperator. Small increases in the applied heat load result in significant changes in the steady-state operating temperature at the cold end of the cycle. It is likely that a decrease in the static cycle charge pressure over the four day period also played a contributing role. Nonetheless, these results serve as verification of the test method utilized.

Table 5-4: Results quantifying experimental deviation from over-estimation of the temperature at the tip of the cryoprobe.

Measured Heater Power [W]	Day 1 [K]	Day 2 [K]	Day 3 [K]	Day 4 [K]
2.5	172.3 ↓	-	173.25 ↓	174.5 ↑
4.5	181.75 ↓	183.25 ↑	180.75 ↓	-
6.0	186.75 ↓	187 ↓	187.25 ↓	198 ↑
↑ = Overestimated Load Temp. (T_7); ↓=Underestimated Load Temp. (T_7)				

5.3 Experimental Data Analysis

A significant amount of post processing was required in order to analyze the experimental data. This ranged from simple calculations such as that used to determine the applied heat load at each steady-state operating point to the estimation of the heat exchanger conductance from the temperature measurements along the shell side of the recuperator. This section defines the relationships between the predictive model outputs and experimental measurements. It also details the calculation of relevant cryoprobe system performance metrics.

5.3.1 Preliminary Data Analysis

Analysis of the experimental data begins by creating a plot of load temperature as a function of time over the steady-state operating period. This plot highlights any errors which

may not have been captured during data collection, specifically significant temperature drift. After preliminary review, all data from the steady-state analysis period (approximately 20 minutes in duration) is averaged and migrated to an EES (Klein, 2013a) lookup table. The composition of the refrigerant mixture must be determined from the uncorrected R14 and R23 curve areas output by the integrator. The calculation of the mixture mole fraction for a single constituent in an *N* component refrigerant is detailed in equation (5.4):

$$\bar{y}_{2nd,1} = \frac{A_{1,uc} RF_1}{\sum_{i=1}^{N} A_{i,uc} RF_i} \tag{5.4}$$

where $A_{i,uc}$ is the uncorrected area output for the *i*th constituent and RF_i is the response factor used to correct the area output from the gas chromatograph (GC). Response factors for R14 and R23 were computed by Skye (2011) based on a calibrated gas mixture sample certified to ±1% by NIST traceable standard from Air Liquide. A three point GC test taken directly from the 60% R14 and R23 refrigerant bottle used for this investigation was conducted to verify the accuracy of these response factors (the R14 and R23 pre-mix was ordered from Air Liquide as a certified master class mixture with a ±1% concentration tolerance). The results agreed with the bottled mixture composition to within the uncertainty of the GC.

In order to accurately compare experimental data to predictive model outputs, relationships between cycle state points relevant to this analysis and actual measurement locations were defined and are summarized in Table 5-5 and the accompanying figure (Figure 5-6). Due to the availability of measurement instrumentation there is little ambiguity in these associations.

Table 5-5: Relationships between predictive model states and measurement instrumentation used in experimental test facility (also reference Figure 5-6).

Variable Name	Sensor Name
T_{amb}	TC 3
P_{amb}	P_amb (barometer reading)
$\dot{m}_{2nd}$	GMC_massflow_coriolis
P_3	P3
T_5	PRT 13
P_5	P2
T_6	PRT 12
T_7	PRT 10
P_7	P3
T_1	PRT 14
P_1	P4
$P_{suction}$	P5

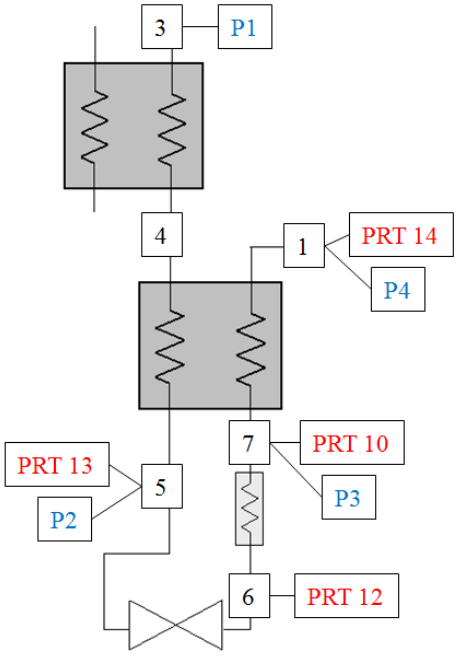

Figure 5-6: Schematic detailing cycle state points relevant to analysis of the 2nd stage cycle. Highlighted are the measurement instrumentation utilized at each thermodynamic cycle state point.

5.3.2 Numerical Heat Exchanger Analysis

A second procedure was added to the main equations window of the predictive model in EES in order to analyze the experimental data. The condition of the mixed refrigerant at state 4 (reference Figure 5-6) can be determined by first taking an energy balance over the cold side of the recuperator as shown in equation (5.5).

$$\frac{\dot{Q}_{rec}}{\dot{m}_{2nd}} = h_1 - h_7 \tag{5.5}$$

Heat transfers adiabatically from the warm side of the recuperator (assuming negligible parasitic heat loss as a result of the multi-layer insulation and vacuum enclosure); thus the warm side energy balance in equation (5.6) can be rearranged to solve for the enthalpy at state 4.

$$\frac{\dot{Q}_{rec}}{\dot{m}_{2nd}} = h_4 - h_5 \tag{5.6}$$

The temperature at state 4 can be determined by estimating the pressure drop through the precooling heat exchanger. As in the thermodynamic model, the pressure is assumed to lie halfway between the compressor discharge pressure and the pressure of the mixed refrigerant exiting the warm side of the recuperator.

$$P_4 = \frac{(P_3 + P_5)}{2} \tag{5.7}$$

$$T_4 = enthalpy(h_4, P_4) \tag{5.8}$$

Evaluation of T_4 by the energy balance method described above resulted in a pinch point violation near the warm end of the heat exchanger for several experimental test points. There are two likely reasons for this violation. The first is an overestimation of the pressure drop for the mixed gas flowing through the precooler. The second is due to errors in property data from the RefProp database (Lemmon et al., 2013). Further discussion on observed thermodynamic property discrepancies will be provided in chapter 6. Regardless of the non-physical solution at state 4 for these test points, no improvement in the estimation of T_4 can be made that would still allow for the use of the shell (cold) side PRT measurements in the experimental data analysis procedure (as is evident from the following analysis).

The temperature profile of the refrigerant through both sides of the recuperator can be evaluated based on the known fluid inlet/outlet conditions (states 5, 7, and 1 from Figure 5-6) and the PRT measurements taken throughout the shell (cold) side of the heat exchanger. The solution methodology closely matches that presented in chapter 3, where the heat exchanger is discretized into smaller sub-sections in order to account for large variations in the specific heat of the mixed refrigerant. Knowing the temperature at several locations throughout the heat exchanger increases the accuracy of this method. Since the PRTs are evenly spaced along the axial flow direction, each diametrically opposed pair can be averaged to determine the corresponding cold side node temperature at the section interface, making a total of six sections as shown in Figure 5-7. The pressure at each node can be approximated by linearly distributing the pressure drop from states 7 to 1. An energy balance can then be taken over each section to determine the heat transferred from the warm fluid stream. An example of this calculation is also shown in Figure 5-7. The corresponding energy balance for the warm

stream side can be rearranged to solve for each nodal enthalpy, starting from either states 4 or 5. An example of this calculation is shown, stepping from state 4 to the 2nd node in the heat exchanger by equation (5.9).

$$h_{rec,h}[2] = h_{rec,h}[1] - \frac{\dot{Q}_{rec}[1]}{\dot{m}_{2nd}} \tag{5.9}$$

The effectiveness-NTU relations can then be utilized, as in chapter 3, to determine the total heat exchanger conductance.

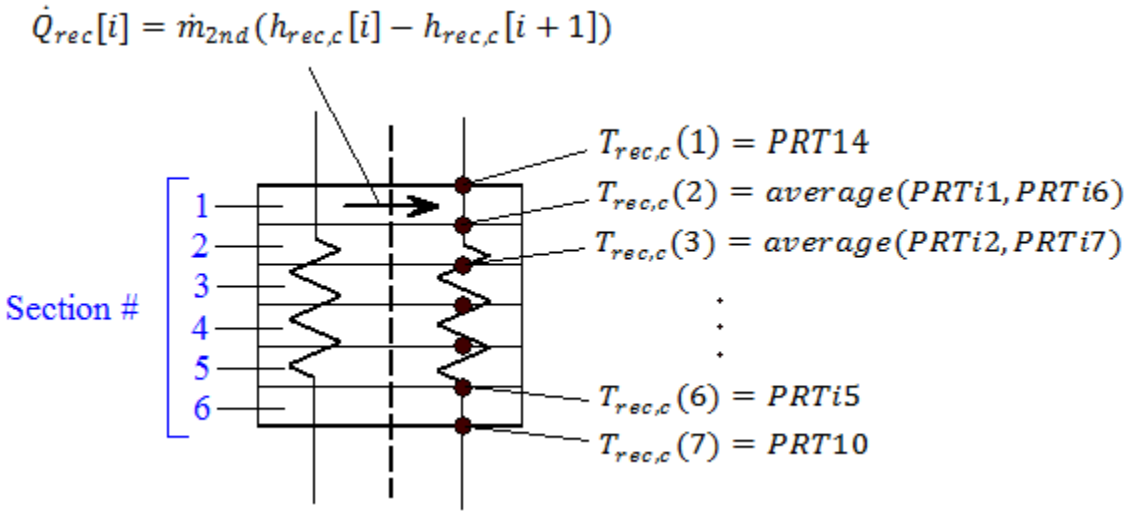

Figure 5-7: Schematic of the recuperator discretized into smaller sub-heat exchanger sections. The initial discretization is based on the location of the diametrically opposed PRTs.

The resolution of this method can be further increased by splitting each section into even smaller units. As in Figure 3-4, the optimal number of sub-sections (number of sub-heat exchanger units within each of the six primary sections) was found by comparing it vs. the ratio of the refrigeration load to the total heat exchanger conductance (Q_{load}/UA_{rec}). This comparison is detailed for a single experimental test point in Figure 5-8 which shows that only about three are needed.

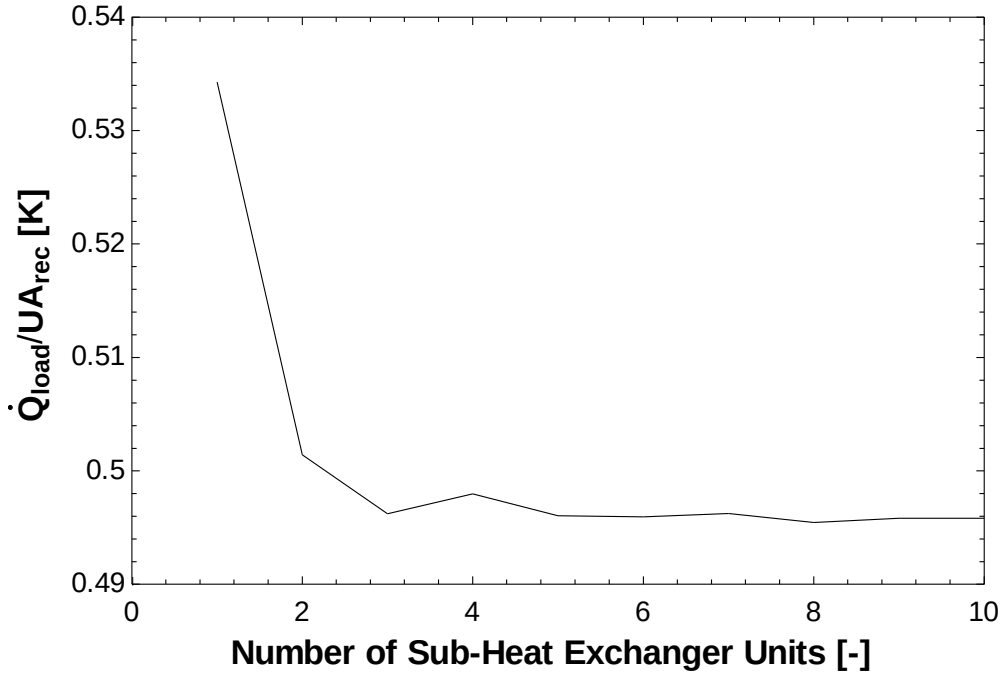

Figure 5-8: Ratio of the refrigeration load to the heat exchanger conductance (recuperator) as a function of the number of sub-heat exchanger sections (contained within each of the six primary sections).

6 Results

6.1 Tuning of the Predictive Model

This chapter describes key predictive model improvements that were made based upon the results of experimentation with the mixed gas Joule-Thomson cryoprobe test facility. It also reviews the usefulness of the tuned model in characterizing system performance, highlighting areas for future improvement.

The first step in the analysis was to compare the processed data collected during the experimental portion of this investigation with the outputs from the predictive model. As described in chapter 4, the model takes in a total of seven inputs. These are listed along with the corresponding measurement sensor name and uncertainty in Table 6-1. Recall from

chapter 2 that the predictive model sets the temperature at state 4 (shown in Figure 5-6) based on the saturation temperature of the 1st stage refrigerant flowing through the precooler.

$$T_4 = T_{sat}(R410A, P = P_{low,1st}) \tag{6.1}$$

Assuming negligible pressure drop through the precooling heat exchanger; $P_{low,1st}$ was calculated as the average of all data points collected. A separate analysis was then conducted to determine the uncertainty in T_4 based on the error in the 1st stage low side pressure and ambient pressure, which are listed in

Table 2-2. A future analysis could also take into consideration the standard deviation of the $P_{low,1st}$ data, which was approximately 1.13 psi (57 experimental test points).

Table 6-1: Summary of input parameters and associated uncertainties for the predictive model. The sensor names corresponding to each input are also identified.

Input Parameter	Sensor Name (reference Figure 3-1)	Uncertainty
$\bar{y}_{2nd}$	N/A (sampled by gas chromatograph)	±0.027
$P_{low,2} = P_{suction}$	P5	±1% relative
$P_{high,2} = P_{discharge}$	P1	±3.0 psi
$T_7 = T_{load}$	PRT 10	±0.5 K
T_4	N/A	±1.0 K
P_{amb}	P_amb (barometer reading)	±0.05 mmHg
T_{amb}	TC 3	±1.0 K

Using the inputs from the experimental data in Table 6-1, the outputs of the model can be evaluated. The primary metric used to evaluate model accuracy was the cooling load generated at the tip of the cryoprobe, $\dot{Q}_{load}$, which was varied experimentally using the nichrome wire heater. This comparison is illustrated in Figure 6-1, where the predicted refrigeration provided by the cryoprobe is plotted as a function of the actual refrigeration load measured experimentally. All data, regardless of 2nd stage charge pressure and mixture composition, are included. As a result of the uncertainty in each of the input parameters, error

bars are shown at one point near both solution boundaries (to provide an idea of the uncertainty range in the predicted value of $\dot{Q}_{load}$). The magnitude of this error was determined using the uncertainty propagation feature in EES (Klein, 2013a) and is illustrated for only two points as a result of the increased computation time required for this analysis.

As can be seen from this plot, the predictive model consistently over-predicts the actual refrigeration load by just over 20%. The modeled data does appear to trend, however, along with increases in cooling load for the experimental system. At actual cooling loads of 3.5 W and 7.3 W, experimental test runs were conducted at several different charge pressures in an effort to isolate one of the main independent parameters. Additional detail regarding trends observed at these two operating conditions is provided in section 6.2.

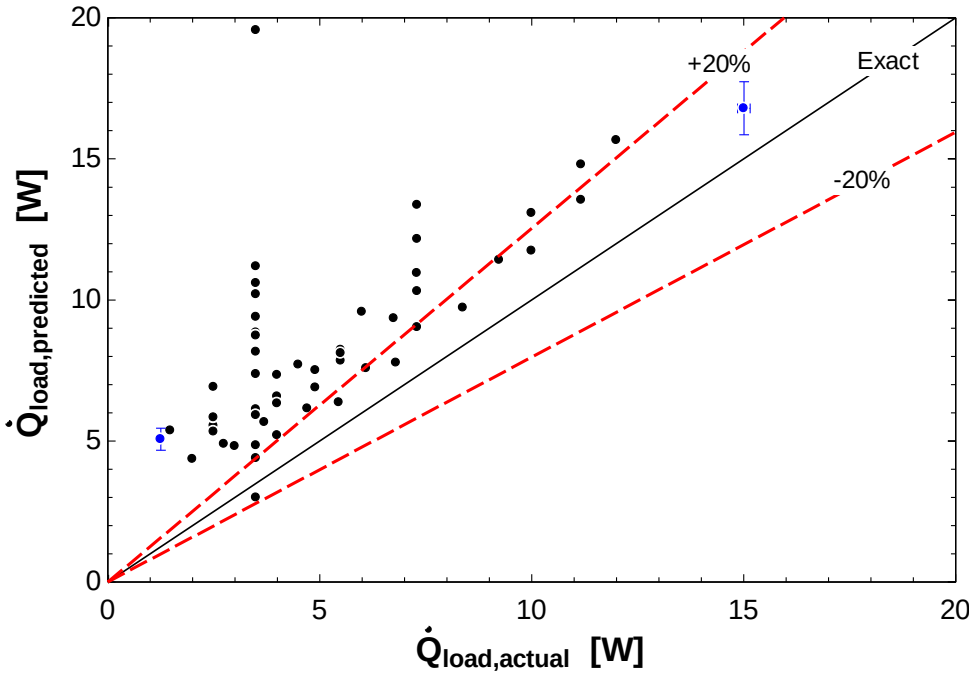

Figure 6-1: Predicted cryoprobe refrigeration load as a function of the value measured experimentally.

Further review of the results from the uncertainty propagation reveals the input parameters that have a large impact on cooling load error. The most significant dependency is on the composition of the refrigerant mixture. As discussed in section 5.1, the mixture composition likely varies from that measured by the gas chromatograph due to differential constituent pooling in the colder portions of the cryoprobe. Compensating for this in the predictive model (possibly by balancing the Gibbs free energy at all points through the system) would likely increase the overall accuracy and explain some phenomena not captured by this analysis. The relative contribution of each of the inputs to the overall uncertainty is shown for a single data point in Table 6-2. These closely match the results for the second data point analyzed. Notice that the uncertainty in the ambient temperature is slightly different than that listed in Table 6-1 as a result of using a mercury thermometer for some of the early tests (as TC 3 was improperly located).

Table 6-2: Uncertainty propagation table for an experimental test point.

$\dot{Q}_{load} = 16.8 \pm 0.94\ [W]$	Partial Derivative	% of Uncertainty
$P_{amb} = 739.8 \pm 0.05\ [mmHg]$	$\partial\dot{Q}_{load}/\partial P_{amb} = 0.0065$	0.00
$P_{discharge} = 310.1 \pm 3.0\ [psig]$	$\partial\dot{Q}_{load}/\partial P_{discharge} = 0.11$	13.3
$P_{suction} = 23.7 \pm 0.13\ [psig]$	$\partial\dot{Q}_{load}/\partial P_{suction} = 0.22$	0.31
$\bar{y}_{2nd} = 0.67 \pm 0.027$	$\partial\dot{Q}_{load}/\partial \bar{y}_{2nd} = -27.9$	64.8
$T_4 = 239.9 \pm 1.03\ [K]$	$\partial\dot{Q}_{load}/\partial T_4 = 0.42$	21.6
$T_7 = 219.5 \pm 0.50\ [K]$	$\partial\dot{Q}_{load}/\partial T_7 = 0.018$	0.01
$T_{amb} = 22 \pm 0.5\ [C]$	$\partial\dot{Q}_{load}/\partial T_{amb} = -0.033$	0.03

6.1.1 Volumetric Efficiency Compressor Model

The analysis presented in Table 6-2 identifies the discharge pressure as one of the three main contributors to uncertainty in the predictive model. The compressor map used in the model solves for the mass flow rate of the refrigerant mix through the 2nd stage cycle

based primarily on the compressor suction and discharge pressures. The original formulation of the volumetric efficiency map relied on data from nitrogen and R23 test runs. In order to determine the appropriate clearance volume ratio and displacement rate in the empirical correlation, a two-degree optimization was performed, minimizing the error between the modeled and measured data. This correlation had not been validated for test points utilizing a refrigerant mixture, which makes the analysis against the experimental data obtained by this research ideal (as the charge pressure is directly varied over the range of the 2nd stage cycle). A comparison between the mass flow rate predicted by the model and that measured experimentally is presented for all the collected data points in Figure 6-2. Further evaluation of the data, for instance by plotting the measured flow rate directly as a function of charge pressure, is not required as the modeled data shows agreement to within 5% for all but a few points.

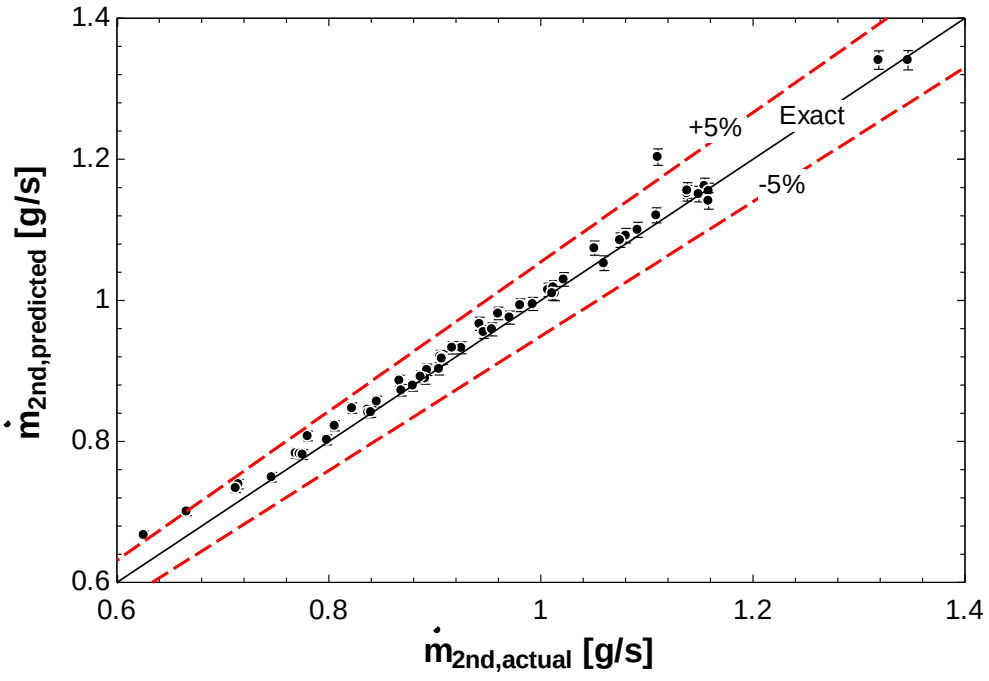

Figure 6-2: 2nd stage mass flow rate predicted by the volumetric efficiency model as a function of the mass flow rate measured experimentally (using a Coriolis flow meter).

The excellent agreement displayed between the measured and modeled data is a testament to the robustness of the empirical correlation. Nonetheless, an optimization was conducted in order to further tune the modeled results. This was accomplished by using the DIRECT algorithm in EES, which varied both the clearance volume ratio and the volumetric displacement rate in the compressor model in order to minimize the RMS error between the experimental data and model outputs.

$$E_{RMS} = \sqrt{\frac{\sum_{i=1}^{\#data\ points} (\dot{m}_{2nd,predicted}[i] - \dot{m}_{2nd,actual}[i])}{\#data\ points}} \tag{6.2}$$

The DIRECT algorithm was found to converge reliably for this analysis and yielded improved results over the genetic optimization routine, including a significant reduction in computation time (1,105 vs. 121 iterations for the genetic and DIRECT methods, respectively). The updated correlation and fit statistics are shown in Table 6-3.

Table 6-3: Updated empirical compressor map correlation. The RMS error is based on comparison of the model outputs with the actual flow rate measured for all data points experimentally.

Correlation	$\dot{V}_{disp}$ [m^3/s]	C [-]	E_{RMS} [g/s]
$\eta_{vol} = \frac{\dot{V}_{suction}}{\dot{V}_{disp}} = 1 + C - C(\frac{P_{discharge}}{P_{suction}})^{\frac{1}{k}}$	0.03065	0.0001611	0.015

6.1.2 Temperature Approximation at State 4 (Recuperator Hot Side Inlet)

The offset observed in the predicted cryoprobe refrigeration load from Figure 6-1 suggests a key difference between an assumed condition in the predictive model and the actual physical solution. Consideration was initially given to the hot side recuperator inlet temperature, state 4 from Figure 5-6, which is assumed based entirely on the saturation temperature of the 1st stage working fluid. If T_4 is under-approximated, the performance of the cryoprobe will be artificially bolstered due to the both a decrease in pressure drop through the recuperator and an increase in the Joule-Thomson effect at the orifice. Further examination of the experimental data was required in order to quantify the discrepancy in T_4. Since no direct measurement of the hot side recuperator inlet temperature is taken, the saturation temperature of the R410A was compared to the temperature of the fluid exiting the recuperator on the cold side (PRT 14 from Figure 5-6). For the majority of test cases, the two values showed good agreement, although the saturation temperature was observed to be as much as 4.1 K less than the PRT 14 in some instances. These findings verify that a correction in T_4 is needed. An attempt to determine the required temperature offset was initially conducted by minimizing the RMS error between the cooling load output for all data points in the predictive model and the experimental data, similar to the methodology in used to correct the compressor map in section 6.1.1. However, performing a single iteration through all the test points is computationally intensive (processing the data through the predictive model originally took about 24 hours).

In an effort to simplify predictive modeling, the empirical pressure drop correlations were omitted from the analysis. As can be seen from Figure 6-3, this effect of this

simplification is primarily to shift the anticipated cooling load to higher values on the y-axis. Most importantly, the trend observed between the modeled and experimental data is retained. This data further validates the use of the model without pressure drop as a design tool.

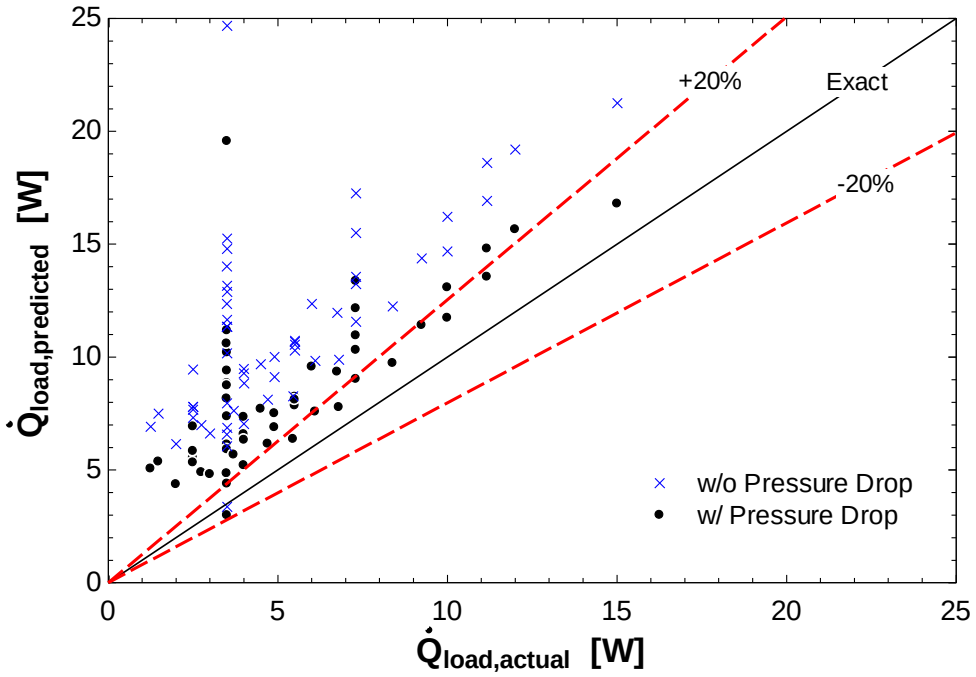

Figure 6-3: Results of an analysis comparing predictive model outputs both with and without the empirical pressure drop correlations.

Although the implementation of the model without pressure drop requires significantly less computation time, its use with EES native optimization algorithms to determine the required correction in T_4 was time prohibitive (even using the most efficient routines). Consequently, a six point minimization of the RMS error between the predicted and experimental results was performed manually. The results of this analysis are illustrated in Figure 6-4 below. As can be seen from the plot, most of the data agree with the actual cryoprobe refrigeration load to within 20%. The response of the system is approximated most accurately between 4 W and 8 W, outside of which the error increases linearly (over-

approximation at low levels of refrigeration, and under-approximation as the cooling load increases). This indicates a linear dependence on T_4 with cooling load, regardless of the mixture composition or charge pressure.

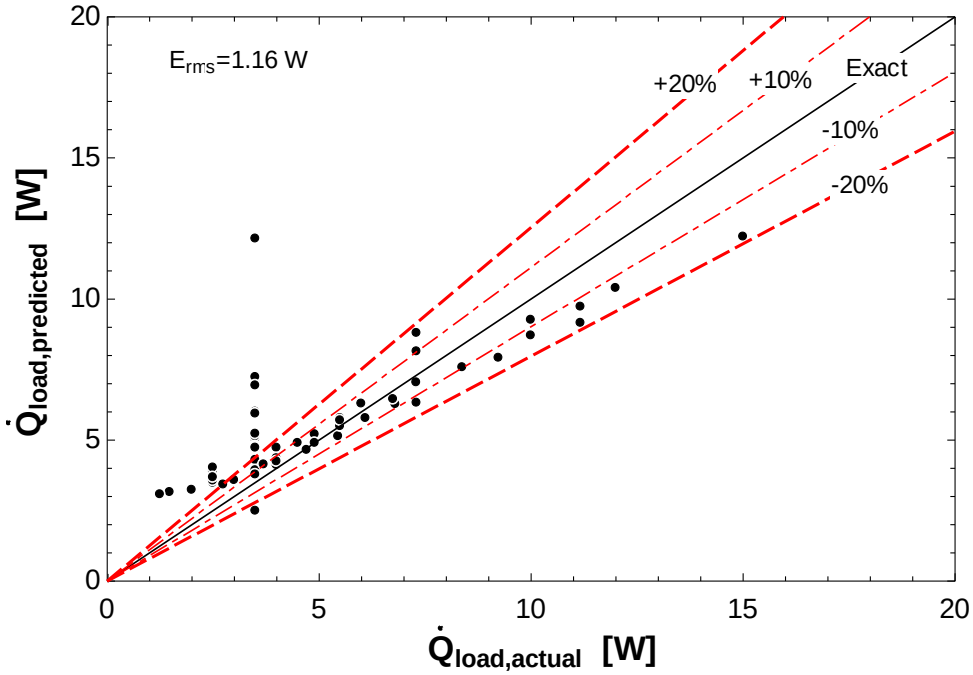

Figure 6-4: Predicted cooling load, evaluated without using the empirical pressure drop correlations, as a function of the cryoprobe refrigeration measured experimentally. Results are based on a six point iterative correction to the temperature at state 4 in order to improve model accuracy.

6.2 Sources of Inaccuracy

Although results from the tuned predictive model showed significant improvement over the original formulation, there are still a few significant outliers. For these points a better understanding of the contributing factor(s) leading to model disagreement is/are needed. Sources of modeling inaccuracy can be attributed to: component-level modeling errors, inaccuracies in predicted thermodynamic properties of the mixed gas refrigerant in the

2nd stage cycle, and experimental operating errors. Component-level errors can be further subdivided and include problems with:

1) The volumetric efficiency compressor map used to determine the mass flow rate from the compressor suction and discharge pressures (compressor model).
2) The assumption that the refrigerant mixture enters the hot side of the recuperator at constant temperature (precooler model).
3) The empirically derived recuperator conductance correlations (recuperator model).
4) The assumption of isenthalpic expansion through the orifice (orifice model).

Section 6.1 dealt exclusively with issues 1 and 2 above, both of which were corrected empirically to improve the model. A few of the major outliers from the tuned model without pressure drop, in terms of the predicted cooling load, are identified in Figure 6-5. Note that for points 13 and 15, the refrigeration output by the model greatly over-predicts that observed experimentally. Point 17 represents the highest cryoprobe refrigeration evaluated, under-predicting the actual load applied by the nichrome wire heater by almost 20%.

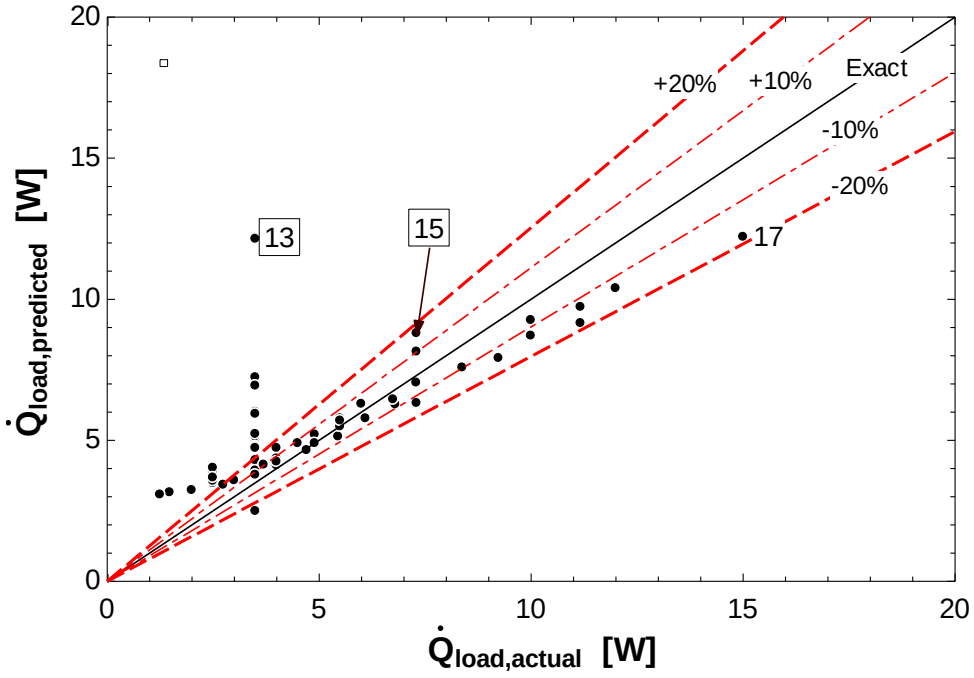

Figure 6-5: Cooling load data output from the tuned predictive model as a function of the actual cryoprobe refrigeration. Three outliers are identified for further analysis.

Data from entries 13 and 15 were collected as part of a sub-set which varied the static 2nd stage charge pressure at constant values of cooling load (equal to 3.5 W and 7.3 W, respectively). The deviation from the actual, measured cryoprobe refrigeration for all points at both 3.5 W and 7.3 W is shown as a function of compressor discharge pressure in Figure 6-6. The deviation is calculated as the difference between the predicted and measured cryoprobe cooling load.

Plotting these data against the static charge pressure directly would be ideal but is not possible as charge pressure measurements can only be taken while the cycle is not operating (and has achieved equilibrium at atmospheric conditions). As can be seen from the plot, a trend between the error in predicted cryoprobe refrigeration and compressor discharge pressure is evident for the 3.5 W data. The error in cooling load is observed to increase along

with the high side pressure (i.e., the predicted cooling load is higher than that measured). However, the exact form of the dependency is somewhat unclear, as few test points are available at the extremes of the range. Error for all of the data at 7.3 W using the tuned model formulation is relatively small. No clear relationship with compressor discharge pressure is observed for this case.

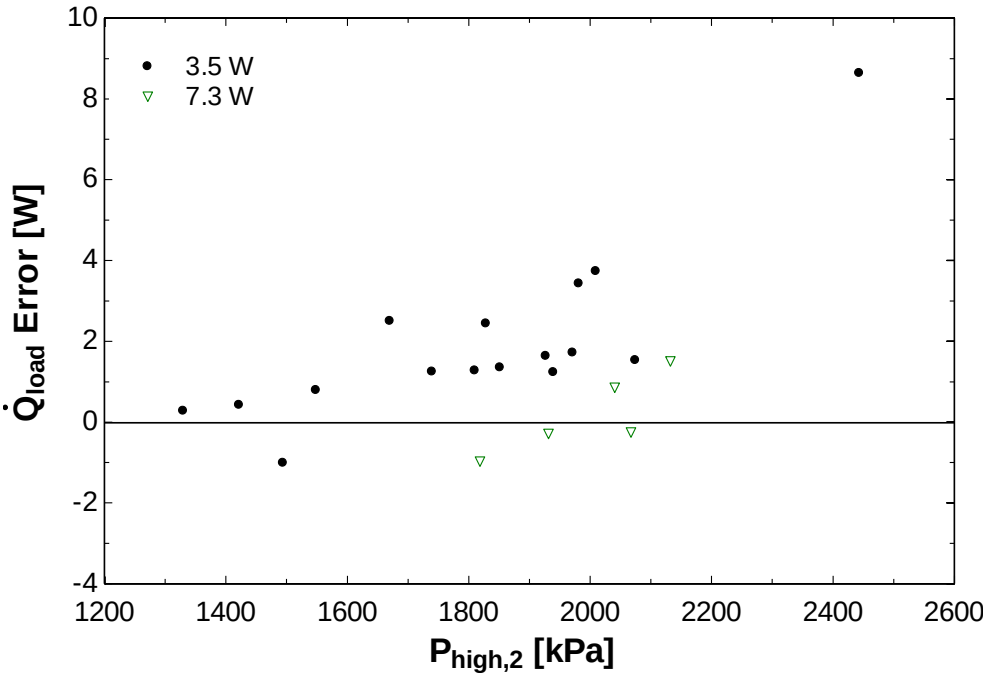

Figure 6-6: Difference between the predicted and measured cryoprobe refrigeration load as a function of the compressor discharge pressure for two data sub-sets (at 3.5 W and 7.5 W).

For test points outside of the constant cooling load sub-sets a simple comparison method was desired that would allow for preliminary assessment of modeling errors. An EES macro was formulated for this purpose, allowing cycle state points determined directly from the measured experimental data as well as from the predictive model to be overlaid on a pressure-enthalpy property plot generated for the test point of interest. This includes the nodal enthalpies/pressures output from the numerical heat exchanger analysis in both

procedures. Such a plot was prepared for entry 17 (from Figure 6-5) in Figure 6-7. Note that the empirical pressure drop correlation is included for this analysis with no correction to T_4 in order to illustrate the usefulness of the technique. For this particular test case, respectable agreement is observed. The findings verify the accuracy of the recuperator conductance correlations. The assumption of isenthalpic expansion over the orifice appears to account for a portion of the error, although prior to correction of the hot side recuperator entry temperature the difference between the measured cooling load was less than 2 W. This emphasizes the impact of using an incorrect value of T_4.

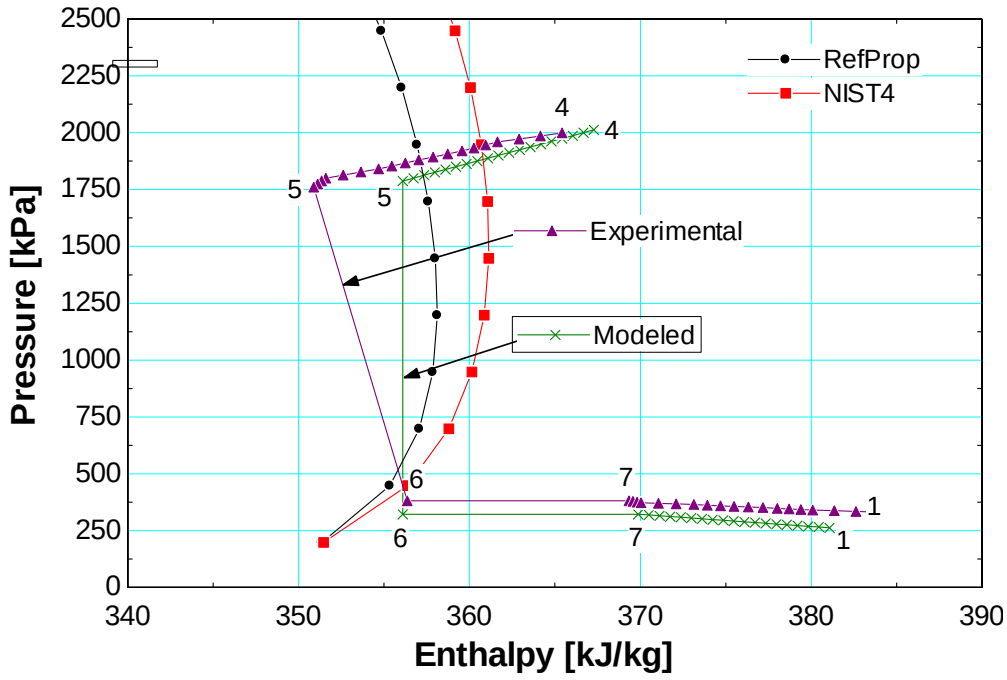

Figure 6-7: Cycle state points comparing the experimental data with that output from the predictive model. Results are overlaid on a pressure-enthalpy plot. The dew-point line predicted by Refprop and NIST4 is also included for this test.

The accuracy of the recuperator conductance model over the range of test points can be assessed in multiple ways. One method is to compute the effectiveness of the recuperator, comparing the results between the experimental data and predictive model. For the majority

of data collected during this research, the cold fluid stream capacitance rate was much less than that of the warm stream. Thus, in the limit of infinite heat exchanger length or conductance, the pinch point would occur near the warm end. The effectiveness for this case can be calculated as shown in equation (6.3)

$$\varepsilon = \frac{h_1 - h_7}{h(T_4, P_7) - h_7} \tag{6.3}$$

where the denominator represents the minimum enthalpy difference if the temperature pinches at the warm end. As discussed in section 5.3.2, using an energy balance over the recuperator to predict the temperature at state 4 often resulted in pinch point errors. In these cases, non-physical values of the effectiveness from the experimental data were calculated ($\varepsilon > 1$). An alternative method that can be used to evaluate the conductance model is to compare the temperature difference between the two fluid streams at the cold end of the heat exchanger (again between the experimental data and predictive model), as illustrated in Figure 6-8. As shown by the plot, agreement from the majority of test points is within 20%. The temperature difference is consistently over-predicted for values greater than 22 K. More tests at higher values of cryoprobe refrigeration load would help to fill in some of the gaps where only a few points are analyzed.

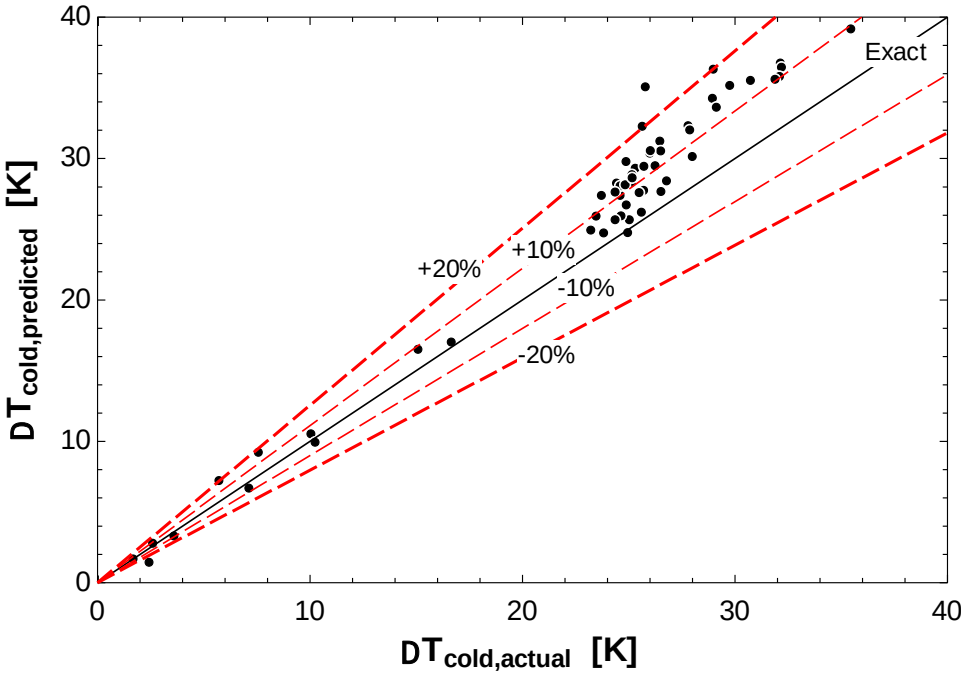

Figure 6-8: The temperature difference at the cold end of the recuperator predicted by the model as a function of the measured cold end temperature difference. Results are shown for the model including the pressure drop correlation.

6.2.1 Predictive Model Assumptions

Major assumptions in the predictive model include the following: the temperature of the refrigerant mixture entering the hot side of the recuperator can be approximated by the saturation temperature of the 1st stage refrigerant; the pressure drop estimated by the empirical correlation can be applied linearly throughout the recuperator and is equal to the pressure drop through the precooler; and the refrigerant mixture expands isenthalpically through the jewel orifice in the 2nd stage cycle. The validity of all these assumptions except for the orifice model were reviewed in the proceeding sections. In order to evaluate the accuracy of the isenthalpic approximation, measurements taken in the vicinity of the expansion device were used to determine the actual change in enthalpy. A simple calculation based on the actual fluid condition before the orifice was also added to the experimental

procedure so that a direct comparison could be made. The result of this analysis, for all of the experimental data, is summarized in Figure 6-9. As shown, the Joule-Thomson effect predicted by the model shows good agreement with that measured experimentally for the majority of the test data. The large error bands on a few of the data points indicate expansion at the location of the dew-point line.

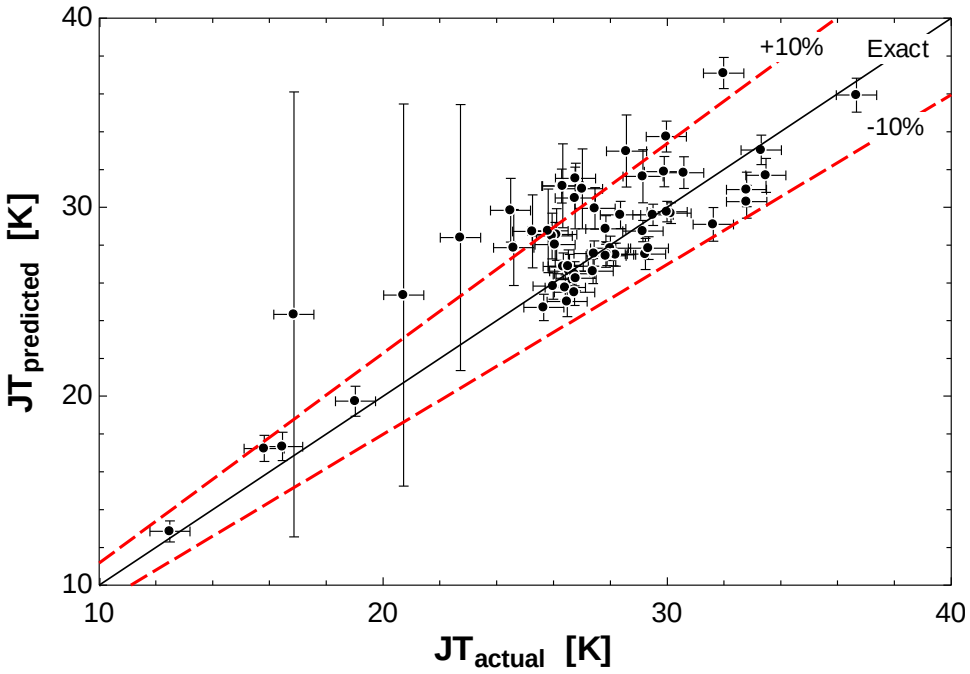

Figure 6-9: Predicted Joule-Thomson effect as a function of the actual change in temperature measure over the jewel orifice.

6.2.2 Thermodynamic Property Calculations

The results of the energy balance analysis used in section 5.3.2 (the analysis in the experimental procedure used to determine the temperature of the fluid entering the hot side of the recuperator) revealed potential inaccuracies with the thermodynamic property data for the R14+R23 refrigerant mixture. In an effort to verify the mixture property data output by RefProp matches the actual behavior of the test fluid, a simple analysis over the cryoprobe test section (about which the load from the nichrome wire heater is applied) can be

conducted. First an energy balance is taken over the heat exchanger representing the active portion of the cryoprobe tip, specified in equation (6.4).

$$\dot{Q}_{load} = \dot{m}_{2nd}(h_7 - h_6) \tag{6.4}$$

The control volume along with associated measurement instrumentation is shown in Figure 6-10. The temperatures at state's 6 and 7 are determined based on the data from PRT's 12 and PRT 10, respectively. As there is direct measurement of the pressure at state 6, an approximation was made using the Müller-Steinhagen and Heck two-phase pressure drop correlation (2002), assuming a test section length of approximately 91.6 mm. However, including the pressure drop correlation was not found to have a dramatic impact on the results, yielding an average test section pressure drop of 0.006 psi.

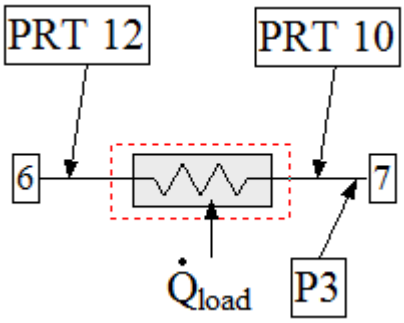

Figure 6-10: Schematic of the heat exchanger representing the active portion of the cryoprobe (tip).

The percent error between the calculated and measured cooling load is shown as a function of the quality (mass basis) at state 7 in Figure 6-11. The greatest outliers are observed near the dew and bubble point lines for the refrigerant mix. The average input load provided by the nichrome wire heater over the range of data points collected is 5.2 W which, for points where the refrigerant mixture is inside the vapor dome at state 6, results in a

relatively small temperature drop over the test section (to within the experimental uncertainty of the PRT's). The effect is a significant increase in the uncertainty for most of the data points analyzed. Unfortunately, filtering the uncertainty to within ±20% error eliminates the majority of points along the dew and bubble point lines observed in Figure 6-10. Thus, experimental data with higher values of input load are required to better quantify thermodynamic property database errors in these regions. A future analysis could accomplish this by comparing the difference between the calculated and observed cryoprobe energy exchange per unit mass to the latent heat of vaporization of the refrigerant mix (at the average test section pressure).

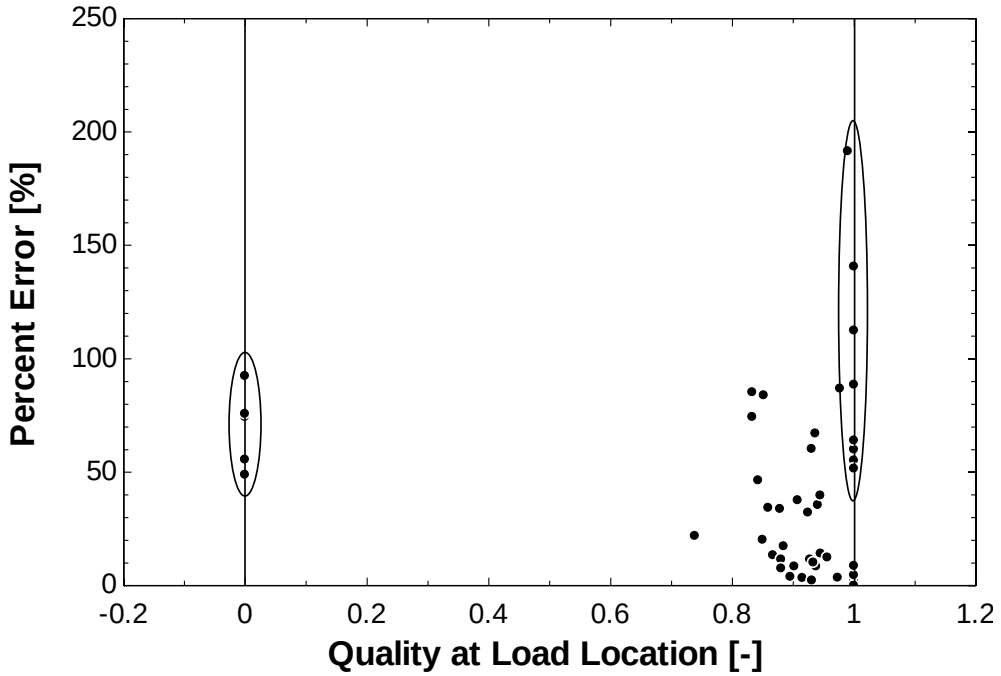

Figure 6-11: Percent error in calculated cooling load using the Refprop property database as a function of the thermodynamic quality (mass basis) at the load location. Results are for a binary mixture of R14 and R23. Points with the greatest uncertainty (>±150%) are filtered from the analysis.

7 Summary and Future Work

7.1 Research Project Overview

The primary goals of this research were to develop, verify, and improve the accuracy of a predictive model for a precooled mixed gas Joule-Thomson cryosurgical probe. Valuable insight into the physical operation of the cryoprobe was gained by understanding model limitations as well as the predicted response to modifications in the input parameters. A significant benefit of the model is that it allows for system optimization (including the charge pressure for the 2nd stage cycle, orifice diameter, and mixture composition) and is constrained only by the size of the compressor and heat exchanger geometry used.

In order to more thoroughly assess the accuracy of the model, experimental testing was conducted which varied the static 2nd stage cycle charge pressure and the input load to the nichrome wire heater. A test mixture was selected via optimization with the predictive model that allowed for better resolution of trends observed during analysis of the two independent parameters of interest. These data were processed using a separate procedure in the model which utilized a similar numerical heat exchanger discretization to more accurately resolve the temperature profile for both the warm and cold fluid streams through the recuperator.

The results of the experimental investigation were compared directly with predictive model outputs. As the mixture composition varied between each data point, a component-level analysis was performed in order to determine the greatest sources of error. The importance of the temperature approximation at state 4 was recognized. It was confirmed that a relationship exists between the low side 1st stage saturation temperature and T_4. A future

analysis could improve upon the correction method performed in chapter 6, taking into account the correction needed at each test point (a linear relationship was observed in section 6.1.2). It would also be interesting to verify the performance dependency on independent parameters not directly varied in this analysis is correctly predicted, specifically the mixture composition in the 2nd stage cycle.

Finally, it is recognized that improvements in thermodynamic property data are needed. For this mixture, inaccuracies were observed in the estimation of the recuperator hot side inlet temperature. In addition to the results provided in chapter 6, errors in property data could be revealed by using the numerical heat exchanger analysis in the experimental procedure to output nodal fluid properties on a temperature-pressure (TP) property plot. From this plot, the actual location of the vapor dome can be visually approximated (or numerically if desired). This technique could be improved by utilizing a more accurate pressure drop model, such as that formulated by Passow (2012) or by using a two-phase pressure drop correlations directly (e.g., reference Didi (2002)).

7.2 Recommended Test Facility Improvements

During the course of experimental testing, a minor leak in the 2nd stage cycle was observed. This leak prevented the use of the test facility in analysis of charge pressures greater than approximately 140 psig (which resulted in readings of Dewar vacuum greater than $1*10^{-3}$ torr during operation). Abnormal increases in the vacuum level were observed during operation of the bypass solenoid valves, even at lower charge pressures, used to prevent oil migration from the compressor. This signifies that the leak is likely on the low pressure side of the system (inside the Dewar). As a precautionary measure during testing,

periods between solenoid actuation were increased to 2 hours. The Dewar vacuum was closely monitored and logged at similar intervals. This leak should be corrected in future investigations and would provide an excellent opportunity to interchange the jewel orifice for further model validation. Other options should also be investigated, potentially for replacement of the current expansion device entirely, as it is the most difficult input parameter to experimentally modify.

7.3 Modeling Considerations

Chapters 3 and 4 summarized the formulation of the predictive model and highlighted issues resulting from the use of the effectiveness-NTU numerical heat exchanger analysis. The computational effort required by the numerical heat exchanger model was also detailed and found to result largely from externals calls to the RefProp thermodynamic property database. Newer versions of the EES_REFPROP interface program (Klein, 2013b) allow for the selective output of the parameter of interest, reducing the computation time required for a single property call. Updating the property functions in the predictive model would be a logical first step to increase model efficiency. A second logical improvement would focus on the iterative solution methodology detailed in chapter 4. A higher order method could potentially be used or an optimization technique better suited to the functional relationship between the cold side recuperator temperature difference and the predicted finned-tube length. It would also be worthwhile to examine functional relationships between the cold side recuperator temperature difference and one or all input parameters, as developing a correlation to improve the initial guess would also reduce computation time.

Lastly, it would be very interesting to add to the model the ability to approximate the actual cryolesion size that would be observed in a surgical environment (for a given operating condition). This could be accomplished by incorporating the power-temperature curve output from an FEHT cryolesion model, such as the one developed by Fredrickson et al. (2006), into the predictive model, thereby allowing for a true global system optimization based on the primary metric for surgical effectiveness.

8 References

Alexeev, A., Haberstroh, C., & Quack, H. (1997). Further Development of a Mixed Gas Joule Thomson Refrigerator.

Babaian, R. J., Donnelly, B., Bahn, D., Baust, J. G., Dineen, M., Ellis, D., . . . Thrasher, J. B. (2008). Best Practice Statement on Cryosurgery for the Treatment of Localized Prostate Cancer. *The Journal of Urology, 180*(5), 1993-2004.

Baust, J., Gage, A. A., Ma, H., & Zhang, C.-M. (1997). Minimally Invasive Cryosurgery - Technological Advances. *Cryobiology, 34*, 373-384.

Didi, M. B. O., Kattan, N., & Thome, J. R. (2002). Prediction of two-phase pressure gradients of refrigerants in horizontal tubes. *International Journal of Refrigeration, 25*, 935-945.

Ely, J. F., & Huber, M. L. (1992). NIST Thermophysical Properties of Hydrocarbon Mixtures Database (SUPERTRAPP). Retrieved from http://www.nist.gov/srd/nist4.cfm

Fredrickson, K. (2004). *Optimization of Cryosurgical Probes for Cancer Treatment.* (Masters), University of Wisconsin - Madison.

Fredrickson, K., Nellis, G., & Klein, S. A. (2006). A Design Method for Cryosurgical Probes. *International Journal of Refrigeration, 29*, 700-715.

Gage, A. A., & Baust, J. (1998). Mechanisms of Tissue Injury in Cryosurgery. *Cryobiology, 37*, 171-186.

Gage, A. A., & Baust, J. (2009). Experimental Cryosurgery Investigations in vivo. *Cryobiology, 59*, 229-243.

Gill, W., Fraser, J., & Carter, D. C. (1968). Repeated Freeze-Thaw Cycles in Cryosurgery. *Nature, 219*, 215-219.

Hoffmann, N. E., & Bischof, J. C. (2002). The Cryobiology of Cryosurgical Injury. *Urology, 60*, 40-49.

Keppler, F., Nellis, G., & Klein, S. A. (2004). Optimization of the Composition of a Gas Mixture in a Joule-Thomson Cycle. *HVAC&R Research, 10*, 213-230.

Klein, S. A. (2012a). EESNIST4: F-Chart Software. Retrieved from www.fchart.com

Klein, S. A. (2012b). EES_REFPROP: F-Chart Software. Retrieved from www.fchart.com

Klein, S. A. (2013a). EES - Engineering Equation Solver (Version 9.420): F-Chart Software. Retrieved from www.fchart.com

Klein, S. A. (2013b). EES_REFPROP: F-Chart Software. Retrieved from www.fchart.com

Klein, S. A., & Nellis, G. (2012). *Thermodynamics*: Cambridge University Press.

Klein, S. A., & Nellis, G. F. (2012). *Mastering EES*: F-Chart Software.

Korpan, N. N. (2007). A History of Cryosurgery: Its Development and Future. *Journal of the American College of Surgeons, 204*(2), 314-324.

Lemmon, E. W., Huber, M. L., & McLinden, M. O. (2013). NIST Reference Fluid Thermodynamic and Transport Properties - REFPROP (Version 9.11).

Maytal, B.-Z., Nellis, G. F., Klein, S. A., & Pfotenhauer, J. M. (2005). Elevated-pressure mixed-coolants Joule-Thomson cryocooling. *Cryogenics, 46*, 55-67.

Nellis, G., Hughes, C., & Pfotenhauer, J. (2005). Heat Transfer Coefficient Measurements for Mixed Gas Working Fluids at Cryogenic Temepratures. *Cryogenics, 45*(8), 546-556.

Nellis, G., & Klein, S. A. (2009). *Heat Transfer*: Cambridge University Press.

Passow, K. L. (2012). *Empirical Model Improvements for a Mixed Gas Joule-Thomson Cycle with Precooling for Cryosurgery.* (M.S.), University of Wisconsin - Madison.

Popovic, P., & Shapiro, H. N. (1995). A Semi-empirical Method for Modelilng a Reciprocating Compressor in Refrigeration Systems. *ASHRAE Transactions, 101*, 367-382.

Rubinsky, B. (2000). Cryosurgery. *The Annual Review of Biomedical Engineering, 2*, 157-187.

Skye, H., Nellis, G., & Klein, S. (2009). Modeling and Optimization of a Cascaded Mixed Gas Joule-Thomson Cryoprobe System. *ASHRAE Transactions, 115*, 996-983.

Skye, H. M. (2011). *Modeling, Experimentation and Optimization for a Mixed Gas Joule-Thomson Cycle with Precooling for Cryosurgery.* (PhD), University of Wisconsin - Madison.

Appendix: Standard Operating Procedure

Startup

1) **Experimental Equipment Setup**
   a) Restart computer to refresh memory
   b) Turn on SCXI 1000 DAQ system
   c) Turn on Lakeshore 332 Temperature Controller – make sure heater is off
   d) Switch on the Variac heater to 140 V – make sure the dial is set to 0%
   e) Turn on Solenoid Valve Rheostat – set to 100%
   f) Check vacuum level in dewar is $< 1 \times 10^{-4}$ Torr (SEE APPENDIX)
   g) Make sure all fans are plugged in
      i) USB fan for vacuum turbo
      ii) Oil separator fan
      iii) 1st stage evaporator fan
   h) Check that the Manual Ball Valves are in the proper position
      i) KF-40 Evac Port Valve – closed
      ii) Pressure Gauge Isolation Valve – closed→already closed during fill (SEE APPENDIX)
      iii) GMC compressor high pressure isolation valve – open
      iv) GMC compressor low pressure isolation valve – open
      v) High Pressure Bypass valve – mostly closed
      vi) Low Pressure Byspass valve – mostly closed
   i) Turn on the DC Voltage Power Supply
      i) Set voltage of Harrison 6296A DC Power Supply to ≈ 250mV (between 200-300mV)

2) **DAQ Software**
   a) Upload previous day's data to the shared network drive
   b) Start National Instruments Labview 8.6
   c) Open latest version of "Cryoprobe" vi from C:\Desktop\DAQ\
      i) 9/13: **Version 3.4.7**
   d) Input the fluid information, mixture information, and jewel size into the LabVIEW interface
      R14 + R23

      0.6 + 0.4

   e) Input the vacuum pressure in the dewar (read from the 943 Cold Cathode Pressure gauge)
   f) Input the ambient pressure (read from the barometer next to the lab door)
   g) Deselect 'Solenoid Valve Sequence' Play Button
   h) Select 'Use default flow meter values' so Play Button is Green (Play Button under the Continuous File Commands)

i) NOTE: the default flow meter values should match the settings in the Endress Hauser Promass 83 Flow Meters. They are currently set to output a frequency signal of 10/260 Hz corresponding to 0/1300 kg/m^3. The 1300 kg/m^3 density limit is probably way higher than is needed, however the LabVIEW program is good enough at resolving the signal frequency that a higher resolution (smaller max density) may not be needed. See flow meter manual if these values ever need to be changed.

i) Run the Labview interface, making sure the "Create new CONTINUOUS file?" and "Write to CONTINUOUS file?" buttons are clicked to on (green light on) if you want to create and new file and write to it.

j) Save the file for data collection in the "Data" folder on the desktop, including date and mixture information in the file name

k) Check the static charge pressure – typical values are:
   i) GMC 65-85 psig
   ii) PCC 145 psig
   iii) PRT≈300K
   iv) TC≈300K

3) Lab Notebook during Startup

a) Record file name (Typical Nomenclature is "R14_R23_Date"

b) Record charge mixture and static charge pressures
   i) P_1, P_2, P_3, P_4 and $P_{7,new}$

c) Record dewar pressures
   i) Record 943 Cold Cathode Pressure
   ii) Record Convectron Pressure Gauge

d) Record start times of GMC and PCC cycles

4) Start System

a) Make sure that the cryoprobe system is plugged in and the power switch is on

b) Turn the PCC Cycle switch off (it's in the gray "High Voltage Danger" box)

c) Turn on AMS CryoGen System once voltage has been set
   i) If system errors out, try adjusting the multimeter voltage - usually the value is between 50mV and 250mV (record this value in the notebook)
   ii) If the pressure in the PCC is too low the system will return an error (the PCC is not supplied a 'trick' voltage like the GMC, and ~45 psig is required for startup)
      (1) $P_{7,new,low}$≈50 psig
   iii) P5 and P7 will not work unless the AMS unit is on (they receive an excitation voltage from the AMS unit). They will work even if the AMS unit errors out.

d) On the AMS CryoGen System:
   (1) From LCD control screen, press option button (left button)
   (2) Scroll down 2 spaces to blank option using down arrow
   (3) Press up arrow, down arrow, and right buttons simultaneously to go into "Service Mode"

(4) Press right button to select "View Sensors"

ii) Turn on the GMC Cycle by pressing the "—" button on the "cryoprobe handle" to begin the cycle and allow the system to stabilize for about 2 minutes.

e) Start the PCC System after the GMC Cycle has stabilized

f) Begin manual Solenoid Valve Sequence (this must be completed every 2 hours)
   i) Check pre-sequence PCC Convectron Vacuum Gauge and 943 Cold Cathode Pressure and record pressure readings in the Lab Notebook
   ii) Click "Manual Override" Play Button on LabView Schematic Screen
   iii) Click "GMC Valve 1," so it is GREEN then listen for the value to hiss open, then click "GMC Valve 1" so that it is GRAY
   iv) Repeat Step (ii) above for "GMC Valve 2"
   v) Wait for the PCC Convectron Vacuum Gauge to return close to the pre-sequence pressure, then Repeat Step (ii) for the "PCC Valve"

   ****NOTE: GMC VALVE 3 IS NOT ACTIVE.*

g) Regulate the GMC cycle pressures using the 2nd stage compressor bypass valve
   i) P1 should be 275-325 [psig], PR should be ~10 (i.e. P1/P5 in psi <10)

5) Allow System to Reach Steady State (≈2.5 hours)—At 200K, start Gas Chromatograph Operation

a) Keep an eye on mass flow and pressure differences to ensure system is not clogging/freezing (mass flow will cut off rapidly and pressures will spike if freezing occurs, in which case you must turn off the system and complete the triple evacuation process for maintenance)

b) Put Kleenex in the top area of the dewar where the pressure taps attach to minimize moisture on the pressure taps

c) Keep an eye on frost conditions on experiment
   i) Turn on the Variac Heater to ≈20[V] once front/condensation forms on the 2nd Stage Return Tube
   ii) If frost forms on 2nd stage return tube (approaching GC collection point), use variac heater (silvery blue) to make sure GC is taking only vapor sample
   iii) Be careful of melting frost on experiment-use paper towels to keep experiment dry and rust-free. Be especially aware of special vacuum fittings with small welded pieces.

d) Cycle Solenoid Valves every 2 hours (you will cycle once before steady state is reached)

e) Wait to operate heater and achieve steady-state conditions until system has run for ≈2.5 hours and PRT10≈165[K]

f) When the system approaches ≈165[K], set desired heater value
   i) Go to "Lakeshore 332" tab in LaVIEW
   ii) Configure "Heater Range" to "High"
   iii) Set Loop to 1
   iv) Select desired "Manual Output" range
   v) Press "Configure" and observe the measured heater power [W]

vi) Adjust "Manual Output" value, pressing "Configure" after each adjustment, until the desired wattage is attained (to within the thousandth [W])

****NOTE: If TC_4 ever gets above 308[K] the heater fault in LabVIEW will trip and will have to be reset on the front panel. This prevents melting of components in the dewar.*

g) Keep door shut to minimize ambient temperature fluctuations

Data Collection

1) Record any unusual observations or deviations from normal procedure
2) Keep door shut to minimize ambient temperature fluctuations
3) Steady State: "Steady State" condition defined as a 20 minute period over which the temperatures change less than 0.25 K (confirm that pressures are also stable)
   a) After criteria for steady state have been met (<0.25 K change in all temperatures over 20 minutes), record the start and stop times (in LabView times) in the lab notebook corresponding to steady state
   b) Record steady state measurements in notebook for future reference (pressures/temperatures/heater values/flow rates, etc.)
   c) Take GC point – See GC operation section below
4) Reset the valve sequence to 15 minutes
5) Adjust the heater value for the next steady state condition

Gas Chromatograph Operation

1) Turn on Helium carrier gas and allow He to flush the system for approximately 20 minutes.
   a) Hook up the copper tubing that connects the Helium bottle to the GC carrier line and to the sample line on the GMC
   b) Open the helium tank and turn in the regulator until the pressure in the carrier line is 50-55 psig (as read on the Column Head Pressure gage on the GC front panel)
      i. NOTE: there is second pressure gage (dial gage) behind the GC that visible from the He bottle. This gage under reads what the CHP actually is – if you want 55psi at the CHP gage, the dial gage should read about 42 psig.
   c) NOTE: He regulator is touchy, and CHP gage may take several minutes to adjust
2) Turn on the GC (switch is on bottom right side) and wait for self-check routine to finish (screen will read 'EMULATION MODE OK')
3) Prepare GC components
   a) Set the oven temp to 50ºC by pressing the OVEN TEMP button, followed by the ON button
   b) Set the injector temp to 100ºC by pressing INJ A TEMP, then ON
   c) Turn TCD A detector on by pressing DET, A, and ON
      i. NOTE: you will hear clicking sound when TCD is on

4) Allow TCD signal to come to equilibrium (to view the TCD signal, press SIG 1 twice)
    a) The baseline signal should become steady in the range of 3.5 to 4.5 after 30-60 min
        i. If the Helium was cycled for 20 minutes prior to operating the CG, baseline signal will become steady in ≈10 minutes
    b) Wait until there is no variation in the signal for ~10 min
    c) NOTE: changing the CHP pressure will change the baseline.
    d) NOTE: if SIG 1 is assigned to B, press SIG 1, A, ENTER to assign A to SIG 1
5) Turn on the HP Integrator if using for data collection (push button on the back)
    a) Allow unit to warm up, wait for green "READY" LED to light up
    b) Press the ATTN key twice (it will print "ATT ^2"), press 5, then ENTER
        i. NOTE: This scales the peaks so they fit on the page without being cut off (increasing the attn will make the peaks smaller)
    c) Press the THRSH button twice (it will print "THRSH"), press 5, then ENTER
        i. NOTE: This sets the threshold for noise reduction (increasing the threshold will decrease the amount of noise picked up)
6) Flush sample line with Helium
    a) Open the screw valve near GMC sample point
    b) Let helium flow at 10-20 ccm (read on rotameter by GC) for 10 minutes
    c) Close screw valve
    d) NOTE: if you are using gas directly from a bottle, flush sample line with that gas for 10 minutes at 10 ccm
7) Adjust GMC sample flow
    a) Make sure black valve on left side of GC is barely open
    b) Open sample line ball valve when steady state has been achieved in GMC
    c) Adjust P_{gage} to ~10-20 psig and P_{diff} to ~0.08-0.12
        i. Look at "GC" tab in Labview for values
        ii. Adjust readings by changing the positions of the black screw valve (left side of GC) and rotameter dial (on top of GC)
8) Begin GC run
    a) Make sure "NOT READY" light on front of GC is off
    b) Record the P_{gage}, P_{diff}, rotameter flow measurement (may be very small), and TCD baseline values in the notebook
    c) If just using integrator:
        i. Press "Start" on front of GC
        ii. Press "Start" on Integrator
        iii. Wait for 2nd hiss (signaling close of pneumatic injection mechanism)
        iv. Close sample line ball valve
        v. Wait until all peaks elute (~ 20 min for R23)
        vi. Press STOP on integrator to see measurements
        vii. Press STOP on the GC
        viii. Record areas in notebook
    d) If using LabVIEW Cornell GC software in conjunction w/ integrator (SOFTWARE IS CURRENTLY BUGGY – 5/4/12):

i. NOTE: The integrator is run in addition to the LabVIEW software to validate the new digital method
ii. NOTE: The GC must be set to an older Firmware Mode (HP 5890 Series A mode) to work with the software
    1. The component labeled P15 (consists of two pins) on the main PC Board underneath the right side panel of the GC must be jumped together to be in the "HP 5890 Series A" mode.
    2. If the GC screen reads "EMULATION MODE OK" after the GC finishes its self-check then it is in the HP 5890 Series A mode. If it reads "PASSED SELF TEST" then it is in the HP 5890 Series II Mode.
    3. The Integrator can be used in either the old mode or the new mode
iii. Open GasChromatograph.lib
iv. Open GasChromatograph.vi from LLB Manager
v. Accept Terms and Conditions, Click OK
vi. Press "Set Method"
    1. Temperature default values should be correct (Oven temp 50ºC, Inj A port 100º, TCD temp 100ºC)
    2. Change data rate to 5 Hz – otherwise labview will time out early
    3. Press OK
    4. Turn TCD ON by clicking button and toggle switch if it isn't already
    5. Wait for temperatures to adjust
    6. Press OK
vii. Follow setup for integrator (step 5 above)
viii. Press "Measure Sample"
    1. Press ok
    2. Press START on integrator
    3. Wait for 2nd hiss (signaling close of pneumatic injection mechanism)
    4. Close sample line ball valve
    5. Wait until all peaks elute (~ 20 min for R23)
    6. Press STOP on integrator to see measurements
    7. Press STOP on LabVIEW vi
    8. Save chromatogram
        a. Press "Save Chromatogram"
        b. Enter name and description, and record in lab notebook
    9. Set peak threshold, max noise, and min points to fit in vi to 0 to allow program to autocalculate retention times and areas
    10. Copy results to Excel to calculate corrected mole percents
ix. NOTE: See the "HP 5890 Gas Chromatograph LabVIEW Software Info" file (or the attached sheets) for more information about software

9) After all desired GC points have been recorded:
    a) Quit LabVIEW GC vi

b) Turn GC off
c) Turn off helium carrier gas

Shutdown

1) Turn Lakeshore 332 Temperature Controller to 0%
2) Turn off Variac heater
3) Cycle 1st and 2nd stage solenoids manually
   a) Press "Manual Override"
      i) Press "GMC Valve 1", leave for 4-8 sec and then turn off
      ii) Press "GMC Valve 2", leave for 4-8 sec and then turn off
      iii) Press "PCC Valve 1", leave for 4-8 sec and then turn off
4) Turn off Solenoid valve Rheostat
5) Turn off PCC Cycle first (using the switch in the High Voltage box)
6) Press "+" button to turn off GMC cycle
7) Allow ~10 min. for fans to cool compressors
8) Unplug all fans
9) Allow LabVIEW data to continue to collect data as the system warms up
10) As the system warms up, wipe off the snow and water that collects on the tubes and dewar
    a) NOTE: Leaving water on the sensors and fragile weld vacuum connections can cause sensor damage and rust!
11) Press power button on CryoGen system to turn machine off

Maintenance

Refrigerant Recovery

1) Connect the Promax Refrigerant Recovery Machine (RG6000) to a 115V outlet
2) Check to make sure the inlet and outlet valves on the RG6000 are both set to closed
3) Connect the inlet line on the RG6000 unit to the GMC low schrader valve (closed)
4) Connect the outlet line on the RG6000 unit to the blue (liquid) valve on the appropriate (R410a or Mix) yellow recovery tank (NOTE: max psi of 350)
5) Slowly open the blue (liquid) valve of the recovery cylinder while watching hoses and connections for leaks
6) Set the recover/purge valve on the RG6000 unit to "RECOVER"
7) Open the outlet valve on the RG6000 unit
8) Toggle the power switch to the "ON" position
9) Open the inlet valve on the unit
10) Slowly open the low schrader valve, about 1 psi drop per update
11) Note: If the unit begins to "knock," slowly throttle back the schrader valve until the noise stops
12) Run the RG6000 until the desired vacuum is achieved
13) Close the low schrader valve

14) Turn the inlet valve on the RG6000 to the "CLOSED" position
15) Toggle the power switch to the "OFF" position
16) Purge Procedure
17) **CAUTION: Always purge the RG6000 unit after a recovery procedure. Failure to purge the remaining refrigerant from the unit could result in acidic degradation of internal components, ultimately causing premature failure of the unit.**
18) Verify the schrader valves are closed
19) Verify the outlet valve on the unit is open and the inlet valve is closed
20) Verify the liquid valve on the recovery cylinder is open
21) Turn the recover/purge valve to the "PURGE" position
22) Toggle the power switch "ON"
23) Slowly turn the inlet valve toward the "PURGE" position
24) As the inlet side pressure decreases, open the valve to the full purge position
25) Run the unit until the desired vacuum is achieved
26) Close the inlet and outlet valves on the unit
27) Toggle the power switch "OFF"
28) Close the ports on the recovery cylinder
29) Turn the recover/purge valve to the "RECOVER" position

Triple Evacuation/Purge for GMC plumbing

1) Recover refrigerant in GMC (see Refrigerant Recovery above)
2) Evacuate
   a) Make sure pressure in system is <2 psig
3) Connect orange cart roughing pump to system
   a) Connect to KF-40 evac port
   b) Connect to GMC high schrader valve
   c) Connect to GMC low schrader valve
   d) Connect to Convectron vacuum gauge 1
4) Valves
   a) KF-40 evac port valve - closed
   b) Convectron vacuum gauge 2 isolation valve – closed (pressure > ambient could ruin gauge)
   c) High pressure isolation valve - closed
   d) Low pressure isolation valve – closed
      i) NOTE: Closing the isolation valves helps keep oil from entering the system
   e) Bypass valve - open
   f) GMC high schrader valve - closed
   g) GMC low schrader valve - closed
5) Turn on vacuum pump
   a) Evacuate refrigeration hoses and KF-fittings to 200 mTorr
6) Slowly system valves
   a) Crack open the KF-40 evac port valve
   b) Wait about 30 s before opening the vacuum gauge isolation valve (where Convectron vacuum gauge 2 is located)

c) Watch the pressure gauge while slowly opening KF-40 evac port valve the rest of the way
    i) Make sure the gauge stays in a vacuum and that the pump is not being overworked
d) Wait until vacuum gauge 1 (nearest the roughing pump) is at 200 mTorr

7) Evacuate from GMC low schrader port
a) Slowly open GMC low schrader valve with small adjustments
    i) Open valve a small increment, observe vacuum pressure jump
    ii) Wait until vacuum pressure returns to low value (after ~1 minute) before next small adjustment
    iii) Continue until GMC low schrader valve fully open
b) Open solenoid valves one at a time, waiting for pressure to return to 200 mTorr
c) After about 10 minutes, close both solenoid valves

8) Evacuate from GMC high schrader port
a) Open valve slowly

9) Wait for vacuum pressure to reach its lowest value
a) The first evacuation will take longer (maybe leave overnight)
b) Subsequent evacuations may take only 3-4 hours
c) Previous low points have been ~ 150 milliTorr (on 2nd/3rd evacs)
d) Record vacuum level and time to reach ultimate vacuum in lab notebook

10) Stop evacuation process
a) Close the valves
    i) KF-40 evac port valve - closed
    ii) Convectron vacuum gauge 2 isolation valve – closed
        (1) Don't blow out the vacuum gauge! – close vacuum gage valve
    iii) High pressure compressor isolation valve - open
    iv) Low pressure line valve - open
    v) Bypass valve - closed
    vi) GMC high Schrader valve – closed
    vii) GMC low Schrader valve - closed
b) Turn off the vacuum pump

11) Purge with Nitrogen
a) Ball Valve Settings
    i) KF-40 evac port valve - closed
    ii) Convectron vacuum gauge isolation valve 2 - closed
        (1) Don't blow out the vacuum gauge! – close vacuum gage valve
    iii) High pressure compressor isolation valve - open
    iv) Low pressure compressor isolation valve - open
    v) Bypass valve - closed
b) Open Nitrogen tank valve, pressure on backside of regulator should read tank pressure
c) Check that regulator frontside pressure reads 0
d) Open brass valve screw valve
e) Purge fill line including the Service Access valve

i) Turn regulator dial in until gas comes out – regulator pressure gauge may not move, listen for gas exiting fill fitting
ii) Allow to purge for ~10-15 seconds where last 5 seconds are with service access valve screwed mostly onto GMC high schrader port
(1) NOTE: It is important that there is no air in the system – air has water in it which will freeze in system

f) Tighten Service Access Valve on GMC high schrader valve– finger tight, plus ~1/2 turn. If Fill fitting leaks during pressure increase, tighten fitting
g) Turn regulator dial in until the pressure reads ~20-40 psig
h) Open GMC high schrader valve SLOWLY, such that the pressure rises ~2 psig per LabVIEW measurement update
i) Watch GMC pressures in LabVIEW under the "Filling pressures" section
j) When median pressure reaches desired pressure, close schrader valve

12) Turn Regulator valve all the way out
13) Close brass screw valve
14) Close Nitrogen tank valve
15) Disconnect fill line and open GMC low schrader valve to relieve pressure to ~2 psig
16) Close GMC low schrader valve
17) Repeat Evacuation – record vacuum level
18) Purge
19) Final evacuation
a) Connect the refrigerant fill line to the GMC high schrader port via the service access valve to evacuate the fill line (the vacuum pump will only be connected to the LP Schrader port and the KF-40 Evac port)
b) Open tank valve for refrigerant, pressure on backside of regulator should read tank pressure
c) Check that the regulator (front) pressure reads 0
d) Open screw valve
e) Purge fill line including the Service Access valve
i) Turn regulator dial in until gas comes out – regulator pressure gauge may not move, listen for gas exiting fill fitting
ii) Allow to purge for ~10-15 seconds where last 5 seconds are with service access valve screwed mostly onto GMC high schrader port
iii) NOTE: It is important that there is no air in the system – air has water in it and will freeze in system

f) Tighten Service Access Valve on GMC high schrader valve– finger tight, plus ~1/2 turn. If fill fitting leaks during pressure increase, tighten fitting
g) Close screw valve
h) Open GMC high Schrader valve
i) Proceed with evacuation as normal (steps 4-10, ignoring 8)

20) Record vacuum level
21) Fill with desired refrigerant after 3 evacuations and 2 Nitrogen purges

Charging the GMC Cycle Plumbing with Refrigerant

1) Complete Triple Evac/Purge process
2) There should be a vacuum on the system of less than 100 mTorr
3) Check valve positions
    a) KF-40 evac port valve - closed
    b) Convectron vacuum gauge 2 isolation valve – closed
        i) Don't blow out the vacuum gauge! – close vacuum gage valve
    c) High pressure compressor isolation valve – open
    d) Low pressure compressor isolation valve – open
    e) Bypass valve – closed
    f) GMC high schrader valve – closed
        i) Should be connected to refrigerant with fill line evacuated
    g) GMC low schrader valve - closed
4) Open screw valve on refrigerant
5) Open GMC high schrader valve
6) Turn Regulator Valve in to ~70 psig (or +5psi whatever charge pressure is needed)
    a) Watch Labview pressures, regulating rate with the schrader valve
    b) System will lose some charge before beginning
7) Close Schrader valve
8) Turn Regulator valve all the way out
9) Close brass screw valve
10) Close refrigerant tank valve
11) ALTERNATIVELY: Use manifold to charge system
    a) Connect hoses
        i) Connect hose from high schrader port to left side manifold connection
        ii) Connect second hose from vacuum system to middle manifold connection
        iii) Connect third hose from desired refrigerant to right side manifold connection
    b) With all manifold valves open and the schrader port closed, run vacuum to evacuate fill lines
    c) Close middle manifold connection valve and turn off vacuum
    d) Turn in refrigerant regulator to desired pressure
    e) Open GMC high schrader port SLOWLY, adding ~2 psi per LabVIEW update
    f) When desired charge is achieved, close schrader port and see Refrigerant Recovery to recover refrigerants that cannot be released into the atmosphere

NOTE: To evacuate and charge the PCC you must use the PCC low schrader port. Everything else is the same as for the GMC cycle except that there are no intermediate valves (like the high and low isolation valves) that need to be closed on the PCC.

NOTE: If the regulator on the bottle does not go high enough to achieve the desired charge pressure, you will have to attach the fill line to the LOW schrader valve (not the high valve) and suck in refrigerant when the compressor is running. This will work for both the PCC and GMC. Be aware that you won't know what the true resting charge pressure is until you turn the compressors off and let the system cool down.

Evacuating the Dewar

1) Connect gray roughing pump to the dewar by attaching the stainless steel vacuum hoses to the T-fitting attached to the turbo vacuum pump
2) Make sure purge valve (small thimble-like valve near-ish where the cold cathode vacuum gage is located) is screwed closed
3) Makes sure blue valve lever by roughing pump is closed
4) Turn roughing pump on
5) Slowly open blue valve lever
6) Watch Convectron vacuum pressure gauge (near the cold cathode gauge) to ensure pressure decreases slowly
    a) At 5 Torr, open blue valve lever 100%
7) Listen to pump pitch and smell for pump oil to make sure pump is not overworked
8) When valve is fully open, wait for a pressure of ~1000 milliTorr to ensure there are no leaks
    a) Make sure the USB is plugged in for the DC fan
9) Press start on the turbo controller
    a) Make sure the USB fan cooling the turbo is plugged in
10) Turn on 943 Cold Cathode Pressure gauge to read vacuum pressures less than 1e-3 torr
11) Wait until 943 Cold Cathode Pressure gauge reads a vacuum of < 1x10-4 Torr before starting experiment
12) NOTE: Sometimes after the turbo has been on for 24+ hours and the vacuum is really good (below 1x10-5Torr), the Cold Cathode Gauge will read erratically between 10x-4Torr and 9x10-6Torr